STUDYING THE INTERFACE BETWEEN DNA AND INORGANIC NANOPARTICLES TO CONTROL SHAPE AND ANISOTROPICITY

BY

LI HUEY TAN

DISSERTATION

Submitted in partial fulfillment of the requirements
for the degree of Doctor of Philosophy in Chemistry
in the Graduate College of the
University of Illinois at Urbana-Champaign, 2015

Urbana, Illinois

Doctoral Committee:

Professor Yi Lu, Chair
Professor Paul V. Braun
Professor Jianjun Cheng
Professor Catherine J. Murphy

ABSTRACT

Nanomaterials with their unique optical, electrical and chemical properties are promising candidates for various applications ranging from catalysis to biomedicine. To realize the full potential of nanomaterials, it is important to demonstrate fine control over nanoparticle morphology, and precise spatial control of the position and orientation between multiple nanoparticles. These issues in the field of nanomaterials are challenging to address and would greatly benefit from the precision and programmability of biomaterials such as DNA. In order to better apply DNA to solve issues in the field of nanomaterials, it is necessary to understand the interactions between DNA and metal nanoparticles. This thesis demonstrates the use of DNA to offer control over nanoparticle morphology and anisotropicity. The role of DNA in programming the growth of nanoparticles into different shapes were investigated through *ex situ* and *in situ* experiments. The optimal pH range for DNA to guide nanoparticle growth was investigated. In addition to shape control, precise positioning and assembly of nanoparticles are also important. Anisotropic nanoparticles have been synthesized through competition of DNA and another hydrophobic ligand on the nanoparticle. Finally, the stabilities of DNA in the presence of nanoparticles were further investigated to understand the conditions suitable for the DNA-nanoparticle hybrids to be used for various applications.

For my loved ones

ACKNOWLEDGEMENT

There are many people whom I wish to thank who have made my journey in UIUC very memorable. Thank you to Dr. Lu for accepting me and providing support all these years for my research. I remember when I was struggling through my research in my second year, I told Dr. Lu that I felt that I cannot do a lot things in this lab due to lack of expertise and resources. Dr. Lu immediately disagreed with me and told me that "UIUC has one of the best facilities and research faculties around, what do you mean by no resources. If there are no resources in our group, I am sure we can find someone on campus that have the expertise to collaborate with." Dr. Lu kept true to his word and I am truly grateful to have him as my advisor. With his dedication and support, I have had numerous collaborators along my research journey that I have learnt from and have helped me through my research.

To my committee members, Prof Jianjun Cheng. I do appreciate the tough prelim that you all had given me. It helped me to shape my thinking and figure out what is important in research. Prof Catherine Murphy, thank you so much for your support. I am thankful that you are always open to provide any amount of help and advice. Prof Paul Braun, I remember your advice that research is not about trying to create stuff but trying to understand or discover the science behind it. I think that has been the most exciting part of my research.

My research journey was filled with help from collaborators whom all I am grateful to have. Donghai Gai from Prof. Jimmy Hsia's group, who helped simulate my Janus nanoparticles, Yin Liu from Prof. Shen Dillon's group who helped with wet-cell TEM and introducing me to *in situ* nanoparticle characterization, Dr. Jianbo Wu from Prof Hong Yang and Prof Jian-Min Zuo's group for help with *in situ* flow-cell TEM endeavors in UIUC and all the discussion on nanoparticle characterization, Dr. Taylor Woehl and Dr. Tanya Prozorov, both of whom have provided great

support in the *in situ* flow cell characterization of the nanoparticles. In addition I have to thank Prof Nahil Sobh and his students from the NanoBIO Node group, who helped simulated the gold nanoprisms and Manish Shankla from Prof. Aleksei Aksimentiev's group who provided me with tutorial sessions on computational methods and allowed me to understand how computational studies could assist in my research.

This next part is a big thanks to my dear labmates who have made my time here really wonderful and comfortable. I really want to thank my seniors Dr. Zidong Wang and Dr. Tian Lan who are ever helpful, Dr. Hang Xing, Dr. Lele Li for all the discussions on my research. Dr. Brian Ngo Yin Wong who helped me get adjusted into the Lu group and start off my research journey. Dr. Xiang Yu, Dr. Jingjing Zhang, Dr. Hui Wei who are very experienced and provided great advice on my projects. Dr. Joy Sinha and Dr. Joonhee Han who provided me with a lot of support while I was looking for jobs. To the awesome students who have worked with me through summers, Arzeena Ali, Erfan Mohamadi, Xueyao Liu, Bené Johnson, thank you for trying out the ideas that I had but had no time to test. Also thank you for giving me the opportunity to learn to teach better. Thank you to all the visiting scholars I met here, especially Tingjie Song, Po-Cheng Chen, Jiangjiexing Wu, Yuan Yue, Chunmei Gu, Panshu Song and Siu Yee New, the times I had with you all were short but memorable, I truly appreciate having had you around although it hurt each time you left. My labmates who are also my close friends here, Hannah Ihms, Ying He, Seyed Fakhreddin Torabi, Peiwen Wu, Kevin Hwang, Parisa Hosseinzadeh, Chang Cui, Claire McGhee, Nitya Sai Reddy Satyavolu, Lu Chen. Thank you for always being there for me and making the Lu group feel like home. Thank you for putting up with me despite of all the noise pollution I made in the lab from playing music or the flute, my unconscious urges to hog sharpies, my inability to spell properly, and making the lab smell like hot chocolate all the time.

Thank you to my badminton and volunteering group of friends, Marco Tjioe, Boon Chong Goh, Marcus Tan, Jason, Ram Reddy, Subbu, Chye Hong, Audrey, Catherine, and all the commissioners of Tzu Chi. Thank you for playing badminton with me despite my mediocre badminton skills. Thank you for continuously inspiring me to be a better person and to be grateful even when times are difficult. My Saturday mornings have been full of joy for the last five years thanks to the children and volunteers in Crisis Nursery.

My time here would not have been complete without my landlady and her family, Stacy Harwood, Ema, Emilio and Buddy. They have provided me a home far away from home for the last six years. The home is always welcoming, warm and cozy. Going back home is the best feeling after a long and tiring day with Buddy always welcoming me and being unconditionally happy all the time. I am thankful to be part of the family as I watched Ema and Emilio grow up, went on family trips to Mexico and California, and experienced Thanksgiving, Christmas, New Years and Halloween in the US.

Finally I would like to thank my parents, Yoke Cheng Tan and Dee Soon Lee and my family, Li Choong and Li Xing for always being around to support me. Although they do not know much about my research, they still provided me with a lot of encouragement and lifted me up in times of need.

To all my friends who are reading this, I truly wish you all the best in your journey in grad school and your journey in life in the future. I pray for you to have the courage to face all the challenges that come in your way.

TABLE OF CONTENTS

CHAPTER 1

INTRODUCTION

Part of this chapter was published in "DNA as a Powerful Tool for Morphology Control, Spatial Positioning and Dynamic Assembly of Nanoparticles", Li Huey Tan, Hang Xing, Yi Lu, *Accounts of Chemical Research*, **2014**, *47*, 1881-1890.

1.1 Overview

Nanomaterials have shown enormous promise as next-generation materials in many areas from catalysis to photonics, environmental detection, biomedical diagnostics and therapy.[1-4] Such promise arises from unique properties intrinsic to these nanomaterials, such as plasmonic and quantum confinement effects that change with morphology (both shape and surface structure)[5] and interparticle distances.[6,7] Therefore, in order to realize the full promise of nanomaterials, it is important to control their morphology and the precise spatial control of position and orientation of these nanomaterials. To address this challenge, one promising method is to incorporate the use of deoxyribonucleic acid (DNA), which stands out as an excellent material for providing both precise spatial control at the nanometer scale and specificity in interactions. These functionalities are due to DNA's predictable base-pairing interactions and sequence programmability. Recent progress has shown that DNA can form various geometries and motifs beyond the standard double helix, allowing further assembly into 1, 2 and 3-dimensional structures.[8-14] These DNA nanostructures can be further conjugated to other nanomaterials through the addition of functional groups on DNA, such as amine, sulfhydryl or carboxylate groups.[15-18] To better combine the advantages of metallic nanomaterials with the precise programmability of DNA, this introduction will cover the basic

understanding of the interactions between DNA and gold (Au), the mechanism of formation of nanoparticles and factors that affect the synthesis of the particles.

1.2 Discovery of DNA codes that control nanoparticle morphology

The discovery of the three-letter genetic code, which consists of combinations of DNA nucleotides that encode for specific amino acid sequences enabling the production of proteins, is a foundation for modern biology. We hypothesized that exploration of DNA sequence combinations could also be used for controlling the morphology of nanomaterials. This discovery could have transformative potential not only in advancing the fundamental knowledge of biomolecular interactions with nanomaterials, but also in producing nanomaterials with novel morphology for applications including catalysis, environmental detection and medical diagnosis or therapy.[1-4,19]

DNA has been widely used as templates or scaffolds for assembly of nanoparticles (NPs) for various applications.[20-24] The majority of the work reported so far, however, has involved functionalization of the synthesized nanomaterials with DNA,[25-29] thereby the effect of DNA in influencing the NP morphology during growth is not well understood. Some recent studies using DNA during NP synthesis encouragingly suggested that different DNA sequences are able to influence both the structure and properties of the resulting nanomaterials.[30-36] However, few studies have comprehensively and systematically reported the effects of varying DNA sequences on the growth of NPs, and few rules have been summarized and applied towards the synthesis and fine control of NP morphology. To bridge this gap, we used a seed-mediated growth method to investigate the influence of different DNA sequence combinations on the growth of NPs. The growth of the NP seeds into various structures upon pre-incubation with different DNA sequences

was monitored. In our initial study, we found that reduction of Au in the presence of a single stranded DNA (ssDNA) containing 30 repeating units of either cytosine (C30) or adenosine (A30) transformed spherical AuNP seeds into stable spiky nanoflowers. In contrast, 30 units of thymine (T30) resulted in only larger spherical AuNPs (Figure 1.1a).[37] The produced nanoflowers have excellent scattering properties and were used for dark-field imaging of cancer cells, showing higher imaging contrast than corresponding spherical AuNPs. More interestingly, the DNA on Au nanoflowers were shown to have enhanced stability against dithiothreitol replacement in comparison to thiolated DNA on AuNP surface due to partial embedding of the DNA during NP growth. Despite being partially embedded, the DNA on the surface retain its capability for hybridization.[37]

Encouraged by the above results, we further explored the effect of sequence combinations of DNA to investigate potential synergy or interference caused by combinations of different DNA bases. Instead of using spherical NPs, we chose the triangular Au nanoprism as a seed due to its defined facets which allow a more specific understanding of the mechanisms of growth. This system produced a variety of morphologies such as round rough plates, smooth six-pointed stars, smooth hexagonal plates and round flat plates, in the presence of A30, T30, G20 and C30, respectively (Figure 1.1b).[38] The morphologies of AuNPs obtained were found to be independent of the length of the DNA strands, suggesting the important role of the nucleobases in controlling the shape. More excitingly, we found that there is a clear transition from one morphology (e.g., hexagon with G20) to another (e.g., six pointed star with T30) when using different sequence combinations under identical experimental conditions. For example, a transition between six-pointed stars to hexagons was observed with increasing G to T ratio, *i.e.* from T30, T20G10, T15G15, T10G20 to G20. Similar transitions in other sequence combinations were also observed.

These results suggest that DNA has the ability to control and encode the synthesis of NPs to specific morphologies based on the DNA sequence. Based on these results, a set of rules that govern the morphology and shape transition of the NPs for homogeneous and mixed DNA strands has been established. This method of growth has also been extended to the programmable growth of silver nanocubes and Au nanorods.[39]

1.3 Interaction between DNA and gold

1.3.1 Binding affinity of DNA bases to gold

The binding affinity of DNA to metal is highly sequence dependent and metal ion dependent.[40] The interaction of DNA strands with gold nanoparticles (AuNPs) has been studied extensively using citrate capped AuNPs.[41-45] The difference in binding affinity of the DNA bases affects the functionalization of DNA on Au surfaces,[46] and the stability of resulting AuNPs.[47] The binding affinity of DNA to metal is proposed to occur through interaction of the metal ion with the phosphate backbone by electrostatic interaction or coordination with the nucleobases.[48] The DNA bases contain nitrogen and oxygen-containing groups that can bind to the metal surface and coordinate to metal ions. These potential binding sites are indicated in red in Figure 1.2. Different binding affinities of bases towards metal have been reported[48,49] such as for Au,[44,50] silver,[51] platinum[52] and mercury ions.[53,54]

The binding affinity of DNA to Au is still under investigation as there are various reports with different relative binding affinity trends between bases. There have been three reported attempts to experimentally determine the relative binding affinity of each base to Au surfaces.

A. Demers *et al.* have investigated the thermal desorption energy of DNA bases on Au (111) thin films using reflection absorption Fourier transform infrared (RAIR)

spectroscopy. The thermal desorption energy (ΔH_{des}) determined was in the order of G > A > C > T for desorption of the bases from the Au surface into a vacuum environment (Table 1.1).[55] The ΔH_{des} were reported to decrease when nucleosides were used, indicating disruption of the most favorable binding orientation through steric hindrance. This changes the relative ΔH_{des} to be rather similar for A, C and T. It is important to note that, in determination of the relative ΔH_{des}, the value is dependent on the interaction between the base on the surface of Au in which more efficient pi stacking of the bases may lead to higher ΔH_{des}.[56]

The relative ΔH_{des} do not fully reflect the binding affinity of DNA oligomers to Au as it does not consider solvation effects. In addition, the binding affinity of a polymeric DNA strand may be affected by steric effects and the flexibility of the oligomer that may hinder optimal orientation for binding. Intramolecular interactions including pi-pi stacking or hydrogen bonding within the bases in the DNA strand may also affect the binding affinity of DNA to Au.

B. A better reflection of the relative binding affinity of bases to Au was reported by Hiromi *et al.* in the order of A > C ≥ G > T. The relative binding affinities were determined from binding competitions between DNA oligomers of 5 repeating units, *i. e.* $(dA)_5$, $(dC)_5$, $(dG)_5$ and $(dT)_5$ noted as A5, C5, G5 and T5 in this report, using Fourier transform infrared (FTIR) and X-ray photoelectron (XPS) spectroscopy techniques and performed in aqueous solution.[57] This study was performed on an Au (111) surface. The order of relative binding affinities is different from the one previously reported by Demers *et al.*, where most notably the relative affinity of G has decreased to be lower

than A and C. The authors noted that the effect of secondary structure of G may affect the observed binding affinity.[57,58]

C. In addition to the above two experimental methods, Gourishankar *et al.* used isothermal titration calorimetry (ITC) to study the interaction of DNA bases with AuNP. The investigation revealed a binding sequence in the order C > G > A > T which is different from the previous two studies. The authors proposed that the difference between their study and the previous two were that the previous investigations used nucleosides rather than bases.[59] Additionally, other factors that may change the observed trend are possibly due to (1) the use of AuNPs which have a variety of facets and defects in the study and (2) solubility of the DNA bases, as some bases have low solubility in water in the absence of the phosphate and ribose group.

Most investigations to date have focused on the study of base interaction on Au (111) surfaces. However, the binding affinity of bases to Au might be expected to differ depending on the choice of Au facet, as the distance between atoms are different on different surface facets. There are limited studies comparing the relative binding affinities of DNA bases to other Au surfaces, such as (100) and (110). Bogdan *et al.* used density functional theory computations to determine the adsorption energy of the bases on Au (100). They compared the adsorption energy of the bases in in the parallel and perpendicular conformation on Au in the absence of solvent. The relative adsorption energy, ΔE_{ads} was reported to be in the order of G > A = C > T which was similar to the trend of desorption energy reported by Mirkin and coworkers.[60] Salvatore *et al.* investigated the adsorption of the four nucleobases A, C, G and T, on the Au (110) electrode surface using cyclic voltammetry (CV), electrochemically controlled scanning tunneling

microscopy (EC-STM), and density functional theory (DFT) calculations. DFT calculations with solvation effects reveal that adsorption energy on Au (110) surface is in the order of A > G > C > T.

1.3.2 Orientation of the base on gold surface

The orientations in which DNA bases bind to Au have been reported both through experimental and computational methods. The experimental method of determination involves Raman studies. These studies reveal the position of binding sites of the bases that coordinate to Au. The positions are indicated by blue arrows in figure 1.2.[40]

Binding of the adenine base occurs through two positions on the base: the N6 exocyclic amino group, and the N7 atom.[57,61] The attachment of adenine at N6-NH_2 coordinates to Au in an sp^3-like, strongly perturbed, nonplanar configuration.[55,56] Binding of cytosine to Au occurs via the N3 nitrogen atom of the pyrimidine ring and a partial interaction from the oxygen of the C2 carbonyl group.[61] Despite the presence of an N2 exocyclic group, binding of guanine is observed, via surface enhanced Raman scattering (SERS), to occur through lone pair of electrons from the C6 carbonyl and the N7 nitrogen atom.[62] The binding of thymine is weak and occurs through the dT oxygen of the C4 carbonyl group of the pyrimidine ring.[61]

The Raman detection method allows the determination of the binding sites, but not the orientation of the base on the surface. Therefore, computational modelling and experimental STM studies have been performed to simulate and investigate binding orientation of nucleobases on Au.[63-66] Typically in terms of simulation, two binding orientation of nucleobases on Au are compared, one consisting of vertical adsorption of the base and the other consisting of planar adsorption, parallel to the surface.

Based on scanning tunneling microscopy (STM) investigations, adenine assembles vertically into wormlike structures on Au (110) and (111) surfaces at pH 4.5, but lies flat on the surface of (110) at pH 2.5.[67] The ring structures formed at low pH are packed in the direction perpendicular to the direction of the stripes and grooves of Au atoms present on the Au (110) surface. This change is largely attributed to the singly protonated state of adenine at N7 which has pK_a of 4.2.[68] Cytosine assembles on the Au (110) surface at pH 2.5 by adopting a flat orientation, forming ring-like features.[67] This is in contrast to the vertical orientation observed at neutral pH.[69,70] Guanine forms a mixed conformation when assembled on Au (110) surface at pH 2.5 resulting in a disordered wormlike structure.[67] The interaction of guanine to Au is largely affected by the solubility of the base itself and the protonation state of the guanine with pK_{a1} of 3.4 and pK_{a2} of 9.2-9.6.[68] At low pH the guanine base is positively charged at the N7 position. Adsorption of thymine on Au (110) surfaces at low pH is in a planar orientation forming terraces.[67,71] The chemisorbed thymine occurs through bonding of both carbonyl functionalities and a deprotonated N3 to the Au (111) surface.[72]

Computational modeling allows the determination of the energy difference in each bound state. The metal−nucleobase bond energy in the planar orientation ranges from 0.5 to 1.0 eV with the base binding energy in decreasing order G > C > A > T. Simulations in the vertical orientation resulted in similar results, however it was noted the nucleobase is predicted to be tilted at an angle to the surface with higher tilt angle for G and lower tilt angle for C. Although there may be a preference of orientation, it was noted that the chemisorption free energy differences between the two orientations in a solvated state is small and likely to result in fast interconversion between the two orientations (Table 1.2).[67]

In addition to binding, the mobility of absorbed DNA nucleobases on Au (111) surfaces were modelled by Rapino and Zerbetto suggesting that the mobility varies with C > T ~ G > A. The mobility trend observed was not inversely proportional to the desorption energy. Rather, the motions of the nucleobase on Au are driven by the number of anchor points and exchange of position caused by mismatch of the distances of binding sites of the base with the Au lattice.[73] Despite the current studies of the orientation and binding sites of nucleobases on Au surfaces, the binding mode of homo-oligomers of nucleobases may differ due to steric constrains and backbone flexibility to allow optimal binding. In addition, the dynamic interaction between the base and the surface (i.e. migration, desorption and adsorption) are critical factors to consider in order to fully understand the interactions of DNA with Au.

1.4 Shape control of nanoparticle

While it was mentioned previously in section 1.2 that we have adopted the seeded growth method to successfully perform DNA mediated shape control of NP growth, this section focuses on the seeded synthesis method and factors that will influence growth of the seed particles.

1.4.1 Seeded growth of nanoparticles

In the synthesis of NPs, there are two main steps: nucleation and growth. In order to achieve monodisperse NP products, reaction conditions are typically tuned to generate a burst of nucleation followed by slower and controllable deposition. However, achieving this type of balanced condition for fast nucleation and slow growth conditions is tricky as continuous nucleation during the growth of the NPs can result in heterogeneity of the resulting NPs.[74,75] To solve the issue of homogeneity, a seeded method was introduced to separate the nucleation and growth steps.[75,76] As

a result, the NPs formed from the seeded growth method are more monodisperse in shape and size.[75-77]

This seeded method has since been exploited to allow the synthesis of various shapes of NPs by either introducing different seeds of single crystal or twinned crystal, or different ligands and additives in the growth step. The seed mediated method is widely adopted as the synthetic route to form AuNPs of various shapes and sizes using different protecting ligands, templates or ions, resulting in particles such as Au nanorods[78,79], Au nanocubes,[80], Au rhombic dodecahedra,[81] Au trisoctahedra,[82,83] Au hexapods[84], and Au tetrahexahedra.[85]

However, conditions for forming NPs are easily influenced by trace amount of impurities and slight variation in reaction conditions.[86,87] For example the presence of trace iodide prevents the formation of Au nanorods,[88] and trace bromide ions in combination with cetyltrimethylammonium chloride inhibits the synthesis of Au nanocubes.[83] Addition of small amounts of metal ions such as silver can lead to underpotential deposition resulting in alteration of the NP shapes formed.[89-91] To minimize variations in reaction conditions, it is important to understand the mechanism of growth.

1.4.2 Factors that affect nanoparticle synthesis

Based on our current knowledge of NP synthesis,[87] growth of NPs can be influenced by various factors: 1) binding affinity of the ligand, 2) speciation of the metal precursor, and 3) properties of the reductant. These factors are co-influenced by various physical parameters such as temperature, pH and concentration. Since the binding affinity of the ligand is specific to the ligand used, the binding affinity of DNA to Au is introduced in section 1.3. This section focuses

on the speciation of Au precursor and the reduction properties of hydroxylamine which are mainly used in this work.

1.4.2.1 Metal ion speciation

It has been demonstrated that the speciation of metal complexes will affect its reduction potential.[92-94] The reduction potential, whether for the Au(III)/Au(0), Au(III)/Au(I), or Au(I)/Au(0) redox pairs, have been reported to vary significantly for different Au complexes and ligands.[95] Wang *et al.* investigated the role of Au species in the synthesis of Au NPs by performing reduction at different pH. The species of Au was determined using ion chromatography method.[96] At pH 2.91, the reduction potential of the gold chloride precursor was 0.66 V while pH 6.16 and 8.01 resulted in reduction potentials of 0.59 V and 0.53 V. The reduction of $HAuCl_4$ at high pH is more difficult than that at low pH.[96] The reduction potential observed for oxidized Au species were also consistent with a report from Burke and Nugent.[97]

At high pH, $AuCl_4^-$ and $[AuCl_3(OH)]^-$ will be converted to less reactive $[AuCl_2(OH)_2]^-$ and $[AuCl(OH)_3]^-$. Ji *et al.* studied the role of citrate in Au reduction and observed a transition from one mechanism of growth to another between pH 6.2 and 6.5. At low pH, the mechanism consists of nucleation, interparticle fusion to form chains, smoothening of the chains and finally ripening into spheres. At pH above 6.5, the mechanism consists of nucleation and subsequent growth by monomer attachment resulting in monodisperse nanospheres. The authors proposed that change in mechanism observed was due to change in Au species from $[AuCl_3(OH)]^-$ to $[AuCl_2(OH)_2]^-$ and $[AuCl(OH)_3]^-$.[98] This observation was consistent with the decrease in reduction potential and a more homogenous growth. Similar observation was reported by Sivaraman *et al.* where a more homogenous growth was observed when they reversed the order of addition, adding citrate before

the Au precursor.[99] The increase in homogeneity upon changing the order of reactant addition was due to a shift of the overall reaction mixture to higher pH when the reaction takes place.[99]

Similar decrease in reduction rate was observed for reduction of Au(III) by CO where the reaction took longer at pH 9 compared to the reaction when at lower pH. The authors noted that the Au concentration would affect the acidity of the growth solution and hence Au speciation.[100] Lee *et al.* investigated the effect of pH on galvanic replacement of Ag by Au in which higher pH resulted in more controllable shapes. The authors attributed this to the decrease in reduction potential with increasing amount of hydrolysis.[101]

To characterize the species of Au, typically UV-Vis and Raman spectroscopy are used. At pH below 5 in the presence of 1 M NaCl, the species of Au is predominantly the square planar four-coordinated complex of chlorides, $[AuCl_4]^-$.[102] At pH about 5.8 it was observed that substitution of hydroxo- groups started to occur forming $[AuCl_3(OH)]^-$ and this species will dominate fully at pH 7.0. These results were concluded from the appearance of an Au-OH stretching frequency peak at 569 cm^{-1} when pH was increased. [102] The pH of this transition was also observed in the UV-Vis spectrum where at low pH the absorbance peak remains at 314 nm but begins to blue shift at pH > 5.[102] This absorbance peak is due to a ligand-metal charge transfer (LMCT) from π of chloride to σ^* of Au. An isosbestic point was observed at 300 nm in the pH range 5-6 indicating the transition from $[AuCl_4]^-$ to another species.[102,103] Similar observations were reported using other techniques such as Extended X-Ray Absorption Fine Structure (EXAFS) in studying the coordination of gold chloride at various pHs.[94]

In most studies, 1 M of NaCl is typically added to the reaction solution. In the absence of additional NaCl, it is expected that the reaction equilibria will shift and favor the hydroxo-

substituted complex and will thus affect the pH at which hydrolysis occurs (figure 1.3).[104] The reaction equilibria for the hydrolysis process is described below.

$$AuCl_4^- + H_2O \rightleftharpoons AuCl_3(OH)^- + H^+ + Cl^-$$

To reflect the true species of the Au precursor in water, Murphy and LaGrange investigated the hydrolysis process at different Au concentration in the absence of excess salt. By improving the resolution and reanalyzing the Raman peaks observed previously by Peck *et al.*, the authors assigned Raman peaks to each of the Au(III) hydroxo-chloride species with the peak numbers matching well with theoretical predictions (figure 1.4). The authors observed that the pH at which first hydrolysis occurs decreases with concentration of the Au salt. At a 5 mM concentration of $HAuCl_4$, the pH at which hydrolysis occurs to form $[AuCl_3(OH)]^-$ was observed to be between pH 2-3; while at a 1 mM concentration of $HAuCl_4$, $[AuCl_2(OH)_2]^-$ and $[AuCl(OH)_3]^-$ were formed even between pH 2.5-3.5.[105] This result indicates that the pH in which the hydrolysis species occur depends on the concentration of the Au in the absence of excess chloride.

1.4.2.2 Properties of the reductant

The rate of reduction has been reported to be influenced by pH in various systems corresponding to a lower reduction potential and a stronger oxidizing ability at high pH.[77,106-109] While there are a large variety of reductants, this introduction chapter focuses on a mild reductant hydroxylamine.

The reduction of $HAuCl_4$ in the presence of hydroxylamine at the concentration of 0.01% Au and 0.025% hydroxylamine does not occur spontaneously until Au seeds are present in the reaction.[110] Oxidation of hydroxylamine is observed to be catalyzed on the surface of Au as the oxidation peak was observed to be at 0.6 V for glassy carbon (GC) electrode but 0.245 V on Au/GC

electrode.[111] Electro-oxidation of hydroxylamine shows two oxidation peaks on rough Au surfaces.[112] Li and Lin reported that the hydroxylamine oxidation has an one-electron oxidation rate limiting step and the total number of electrons occurring in the oxidation process of hydroxylamine was 2 electrons.[111] Comparing the reduction on different Au surfaces, the activity of hydroxylamine on Au (100) surfaces were found to be higher than the activity on Au (111) or (110) which are facets with lower energy as a more negative onset potential for the oxidation of hydroxylamine was observed for Au (100).[113]

The autocatalytic deposition of Au by hydroxylamine has been observed in various occasions.[75,114] Using the property of hydroxylamine that reduces Au in the presence of a Au surfaces, AuNPs with controllable sizes and high monodispersity were synthesized using seeded methods.[76] The reaction of hydroxylamine would result in various oxidation products such as N_2, N_2O or NO_3^- depending on the specific oxidation conditions.[115] Hydroxylamine based reduction of silver has been investigated since 1939 as developing agents in photography. The reduction of silver by hydroxylamine was found to generate N_2 in non-alkaline conditions and the rate was found to be second order with respect to pH concentration. At pH 3.8, the rate of the reaction is approximately first order with respect to the hydroxylamine concentration but the dependence in concentration decrease with increase in pH. From the pH dependency of the reaction, it was proposed by James that the reactive reducing agent in the reaction is NH_2O^-.[116]

The reaction rates of hydroxylamine with iodine have been investigated by several groups. The mechanism of the reduction by NH_3OH^+ have been proposed to produce HNO_2 intermediates as well as N_2O and NO as products and the rate of reactions were monitored by the evolution of the reaction products.[117,118] The reaction rates for reduction of I_2 by hydroxylamine were found to be sensitive to pH. The rate of reactions were determined by stopped-flow in the presence of

acetate buffer as shown in Table 1.3.[119] The rates of the reaction increases rapidly even with minor changes in the pH of the solution. The authors demonstrated that the reaction rates accelerated in with increasing concentration of not only [OH^-] but also [NH_2OH], [NH_2OH]^2, [OAc^-], and [HPO_4^{2-}].[119] The reaction rate dependence of hydroxylamine was also observed for reduction of monochloramine.[120]

Simic and Hayon investigated the one-electron oxidation of hydroxylamine using hydroxyl radicals. The rate of the reaction with protonated form of hydroxylamine was determined to be slower at $k \leq 5.0 \times 10^8$ $M^{-1}s^{-1}$ while the rates with the unprotonated form was determined to be much faster at $k = 9.5 \times 10^9$ $M^{-1}s^{-1}$. The acid dissociation constant for the hydroxyamino radical was determined to be pK ($\cdot N^+H_2OH$) = 4.2.[121] The reaction with hydroxyl radicals were similar for the proposed mechanism of reduction of iron (III) where N_2O was observed as 80 % of the reaction by product.[122]

The one-electron oxidation of hydroxylamine is proposed to be

$$NH_2OH \rightarrow NH_2O\cdot + H^+ + e^-$$

$$NH_2O\cdot \rightarrow \frac{1}{2}N_2 + H_2O$$

$$NH_2OH \rightarrow \frac{1}{2}N_2 + H_2O + H^+ + e^- \quad (1)$$

While in excess of oxidant, the two-electron reduction is proposed to generate HNO, which will then dimerize to form N_2O.[111,123,124]

$$NH_2OH \rightarrow NH_2O\cdot + H^+ + e^-$$

$$NH_2O\cdot \rightarrow HNO + H^+ + e^-$$

$$HNO \rightarrow \frac{1}{2}N_2O + \frac{1}{2}H_2O$$

$$NH_2OH \rightarrow \frac{1}{2}N_2O + \frac{1}{2}H_2O + 2H^+ + 2e^- \quad (2)$$

1.5 References

(1) Lu, Z.; Yin, Y. *Chem. Soc. Rev.* **2012**, *41*, 6874.

(2) Nie, Z.; Petukhova, A.; Kumacheva, E. *Nature Nanotech.* **2010**, *5*, 15.

(3) Chen, X.-J.; Sanchez-Gaytan, B. L.; Qian, Z.; Park, S.-J. *Wiley Interdiscip. Rev. Nanomed. Nanobiotechnol.* **2012**, *4*, 273.

(4) Schroeder, A.; Heller, D. A.; Winslow, M. M.; Dahlman, J. E.; Pratt, G. W.; Langer, R.; Jacks, T.; Anderson, D. G. *Nat. Rev. Cancer* **2012**, *12*, 39.

(5) Xia, Y.; Xiong, Y.; Lim, B.; Skrabalak, S. E. *Angew. Chem. Int. Ed.* **2009**, *48*, 60.

(6) Fan, J. A.; Wu, C.; Bao, K.; Bao, J.; Bardhan, R.; Halas, N. J.; Manoharan, V. N.; Nordlander, P.; Shvets, G.; Capasso, F. *Science* **2010**, *328*, 1135.

(7) Halas, N. J.; Lal, S.; Chang, W.-S.; Link, S.; Nordlander, P. *Chem. Rev.* **2011**, *111*, 3913.

(8) Seeman, N. C. *Nature* **2003**, *421*, 427.

(9) Rothemund, P. W. K. *Nature* **2006**, *440*, 297.

(10) He, Y.; Ye, T.; Su, M.; Zhang, C.; Ribbe, A. E.; Jiang, W.; Mao, C. *Nature* **2008**, *452*, 198.

(11) Lo, P. K.; Karam, P.; Aldaye, F. A.; McLaughlin, C. K.; Hamblin, G. D.; Cosa, G.; Sleiman, H. F. *Nature Chem.* **2010**, *2*, 319.

(12) Pinheiro, A. V.; Han, D. R.; Shih, W. M.; Yan, H. *Nature Nanotech.* **2011**, *6*, 763.

(13) Fu, J. L.; Liu, M. H.; Liu, Y.; Yan, H. *Acc. Chem. Res.* **2012**, *45*, 1215.

(14) Ke, Y.; Ong, L. L.; Shih, W. M.; Yin, P. *Science* **2012**, *338*, 1177.

(15) Sacca, B.; Niemeyer, C. M. *Chem. Soc. Rev.* **2011**, *40*, 5910.

(16) Stadler, A.; Chi, C.; van der Lelie, D.; Gang, O. *Nanomedicine* **2010**, *5*, 319.

(17) Li, L.-L.; Wu, P.; Hwang, K.; Lu, Y. *J. Am. Chem. Soc.* **2013**, *135*, 2411.

(18) Kumar, A.; Hwang, J.-H.; Kumar, S.; Nam, J.-M. *Chem. Commun.* **2013**, *49*, 2597.

(19) Lim, D.-K.; Jeon, K.-S.; Hwang, J.-H.; Kim, H.; Kwon, S.; Suh, Y. D.; Nam, J.-M. *Nat. Nanotechnol.* **2011**, *6*, 452.

(20) Zhang, Y.; Lu, F.; Yager, K. G.; van der Lelie, D.; Gang, O. *Nature Nanotech.* **2013**, *8*, 865.

(21) Tan, S. J.; Campolongo, M. J.; Luo, D.; Cheng, W. *Nat. Nanotechnol.* **2011**, *6*, 268.

(22) Macfarlane, R. J.; Lee, B.; Jones, M. R.; Harris, N.; Schatz, G. C.; Mirkin, C. A. *Science* **2011**, *334*, 204.

(23) Kuzyk, A.; Schreiber, R.; Fan, Z.; Pardatscher, G.; Roller, E.-M.; Hogele, A.; Simmel, F. C.; Govorov, A. O.; Liedl, T. *Nature* **2012**, *483*, 311.

(24) Surwade, S. P.; Zhou, F.; Wei, B.; Sun, W.; Powell, A.; O'Donnell, C.; Yin, P.; Liu, H. *J. Am. Chem. Soc.* **2013**, *135*, 6778.

(25) Alivisatos, A. P.; Johnsson, K. P.; Peng, X.; Wilson, T. E.; Loweth, C. J.; Bruchez, M. P.; Schultz, P. G. *Nature* **1996**, *382*, 609.

(26) Mirkin, C. A.; Letsinger, R. L.; Mucic, R. C.; Storhoff, J. J. *Nature* **1996**, *382*, 607.

(27) Wang, Z. D.; Lu, Y. *J. Mater. Chem.* **2009**, *19*, 1788.

(28) Sperling, R. A.; Rivera gil, P.; Zhang, F.; Zanella, M.; Parak, W. J. *Chem. Soc. Rev.* **2008**, *37*, 1896.

(29) Li, L.-L.; Zhang, R.; Yin, L.; Zheng, K.; Qin, W.; Selvin, P. R.; Lu, Y. *Angew. Chem. Int. Ed.* **2012**, *51*, 6121.

(30) Mertig, M.; Ciacchi, L. C.; Seidel, R.; Pompe, W.; De Vita, A. *Nano Lett.* **2002**, *2*, 841.

(31) Richards, C. I.; Choi, S.; Hsiang, J.-C.; Antoku, Y.; Vosch, T.; Bongiorno, A.; Tzeng, Y.-L.; Dickson, R. M. *J. Am. Chem. Soc.* **2008**, *130*, 5038.

(32) Rotaru, A.; Dutta, S.; Jentzsch, E.; Gothelf, K.; Mokhir, A. *Angew. Chem. Int. Ed.* **2010**, *49*, 5665.

(33) Tikhomirov, G.; Hoogland, S.; Lee, P. E.; Fischer, A.; Sargent, E. H.; Kelley, S. O. *Nat. Nanotechnol.* **2011**, *6*, 485.

(34) Choi, S.; Dickson, R. M.; Yu, J. *Chem Soc Rev* **2012**, *41*, 1867.

(35) Zhao, B.; Shen, J.; Chen, S.; Wang, D.; Li, F.; Mathur, S.; Song, S.; Fan, C. *Chem. Sci.* **2014**, *5*, 4460.

(36) Oh, J.-W.; Lim, D.-K.; Kim, G.-H.; Suh, Y. D.; Nam, J.-M. *J. Am. Chem. Soc.* **2014**, *136*, 14052.

(37) Wang, Z.; Zhang, J.; Ekman, J. M.; Kenis, P. J. A.; Lu, Y. *Nano Lett.* **2010**, *10*, 1886.

(38) Wang, Z.; Tang, L.; Tan, L. H.; Li, J.; Lu, Y. *Angew. Chem. Int. Ed.* **2012**, *51*, 9078.

(39) Wu, J.; Tan, L. H.; Hwang, K.; Xing, H.; Wu, P.; Li, W.; Lu, Y. *J. Am. Chem. Soc.* **2014**, *136*, 15195.

(40) Liu, J. *Phys. Chem. Chem. Phys.* **2012**, *14*, 10485.

(41) Storhoff, J. J.; Elghanian, R.; Mirkin, C. A.; Letsinger, R. L. *Langmuir* **2002**, *18*, 6666.

(42) Kryachko, E. S. In *Quantum Biochemistry*; Wiley-VCH Verlag GmbH & Co. KGaA: 2010, p 245.

(43) Nelson, E. M.; Rothberg, L. J. *Langmuir* **2011**, *27*, 1770.

(44) Zhang, X.; Servos, M. R.; Liu, J. *Langmuir* **2012**, *28*, 3896.

(45) Zhang, X.; Liu, B.; Dave, N.; Servos, M. R.; Liu, J. *Langmuir* **2012**, *28*, 17053.

(46) Wolf, L. K.; Gao, Y.; Georgiadis, R. M. *Langmuir* **2004**, *20*, 3357.

(47) Zhao, W.; Lee, T. M. H.; Leung, S. S. Y.; Hsing, I. M. *Langmuir* **2007**, *23*, 7143.

(48) Berti, L.; Burley, G. A. *Nat. Nanotechnol.* **2008**, *3*, 81.

(49) Izatt, R. M.; Christensen, J. J.; Rytting, J. H. *Chem. Rev.* **1971**, *71*, 439.

(50) Erdmann, M.; David, R.; Fornof, A. R.; Gaub, H. E. *Nat. Chem.* **2010**, *2*, 745.

(51) Basu, S.; Jana, S.; Pande, S.; Pal, T. *J. Colloid Interface Sci.* **2008**, *321*, 288.

(52) Reedijk, J. *Proc. Natl. Acad. Sci.* **2003**, *100*, 3611.

(53) Miyake, Y.; Togashi, H.; Tashiro, M.; Yamaguchi, H.; Oda, S.; Kudo, M.; Tanaka, Y.; Kondo, Y.; Sawa, R.; Fujimoto, T.; Machinami, T.; Ono, A. *J. Am. Chem. Soc.* **2006**, *128*, 2172.

(54) Yamane, T.; Davidson, N. *J. Am. Chem. Soc.* **1961**, *83*, 2599.

(55) Demers, L. M.; Östblom, M.; Zhang, H.; Jang, N.-H.; Liedberg, B.; Mirkin, C. A. *J. Am. Chem. Soc.* **2002**, *124*, 11248.

(56) Östblom, M.; Liedberg, B.; Demers, L. M.; Mirkin, C. A. *J. Phys. Chem. B* **2005**, *109*, 15150.

(57) Kimura-Suda, H.; Petrovykh, D. Y.; Tarlov, M. J.; Whitman, L. J. *J. Am. Chem. Soc.* **2003**, *125*, 9014.

(58) Parkinson, G. N.; Lee, M. P. H.; Neidle, S. *Nature* **2002**, *417*, 876.

(59) Gourishankar, A.; Shukla, S.; Ganesh, K. N.; Sastry, M. *J. Am. Chem. Soc.* **2004**, *126*, 13186.

(60) Bogdan, D.; Morari, C. *J. Phys. Chem. C* **2012**, *116*, 7351.

(61) Jang, N.-H. *Bull. Korean Chem. Soc.* **2002**, *23*, 1790.

(62) Pergolese, B.; Bonifacio, A.; Bigotto, A. *Phys. Chem. Chem. Phys.* **2005**, *7*, 3610.

(63) Piana, S.; Bilic, A. *J. Phys. Chem. B* **2006**, *110*, 23467.

(64) Lv, G.; Wei, F.; Jiang, H.; Zhou, Y.; Wang, X. *J. Mol. Struc. Theochem* **2009**, *915*, 98.

(65) Lv, G.; Wei, F.; Li, Q.; Shen, Q.; Jiang, H.; Zhou, Y.; Wang, X. *J. Nanosci. Nanotechnol.* **2010**, *10*, 809.

(66) Sandig, N.; Zerbetto, F. *Chem. Commun.* **2010**, *46*, 667.

(67) Salvatore, P.; Nazmutdinov, R. R.; Ulstrup, J.; Zhang, J. *J. Phys. Chem. B* **2015**, *119*, 3123.

(68) Verdolino, V.; Cammi, R.; Munk, B. H.; Schlegel, H. B. *J. Phys. Chem. B* **2008**, *112*, 16860.

(69) Mansley, C. P.; Smith, C. I.; Bowfield, A.; Fernig, D. G.; Edwards, C.; Weightman, P. *J. Chem. Phys.* **2010**, *132*, 214708.

(70) Weightman, P.; Dolan, G. J.; Smith, C. I.; Cuquerella, M. C.; Almond, N. J.; Farrell, T.; Fernig, D. G.; Edwards, C.; Martin, D. S. *Phys. Rev. Lett.* **2006**, *96*, 086102.

(71) Roelfs, B.; Bunge, E.; Schröter, C.; Solomun, T.; Meyer, H.; Nichols, R. J.; Baumgärtel, H. *J. Phys. Chem. B* **1997**, *101*, 754.

(72) Haiss, W.; Roelfs, B.; Port, S. N.; Bunge, E.; Baumgärtel, H.; Nichols, R. J. *J. Electroanal. Chem.* **1998**, *454*, 107.

(73) Rapino, S.; Zerbetto, F. *Langmuir* **2005**, *21*, 2512.

(74) Wiesner, J.; Wokaun, A. *Chem. Phys. Lett.* **1989**, *157*, 569.

(75) Jana, N. R.; Gearheart, L.; Murphy, C. J. *Chem. Mater.* **2001**, *13*, 2313.

(76) Brown, K. R.; Walter, D. G.; Natan, M. J. *Chem. Mater.* **2000**, *12*, 306.

(77) Perrault, S. D.; Chan, W. C. W. *J. Am. Chem. Soc.* **2009**, *131*, 17042.

(78) Jana, N. R.; Gearheart, L.; Murphy, C. J. *J. Phys. Chem. B* **2001**, *105*, 4065.

(79) Nikoobakht, B.; El-Sayed, M. A. *Chem. Mater.* **2003**, *15*, 1957.

(80) Niu, W.; Zheng, S.; Wang, D.; Liu, X.; Li, H.; Han, S.; Chen, J.; Tang, Z.; Xu, G. *J. Am. Chem. Soc.* **2009**, *131*, 697.

(81) Jeong, G. H.; Kim, M.; Lee, Y. W.; Choi, W.; Oh, W. T.; Park, Q. H.; Han, S. W. *J. Am. Chem. Soc.* **2009**, *131*, 1672.

(82) Ma, Y.; Kuang, Q.; Jiang, Z.; Xie, Z.; Huang, R.; Zheng, L. *Angew. Chem. Int. Ed.* **2008**, *47*, 8901.

(83) Wu, H.-L.; Kuo, C.-H.; Huang, M. H. *Langmuir* **2010**, *26*, 12307.

(84) Kim, D. Y.; Yu, T.; Cho, E. C.; Ma, Y.; Park, O. O.; Xia, Y. *Angew. Chem. Int. Ed.* **2011**, *50*, 6328.

(85) Ming, T.; Feng, W.; Tang, Q.; Wang, F.; Sun, L.; Wang, J.; Yan, C. *J. Am. Chem. Soc.* **2009**, *131*, 16350.

(86) Sau, T. K.; Murphy, C. J. *J. Am. Chem. Soc.* **2004**, *126*, 8648.

(87) Personick, M. L.; Mirkin, C. A. *J. Am. Chem. Soc.* **2013**, *135*, 18238.

(88) Smith, D. K.; Korgel, B. A. *Langmuir* **2008**, *24*, 644.

(89) Grzelczak, M.; Perez-Juste, J.; Mulvaney, P.; Liz-Marzan, L. M. *Chem Soc Rev* **2008**, *37*, 1783.

(90) Zhao, P.; Li, N.; Astruc, D. *Coord. Chem. Rev.* **2013**, *257*, 638.

(91) Personick, M. L.; Langille, M. R.; Zhang, J.; Mirkin, C. A. *Nano Lett.* **2011**, *11*, 3394.

(92) Hubbard, A. T.; Anson, F. C. *Anal. Chem.* **1966**, *38*, 1887.

(93) Straney, P. J.; Marbella, L. E.; Andolina, C. M.; Nuhfer, N. T.; Millstone, J. E. *J. Am. Chem. Soc.* **2014**, *136*, 7873.

(94) Spieker, W. A.; Liu, J.; Miller, J. T.; Kropf, A. J.; Regalbuto, J. R. *Appl. Catal. A-Gen* **2002**, *232*, 219.

(95) Kohl, P. A. In *Modern Electroplating*; John Wiley & Sons, Inc.: 2010, p 115.

(96) Wang, S.; Qian, K.; Bi, X.; Huang, W. *J. Phys. Chem. C* **2009**, *113*, 6505.

(97) Burke, L. D.; Nugent, P. F. *Gold Bull.* **1997**, *30*, 43.

(98) Ji, X.; Song, X.; Li, J.; Bai, Y.; Yang, W.; Peng, X. *J. Am. Chem. Soc.* **2007**, *129*, 13939.

(99) Sivaraman, S. K.; Kumar, S.; Santhanam, V. *J. Colloid Interface Sci.* **2011**, *361*, 543.

(100) Young, J.; Lewinski, N.; Langsner, R.; Kennedy, L.; Satyanarayan, A.; Nammalvar, V.; Lin, A.; Drezek, R. *Nanoscale Res. Lett.* **2011**, *6*, 428.

(101) Lee, K.-J.; Lee, Y.-I.; Lee, J.; Myung, N. V.; Choa, Y.-H. *Curr. Appl. Phys.* **2012**, *12, Supplement 2*, S53.

(102) Peck, J. A.; Tait, C. D.; Swanson, B. I.; Brown Jr, G. E. *Geochim. Cosmochim. Acta* **1991**, *55*, 671.

(103) Usher, A.; McPhail, D. C.; Brugger, J. *Geochim. Cosmochim. Acta* **2009**, *73*, 3359.

(104) Moreau, F.; Bond, G. C.; Taylor, A. O. *J. Catal.* **2005**, *231*, 105.

(105) Murphy, P. J.; LaGrange, M. S. *Geochim. Cosmochim. Acta* **1998**, *62*, 3515.

(106) Miwa, Y.; Zinchenko, A.; Lopatina, L. I.; Sergeyev, V. G.; Murata, S. *Polym. Int.* **2014**, *63*, 1566.

(107) Vo, K. D. N.; Guillon, E.; Dupont, L.; Kowandy, C.; Coqueret, X. *J. Phys. Chem. C* **2014**, *118*, 4465.

(108) Tang, J.; Huang, J.; Man, S.-Q. *Spectrochim. Acta A Mol. Biomol. Spectrosc.* **2013**, *103*, 349.

(109) Scaravelli, R. C. B.; Dazzi, R. L.; Giacomelli, F. C.; Machado, G.; Giacomelli, C.; Schmidt, V. *J. Colloid Interface Sci.* **2013**, *397*, 114.

(110) Turkevich, J.; Stevenson, P. C.; Hillier, J. *J. Phys. Chem.* **1953**, *57*, 670.

(111) Li, J.; Lin, X. *Sens. Actuators B Chem.* **2007**, *126*, 527.

(112) Godoi, D. R. M.; Chen, Y.; Zhu, H.; Scherson, D. *Langmuir* **2010**, *26*, 15711.

(113) Jebaraj, A. J. J.; Martins de Godoi, D. R.; Scherson, D. A. *ACS Catalysis* **2012**, *2*, 911.

(114) Stremsdoerfer, G.; Perrot, H.; Martin, J. R.; Cléchet, P. *J. Electrochem. Soc.* **1988**, *135*, 2881.

(115) Makarycheva-Mikhailova, A. V.; Stanbury, D. M.; McKee, M. L. *J. Phys. Chem. B* **2007**, *111*, 6942.

(116) James, T. H. *J. Am. Chem. Soc.* **1939**, *61*, 2379.

(117) Rabai, G.; Beck, M. T. *J. Chem. Soc., Dalton Trans.* **1982**, 573.

(118) Coumes, C. C. D.; Chopin-Dumas, J.; Devisme, F. *Int. J. Chem. Kinet.* **1998**, *30*, 785.

(119) Liu, R. M.; McDonald, M. R.; Margerum, D. W. *Inorg. Chem.* **1995**, *34*, 6093.

(120) Robinson, D. M.; Hoppe, T. J.; Paslay, T. J.; Purser, G. H. *Int. J. Chem. Kinet.* **2006**, *38*, 124.

(121) Simic, M.; Hayon, E. *J. Am. Chem. Soc.* **1971**, *93*, 5982.

(122) Butler, J. H.; Gordon, L. I. *Inorg. Chem.* **1986**, *25*, 4573.

(123) Bengtsson, G.; Fronaeus, S.; Bengtsson-Kloo, L. *J. Chem. Soc., Dalton Trans.* **2002**, 2548.

(124) Kannan, P.; John, S. A. *Anal. Chim. Acta* **2010**, *663*, 158.

(125) Tan, L. H.; Xing, H.; Lu, Y. *Acc. Chem. Res.* **2014**, *47*, 1881.

1.6 Figures

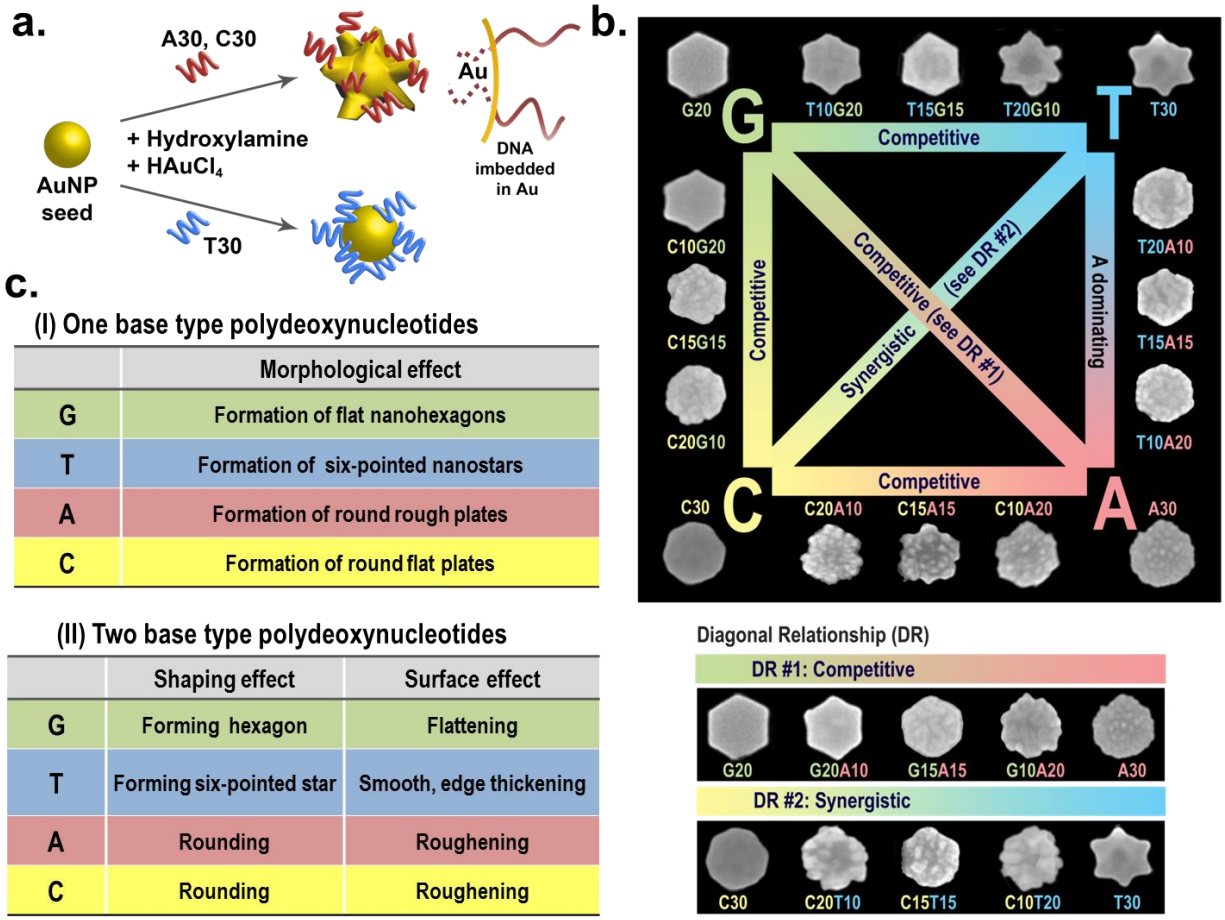

c.

(I) One base type polydeoxynucleotides

	Morphological effect
G	Formation of flat nanohexagons
T	Formation of six-pointed nanostars
A	Formation of round rough plates
C	Formation of round flat plates

(II) Two base type polydeoxynucleotides

	Shaping effect	Surface effect
G	Forming hexagon	Flattening
T	Forming six-pointed star	Smooth, edge thickening
A	Rounding	Roughening
C	Rounding	Roughening

Figure 1.1. (a) Shape-controlled growth of AuNP with spherical seeds and DNA of A30, C30 and T30 into Au nanoflowers and Au nanospheres. Enhanced stability of Au nanoflowers attributed to partially embedded DNA in Au surface. (b) Schematic summarizing AuNPs shapes grown from Au prism seeds with different DNA sequences and the relationship between different base combinations in governing growth process. (c) Table summarizing the rules of different DNA bases and their combinations in controlling AuNP morphology. Adopted from ref. 125.[125]

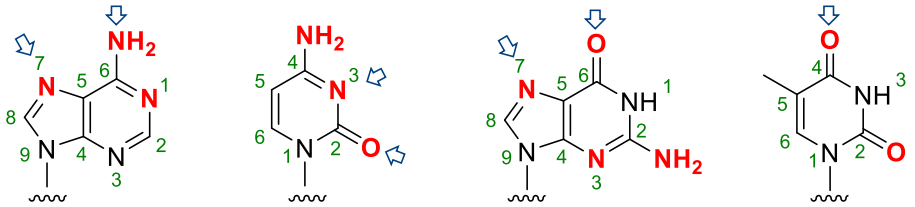

Figure 1.2. Possible binding sites of DNA bases adenine (A), cytosine (C), guanine (G) and thymine (T) to metal indicated in red. The blue arrows indicate positions where adsorption to Au occurs. Adopted from ref. 40 and 42.[40,42]

Table 1.1. Heats of desorption (ΔH_{des}) in kJ/mol) of DNA bases and 2-deoxyribnucleosides from Au (111) surfaces. Adopted from ref. 55.[55]

	ΔH_{des}(kJ mol^{-1}) nucleobases		ΔH_{des} (kJ mol^{-1}) 2'deoxyribonucleosides
	TPD mass trace[a]	IR[b]	IR
thymine	111 ± 2[c]	110 ± 2	109 ± 3
cytosine	128 ± 4	130 ± 5	114 ± 2
adenine	131 ± 3	129 ± 4	112 ± 4
guanine	146 ± 2	144 ± 2	120 ± 2

[a] ΔH_{des} values calculated using Redhead's equation for T (K) at mass spectrum peak maxima.[9] [b] ΔH_{des} values calculated from normalized peak area profile from RAIR spectra using T at 50% loss of material and Redhead's equation. [c] Number of samples was at least 3.

Table 1.2. Summarized surface orientation of DNA nucleobases on Au (110) surfaces at different pH. Adopted from ref. 67.[67]

	surface orientation at		
	pH 2.5	pH 4.5	pH 6.5
adenine	planar	vertical	
cytosine	planar		planar
guanine	disordered		vertical
thymine	planar		

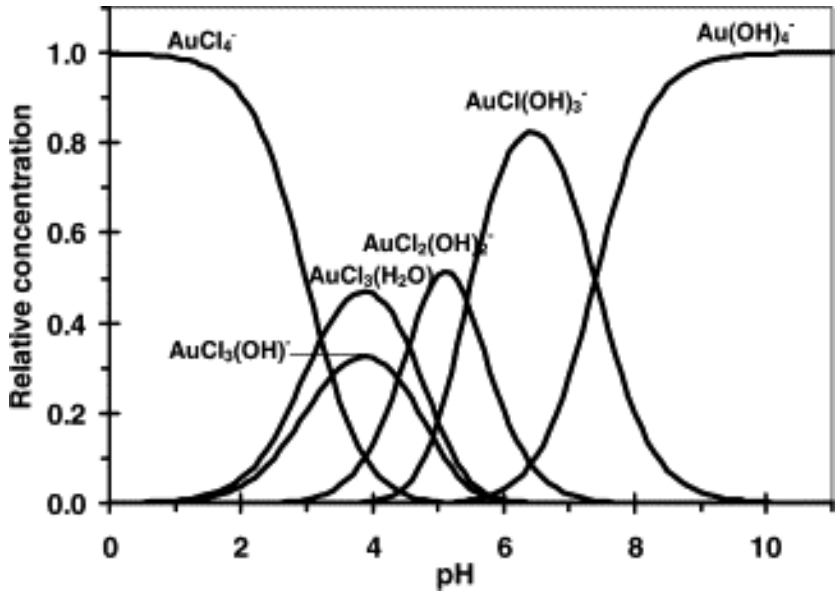

Figure 1.3. Species of Au complexes at Cl^- concentration of 2.5 mM at various pH. Figure adopted from ref. 104.[104]

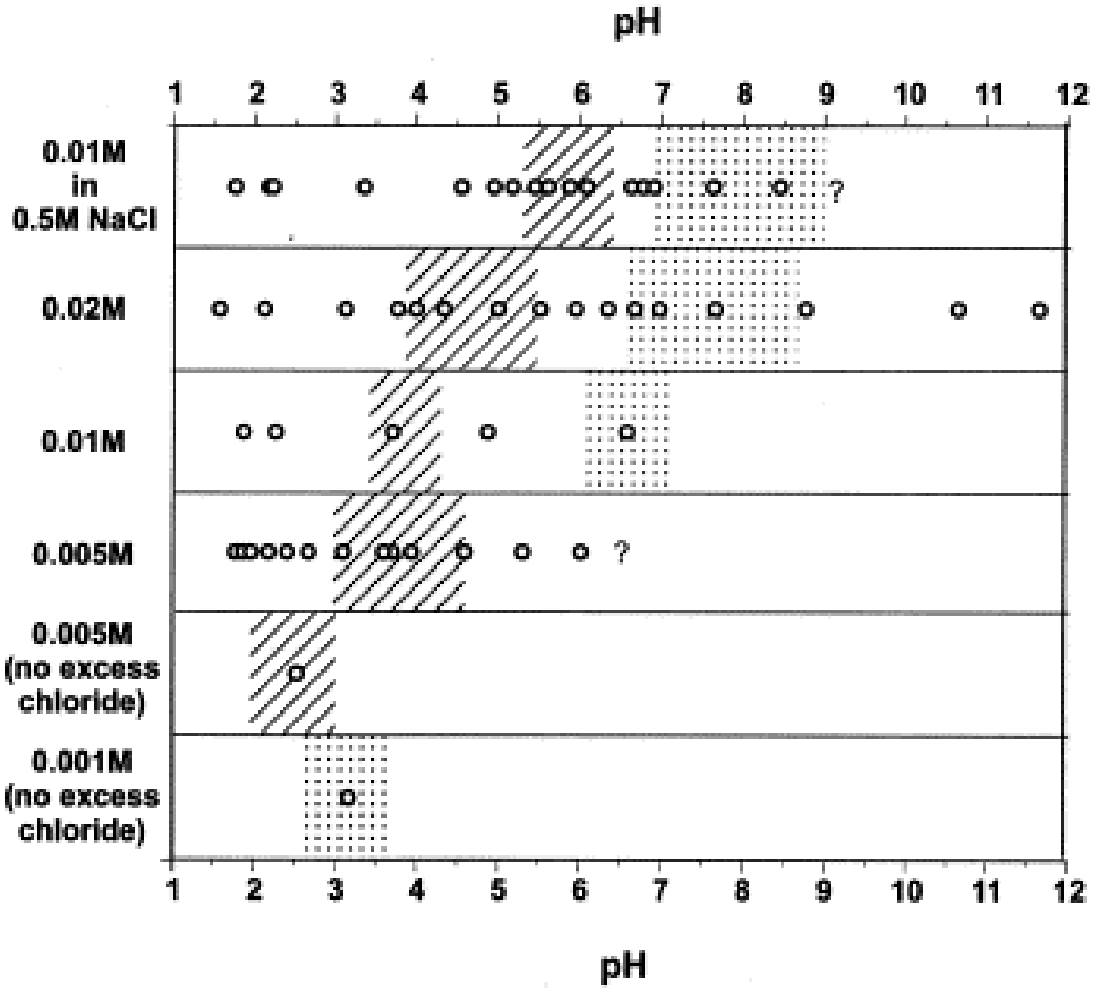

Figure 1.4. The speciation of Au determined from Raman spectroscopy mesurements of various complex concentration with respect to pH and in the presence/absence of excess chloride ions. The hashed area refers to the presence of $[AuCl_3(OH)]^-$ complex while the dotted areas incdicate the presence of $[AuCl_2(OH)_2]^-$ and $[AuCl(OH)_3]^-$ complexes coexisting in the solution. Figure adopted from ref. 102.[102]

Table 1.3. Reaction rates measured using stopped-flow methods at various pH values. Table adopted from ref. 119.[119]

p[H+]	$[NH_2OH]_T$, mM	k_r,[b] s^{-1}	p[H+]	$[NH_2OH]_T$, mM	k_r,[b] s^{-1}
3.44	10.13	0.851 ± 0.008	4.49	9.802	40.9 ± 0.4
3.67	10.13	2.22 ± 0.002	4.57	9.802	53.8 ± 0.7
3.82	10.13	3.89 ± 0.13	4.66	9.802	71.9 ± 0.7
4.00	10.13	8.22 ± 0.11	4.76	9.802	99 ± 1
4.18	10.13	16.2 ± 0.4	4.87	9.802	139 ± 3
4.27	10.13	23.1 ± 0.3	4.98	9.802	196 ± 6

[a] Conditions: 25.0 ± 0.1 °C; μ = 0.50 M ($NaClO_4$); λ = 353 nm; $[I^-]$ = 0.010 M; $[I_2]_T = 2.1 \times 10^{-5}$ M; $[HOAc]_T$ = 0.20 M. [b] Experimental stopped-flow rate constants (k_{exptl}) larger than 50 s^{-1} were corrected for mixing limitations of the instruments by using $k_r = k_{exptl}/(1 - (k_{exptl}/k_{mix}))$, where $k_{mix} = 2900\ s^{-1}$ for the Hi-Tech and $k_{mix} = 5276\ s^{-1}$ for the Durrum.

CHAPTER 2

A MECHANISTIC INSIGHT TO DNA-GUIDED SHAPE CONTROL OF NANOPARTICLES

2. 1 Introduction

The use of biomaterials, such as DNA, for precise engineering nanomaterials is becoming a promising field due to the programmability of these ligands and their specific molecular recognition properties.[1-5] Through the nitrogen and oxygen functional groups on the bases and electrostatic interactions, deoxyribonucleic acids (DNA) have shown sequence-dependent affinity with gold,[6-8] silver,[9,10], quantum dots[11-13] and carbon nanoparticles.[14] Recently we have reported the use of DNA oligonucleotides to encode the growth of nanoparticle seeds into various shapes depending on the DNA sequences.[7,8,15] The control over shape of nanoparticles is important as the properties of the nanoparticles are shape- dependent due to quantum confinement effects.[16] This property influences the use of the particles for various applications optical,[17-25] biomedical,[26-28] sensing,[29-33] and catalytic applications.[34-37] Despite the diversity of ligands and additives[38-47] used in nanoparticle synthesis, it remains challenging to systematically tune the shape of the nanoparticles. This challenge arises from the limited fundamental understanding of the growth mechanism of nanoparticles in the presence of different ligands.

Specifically, with the use of gold nanoprism (AuNPr) seeds, oligonucleotides consisting of poly-adenine (A) successfully guided the growth into round rough plates, poly-thymine (T) formed six pointed stars, poly-cytosine (C) formed round flat plates while poly-guanine (G) formed flat hexagons.[8] The use of oligonucleotides for synthesis not only results in four different shapes, we have also demonstrated the ability to fine-tune the transition from one shape to another using

combinations of two bases. This property to tune the shape is unique and difficult to achieve by typical ligands or by mixing two different ligands together.[48,49] DNA with its programmable nature offers excellent control over the sequence and length. Each of the four different bases has different binding affinity with the metal nanoparticle allowing fine-tuning of the interaction between DNA ligands with nanoparticles.[50] This system has demonstrated unprecedented control over nanoparticle synthesis.

Understanding how to obtain such fine control is important to allow better control over tuning the shape of colloidal nanoparticles. The syntheses of nanoparticles with controllable shapes are typically tricky as the growth is highly sensitive to variations in reactants. This makes fine tuning of the shapes even more difficult to achieve.[51] Having demonstrated the ability to finely control the growth of nanoparticles using DNA, this growth platform serves as an excellent system for us to understand the mechanism of growth of nanoparticles into different shape and identify the origin for such fine control. In an attempt to understand the programmable growth of the AuPr, we 1) studied the evolution of the AuPr in presence of the four DNA bases, into their respective shapes at different time points, 2) investigated the role of DNA in the growth and 3) probed the location of DNA on the nanoparticles. Finally, based on our investigations, we propose a three stage growth mechanism that permits DNA to finely control the nanoparticle shape.

2.2 Results and Discussions

Morphological evolution and kinetic UV-vis studies of the nanoparticle growth

The DNA mediated growth of nanoparticles was performed using homopolymeric sequence of DNA (T30, G20, C30 and A30) on gold nanoprisms of 100 nm in diameter (Figure 2.1a). A sequence of only 20 bases of guanine was used due to difficulties in synthesizing long

guanine oligos. The reaction was performed by firstly incubating the DNA with the nanoprism seeds for about 15 min. Subsequently, reductant hydroxylamine and precursor chloroauric acid was added to the growth solution (Figure 2.1a). The reaction was left to stand for at least 30 minutes to ensure completion of the growth. To elucidate the growth transformation from gold nanoprisms into the four different shapes guided by the four DNA bases, we performed simultaneous time dependent experiments to study morphological evolution and kinetic UV-vis absorbance of the growth.

To understand how the morphology evolves with time, a kinetic quenching experiment was conducted. Excess of mercaptopropionic acid were added to the growth mixture to stop the growth at desired time points. The presence of excess mercaptopropionic acid would bind the unreacted gold precursor and prevent further deposition of gold on the nanoparticle surfaces,[8] hence the morphology of nanoparticles at various time points can be observed. The quenched nanoparticles were washed and observed under SEM. The morphological evolution of the particle grown with T30, G20, C30 and A30 are shown in Figure 2.1b. (large area view of the nanoparticles are provide in SI, Figure 2.2, 2.3, 2.4 and 2.5). For the transition in to six pointed star with T30, the nanoparticle first grew into a polygon (nonagon or dodecagon) shaped plate. The particles then gradually transformed into hexagonal shape and retained the shape between 3 min to 5 min (Figure 2.1b). At 7^{th} min, the quenching experiment showed the appearance of pointed edges, forming from the edges of the hexagon. The six-point edges became more prominent with time at 10 min and thereafter the growth became gradual. The overall morphological evolution for T30 observed were triangle prisms to nonagon shape, hexagon shape and finally six-pointed stars.

The final shapes of the nanoparticles G20, C30 and A30 were formed within 5 min of the growth. Nanoparticles grown with G20 adopted the hexagonal structure observed within 3-5 min.

On the other hand, A30 and C30 grew into polygon shapes within 2-3 min and retained the shape throughout the growth duration. The final shape of the nanoparticles grown with G20, C30, and A30 were intermediate shapes observed during the growth of T30. The duration and time it took for defined shapes to form were also similar, where 3-5 min were observed for hexagon formation and 2-3 min for observation of round polygon particles. In addition to the changes in shape, roughness was observed to form on the particle surface for A30 around the 10^{th} min and became rougher with time.

Simultaneous kinetic UV-vis investigation to monitor the growth process was performed to correlate the observed structures with the changes in plasmonic features. Due to the plasmonic properties of AuNP, the absorbance of the nanoparticle was highly dependent on the morphology and size.[52-54] The absorbance of the nanoparticle grown with T30 was monitored at intervals of 1 min for 30 mins (Figure 2.1c, 2.6a). As the growth proceeded, the maximum absorbance wavelength (λ_{max}) blue-shifted in the first minute and subsequently red-shifted. The blue shift of the maximum absorbance peak in the initial 1-2 min is consistent with the rounding of the particles.[55] While the absorbance intensity increased with time, the λ_{max} appears to be consistent after 10 min of growth suggesting that very little morphological change occurs after 10 min. To clearly observe the change, we plotted the λ_{max} with time (Figure 2.1d).The λ_{max} of the gold nanoprism, initially at 828 nm, firstly blue shifted to 812 nm in the 1^{st} minute and subsequently red shifted till 3^{rd} min to 866 nm. It is interesting to note that there was a plateau with no change in λ_{max} from the 3^{rd} to 6^{th} min but an increase in the absorbance value (Figure 2.1c). This plateau was consistent with no shape change in observed in Figure 2.1b for 3 min and 5 min showing the formation of hexagonal shaped particles. After the growth at 6^{th}min, the λ_{max} continued to red-shift to 960 nm until the 8^{th} min and remained consistent for the rest of the test duration. The absorbance

at the transition of 7thmin showed a broadening and red shifting of the absorbance peak (Figure 2.1c). At this transition of 7 min, the morphology of the nanoparticle was observed to have some growth at the tips of the hexagon which indicates the start of the formation into six-pointed stars. These UV-vis kinetic experiments suggest a two step-growth observed for the growth of T30 nanoparticle where one shape would be observed between 3rd-6th min and the final growth is completed within 10 min. This corresponds well with the morphological changes where, hexagons were observed as an intermediate at the 3rd and the 5th min before transiting into six-pointed stars.

UV-vis kinetic experiments for G20, C30 and A30 are shown in Figure 2.1d, 2.6b, 2.6c and 2.6d. The final λ_{max} for T30 and G20 were observed to both red-shift (960 nm and 841 nm, respectively) from the initial λ_{max} of AuNPr (828 nm) while A30 and C30 have λ_{max} value blue-shifted to 748nm and 704 nm respectively (Figure 2.1d). It is noted that the λ_{max} for G20 was similar to the first plateau observed for the growth in T30 at 866 nm consistent with the formation of hexagonal shape nanoparticle. The λ_{max} of A30 blue shifted in the first 3 min and remain relatively constant while λ_{max} of C30 constantly blue-shifts slowly throughout the growth. The final λ_{max} observed for each of the nanoparticles grown with the four different sequences were as expected as the larger size nanoparticle showed a larger λ_{max}.[53]

The growth dimensions of the nanoparticles at various time points were plotted in Figure 2.8e to allow tracking of the growth progression. All the bases show similar increase in the diameter prior to a sudden halt in lateral growth at different times for different bases. The growth stops at earlier times for A and C followed by G and finally T. The measured diameters of the particles at the end of growth were 220 ± 20 nm for T30, 170 ±10 nm for G20, 155 ±10 nm for A30 and 129 ± 5 nm for C30 which corresponds well with the trend of λ_{max} observed where C30< A30< G20< T30. We note that an increase in thickness was observed for A30> C30> G20>T30.

While most of the changes in diameter of the particles were noted to be completed within 7 min of growth, the thickness of the nanoparticle grew at similar rates at the initial 7 min but started to grow at different rates for different bases after 7^{th} min. The growth of thickness occurs at a longer time frame than the growth of the diameter. Comparing both the change in thickness and the change in diameter, we noticed two growth steps where rapid growth in the diameter first takes place and stops followed by growth of the thickness.

We noticed that the trend of the time taken for the shape formation for each sequence is related to the binding affinity of the DNA bases to gold in the order of T< G< C< A, determined from competitive binding experiments reported by Tarlov and coworkers.[56,57] The higher binding affinity plays a role in blocking the nanoparticle growth on the sides resulting in an overall smaller nanoparticle diameter and thicker particle. In addition to the shape, one additional factor to note is the roughness. A30 was the only base to result in roughness of particles grown and the roughness were only observed between 10-15 min of growth. This roughness was observed probably due to the A30 having a stronger binding affinity to gold than the rest of the bases. The binding of A30 bases hindered the growth of gold from depositing evenly on the surface of the nanoparticle as the nanoparticle grew thicker. Diffraction on the particle fromed by A30 on the [111] zone axis, shows multiple diffraction patterns suggesting that the roughness is due to new nucleation sites on the nanoparticle (Figure 2.7). The role of DNA in preventing the deposition of gold precursor on the seed has been previously observed as overgrowth of gold on DNA coated AuNP were found to be polycrystalline and grow through several nucleation sites on the AuNP suggesting the role of DNA in hindering the deposition of gold on the NP.[33,58]

Mechanism of growth

Quenching of the nanoparticle growth provided insight into the nanoparticle morphology at various time points. However, it is still unclear how the prism transforms into hexagon through an intermediate polyhedron shape as the quenching experiments are snapshots taken post-synthesis (Figure 2.8). [59-63] Since all of the final shape of the nanoparticles grown with G20, C30, and A30 were intermediate shapes observed during the growth of T30, we focused our analysis on the shape transformation of T30. The first question to address is the seed orientation on the nonagon and hexagon intermediates. Upon careful analysis, the nonagon shape intermediates observed at 2 min time point had an average angle of 140° (Figure 2.8b) while the hexagons formed at 5 min were found to have alternating three angles larger than the other three angles. This suggests that the original sides of the prism has grown and are no longer present in the hexagonal shape.[59] We further confirm the relative position of the prism seed by comparing the lattice directions on the hexagon nanoparticle. High magnification TEM of the hexagon nanoparticle grown at 5 min was carried out to observe the lattice on the nanoparticles. The d-spacing observed corresponds well with the $\frac{1}{3}(\bar{4}22)$ planes which meant that the lattice patterns are perpendicular to the $[\bar{2}11]$ direction parallel to $[10\bar{1}]$ direction. Since the edge of the prism was aligned with the $[10\bar{1}]$ direction of the lattice, the lattice direction observed on the hexagon particle would be parallel to the edges of the seed. The prism seed vertices were aligned with three of the vertices on the hexagon (Figure 2.8e).

Upon identifying the orientation of the seed, the growth profile from prism into the six-pointed star was identified. The growth from prisms occurred from the sides outwards in the direction of $[11\bar{2}]$, $[1\bar{2}1]$ and $[\bar{2}11]$ forming 9 sided intermediates where 3 sides were from the original prism and 6 new sides were formed. The planes on the side of the particle were difficult to identify due to the complications in obtaining the diffraction from the side for a thin plate and

determining the angle of the side plane, hence we describe the particle growth based on the changes on the direction of the edges. The original sides parallel to $[10\bar{1}]$, $[\bar{1}10]$ and $[0\bar{1}1]$ sides gradually disappeared, forming hexagons whose sides were aligned with the $\langle 11\bar{2}\rangle$ direction. The final morphology was a result of the six corners growing outwards preferentially more than the sides giving a six-pointed star which the edges are closely aligned to the $\langle 10\bar{1}\rangle$ direction.

Measurements of the length from the center of the nanoparticle to the corners and sides (defined in the models in Figure 2.8a-d) were performed for resulting particles quenched at various time points and plotted in Figure 2.8f. When the shape of the nanoparticle became symmetrical after the growth into hexagons, both lengths are the same and were measured as the distance from the center to the corner (distance in blue in model Figure 2.8c and d). From the plot in Figure 2.8f, we observed that the growth of the nanoparticle initially was faster from the sides (measurement of the red line and was slower to initiate from the corners (measurement of the blue line) in the first three minutes, resulting in rounding of the nanoparticle (Figure 2.8f). The rate of growth subsequently became similar from these two representative directions after 10 min. The disparate initial growth rate is suggestive that the sides favored deposition of the gold precursor at the initial time point.

Role of DNA

Two of the biggest questions in DNA mediated synthesis are the role of DNA on the nanoparticle and the location of DNA. To ensure that growth is mainly affected by DNA, we tested the growth at various reductant concentrations.[64,65] Our results demonstrated that the DNA mediated growth is independent of reductant concentration below 2 mM (Figure 2.9). At higher concentrations of reductant the growths were inhomogenous (Figure 2.10) indicating a rapid and

diffusion limited reduction process. Reductant concentrations in our experiments were maintained at 2 mM for a slow reduction that allow DNA to control the growth.

The difference in nanoparticle growth for different DNA may be affected by 1) influence of DNA binding on reduction potential of the gold precursor, 2) ease of removal of DNA from the gold seed, 3) DNA density on the gold seed, and 4) mobility of DNA on the gold surface. In terms of DNA binding to the gold precursor, cyclic voltammetry of the gold precursor in presence of the 4 different DNA sequence show no significant change in the reduction potential peak but the presence of DNA would influence the diffusion of the gold ion to the gold electrode surface (Figure 2.11). To address the other 3 possible interactions, we investigated the role of DNA in terms of binding affinity, concentration and mobility.

Based on our observations in the morphological evolution of the nanoparticle, the binding affinity of DNA to gold is highly related to the growth of the nanoparticle in controlling the final morphology. The stronger binding bases appeared to restrict the growth on the sides giving round particles while the weak binding bases were unable to hinder the growth on the sides. To investigate that the binding of DNA on the grown nanoparticle indeed is the factor that shape the growth, we quantified the number of DNA on synthesized nanoparticle. Using the growth from A30 and T30 as models to represent the growth with the strongest and weakest binding DNA, fluorophore labeled A30 and T30 were used in the particle growth (Figure 2.12). Upon removal of excess DNA and etching of the AuNP, the number of DNA on each particle after growth was determined from fluorescence measurements (Figure 2.13) to be approximately 240 ± 50 for A30 while it is about 23 ± 2 strands when grown with T30. Note that the number of T30 DNA on nanoparticle is about 10 times less than A30. This is consistent with the stronger binding affinity of A30 as compared to T30.[56,57] This results were consistent with the zeta potential measurement

of the nanoparticle as the zeta potential (initially +37 ±1 mV for CTAB coated nanoprism) became more negative for particles grown with A30 (-36 ± 1 mV) than that for particles grown with T30 (-19 ± 2 mV). A higher amount of DNA was bound to the final nanoparticle for A than T which suggested that the binding is important in tuning the final shape.

Since the DNA plays an important surface passivation role, the change in concentration of the DNA should affect the growth. Using growth with T30 as our model system, we investigated the growth at a range of DNA and gold precursor concentrations. The shapes of the nanoparticles thus formed were plotted as a phase diagram in Figure 2.14a. The concentration of gold precursor was varied between 0.16 mM to 1.6 mM, while the concentration of T30 was tuned between 1 to 40 μM. Four major shapes of nanoparticles observed after the growth were round, hexagonal, star, or irregular overgrown particles. At a low concentration of T30 and $HAuCl_4$, the final particles that formed are close to round shapes (representative SEM images shown in Figure 2.14 b1 and c1). With high T30 concentrations but low $HAuCl_4$, the resulting nanoparticles were hexagonal in shape (Figure 2.14, b4 and b5). At high precursor concentration, the nanoparticles were observed to be overgrown, and losing its regularity in shape (Figure 2.14, c4 and c5). We proposed that the irregularity was possibly due to insufficient DNA ligands to direct further growth of the nanoparticle. The formation of six-pointed star shape which was the desired shape for T30, only occurred at a suitable DNA and gold concentration. In addition, a minimum amount of 0.2 mM $HAuCl_4$, a minimum of 2 μM DNA is necessary for the formation of the six-pointed star shape.

To clearly elucidate the effect of DNA concentration on the growth, we compared the dimensions of the nanoparticle based on measurements of the diameter and thickness of the nanoparticles from SEM micrographs. With increasing concentration of T30, the resulted nanoparticles were smaller in diameter and thicker (Figure 2.15a). Comparing the six pointed star

shape nanoparticles that were grown at 0.5 mM of $HAuCl_4$ with 2, 5, 10, and 15 μM of T30, the lateral dimensions decreased from 280 ± 20 nm, 260 ± 30 nm, 190 ± 10 nm, to 170 ± 5 nm. The thickness of the nanoparticle however increased from 20 ± 4 nm, 34 ± 4 nm, 36 ± 6 nm, to 49 ± 7 nm. The thickness changes were unique to change of DNA concentration as manipulating the $HAuCl_4$ concentration for growth of nanoparticles induced changes on the lateral dimension of the nanoparticle but did not affect the thickness of the nanoparticle (Figure 2.15b). The diameter of the nanoparticle increased from 158 ± 8 nm, 180 ± 20 nm, 240 ± 10 nm to 280 ± 20 nm for concentrations of $HAuCl_4$ 0.16, 0.25, 0.31and 0.51 μM respectively but the thickness of the nanoparticle remained at 19 ± 4 nm. These observations suggest DNA is unique in controlling the thickness of the nanoparticle where the higher concentration would encourage the growth in thickness and restrict lateral growth.

Both the investigations involving the parameters DNA affinity and DNA concentration in the growth arrived to a similar conclusion. The results were consistent in suggesting the binding of DNA on the sides of the nanoparticle which hinders the growth on the sides with higher binding affinity DNA and higher concentration of DNA. As a result the nanoparticle is smaller in diameter but would appear thicker or rougher.

Location of DNA

Probing the location of ligands on the surface of nanoparticles has found to be challenging. The low electron contrast of organic ligands makes the ligand difficult to be observed with nanometer scale spatial resolution. One of the advantages of DNA as a ligand is the ability to hybridize with its complementary sequence. Using the properties of DNA, we can probe the location of the DNA on the nanoparticle surface using a complementary DNA (cDNA) tag. We

used small AuNP of 5 nm functionalized with thiolated DNA (e.g. T30 (AuNP-T)) as the tag to easily observe under the electron microscope. Using the complementary strands with AuNP probes, we can detect the location of DNA on the nanoparticle grown. The T30 on the AuNP will be able to hybridize to the A30 DNA on the grown nanoparticle and the location of the AuNP would indicate the distribution of A30. Upon hybridization of the AuNP-T on rough round particles grown with A30, 5 nm AuNP-T were observed throughout the nanoparticle. However, it was notable that the AuNP-T were found mainly on the crevices of the rough features on the nanoparticle (Figure 2.16). Control experiments using AuNP with non-complementary sequences did not bind the grown nanoparticle indicating that the interaction of AuNP-T with the nanoparticle is through specific hybridization and not artifact of drying. The position of AuNP-T is reflective of the position of the DNA. The observation of A30 at the crevices of the nanoparticle is consistent with binding of A30 to the gold surface that would hinder deposition of gold. Despite our desire to observe the location of DNA on attached initially on the prism, no AuNP was found to bind the prism. This might be due to the weak attachment of the probe AuNP on the prism.

In addition to the role of the DNA binding on the AuNP, the role of excess DNA present in the growth solution was also investigated. To prove that the excess DNA would influence the growth, we pre-incubated the seeds with A30 for 30 min and removed the excess A30 from the growth system through centrifugation once. Subsequently, the prisms were resuspended in water and reduction was performed. The growth resulted in formation of smooth pointed nanoparticles, which are far from the expected growth of a round and rough A30 (Figure 2.17). This experiment indicated that other than the DNA bound to the surface of the nanoparticle, the growth is continuously affected by binding from the excess DNA. The excess DNA plays a pivotal role in simultaneously binding to the gold surfaces as the gold deposits on the nanoparticle.

Proposed mechanism of growth

Based on our studies above, we can conclude that 1) The shape transformation for prism occurs via nonagon and hexagon intermediates to finally a six-pointed star, 2) the growth of the nanoparticle occurs on the sides in the direction of first forming a nonagon intermediate, 3) the shape or diameter of the nanoparticle is achieved within 7 min followed by the change in thickness, 4) The change in shape is influenced by the binding affinity of the DNA and likely through a surface passivation mechanism 5) DNA binding hinders the deposition of gold precursor on the surface of the seed, 6) DNA binding continuously plays a role in affecting the growth.

To describe the growth mechanism, the growth is divided to 2 stages and summarize in Scheme 2.1. In the first stage of growth, the shape of the nanoparticle is defined and determined by the binding of DNA on to the nanoparticle. From Figure 2.1, we observe that the rates of growth of diameter are similar for all four bases prior to the observation of a plateau or decrease in growth rate. The growth starts to plateau or slow down at 3 min for A and C, 5 min for G and 7 min for T. At these time points the nanoparticle shape are final and the diameter of the nanoparticles do not significantly increase with time. To explain this growth phenomenon where the shape of the nanoparticle stops changing at various points depending on the DNA, a reasonable explanation is that binding of the DNA stabilizes the side facets of the nanoparticle and lowers the surface energy of the side facet. However, based on solely a surface energy argument, it is unlikely for DNA binding to completely hinder the growth on the sides. The observation of a sudden stop in growth of {100} over other facets was observed recently in the growth of platinum nanocubes using in-situ TEM. The authors identified that arresting of the {100} growth is due to the low ligand mobility o the {100} facet resulting in a kinetically controlled growth rather than thermodynamic

growth.[66] Therefore, the possible explanation for the observed growth is that the DNA bound on the sides of the particle is kinetically trapped thereby hindering deposition of additional gold atoms. In kinetically controlled growth, other than the mobility, desorption of the ligand from the surface and the packing density of the ligand would also play a role. The binding of ligands on gold is a reversible process with the equilibrium dependent on the binding affinity and concentration of the ligand.[67] The binding affinity of the DNA affects the ability of the DNA to desorb from the surface and the density of the ligand on the particle. The higher binding affinity results in the DNA being more difficult to remove from the surface and the higher binding DNA also have a higher number of DNA bound per particle, these two effect combined results in difficulties for the DNA to make room for gold deposition. Therefore the higher binding affinity base, A and C, could kinetically trap the shape of the nanoparticle at a nonagon shape at the early stage while the weaker binding affinity base, G and T could only trap the shape at a later stage of the growth. The mobility of the DNA may be a factor as well but the mobility of DNA bases on the side surface is currently difficult to characterize. Due to the complexity of DNA and the side facet, we have yet to determine the mobility of the DNA on the surface of the nanoparticle. But we expect the mobility to change with the DNA sequence.

At the second stage of growth, the thickness of the nanoparticle varies and grows at different rates. The thicknesses of the nanoparticles were similar in the initial 7 min but the rates starts to vary with different bases thereafter. At 7 min, the lateral growths for all four bases were mostly completed. The growth on the thickness is dependent on the remaining gold amount in the solution which is inversely related to the diameter of the nanoparticle. The thickness did not change much for T after 7 min as the gold source have been depleted but G, C and A continues to grow and the rate varies. The growth rate for G is lower which might be related to the lower amount of

gold remaining in solution. The gold amount remaining for A and C is rather similar but the rates are different and the surface morphology is different. We propose that this growth would depend on the mobility of the DNA bases on the Au {111} surface. The mobility of A base on the Au{111} surface was reported to be lower than the mobility of C base on Au{111}. This low mobility for A drives the deposition of gold on locations where the DNA is not bound resulting in formation of rough growth surface. On the other hand, despite the high biding affinity, the higher mobility of C base on Au{111} permits a smooth deposition on the Au{111} surface.

Rather than a thermodynamically determined growth which is expected through a surface passivation mechanism, the DNA kinetically controls the deposition of gold based on the binding affinity of DNA, the DNA density and the DNA mobility on the gold surface. This mechanism can also be used to explain the observation of a thicker nanoparticle formed with higher concentration of DNA for T30. As the edges of the gold nanoparticle are better blocked by the higher concentration of T30, the surface of the prism is forced to grow resulting in the formation of a thicker nanoparticle.

Extension of the mechanism into other systems: Combination of bases

We further extend the mechanistic understanding of nanoparticle synthesis with homo-oligomers to understand the programmability of DNA to tune the structures based on combinations of sequences.[8] While A30 forms rough and round plates and G20 forms hexagonal plates, a combination of G15A15 results in nanoparticles that are hexagonal and rough. A kinetic investigation on the growth of nanoparticle influenced by G15A15 was performed (Figure 2.18a). The shape transformation is similar to the kinetics study of with other bases where the prism grew into round polyhedron then hexagon, and finally the roughness developed on the surface of the

nanoparticle. As compared to the growth with G20, the growth into hexagon shape for G20 was only 3 -5 min but with G15A15, the time was slightly slower at 5-7 min. This increase in growth time is reflective of the increase in binding affinity of G15A15 to gold as compared to the G20 sequence. The increase in binding affinity more effectively bound to the edge and resulted in slower growth to form the hexagonal shape. The roughness of the particle begins to develop at 15 min, similar to when the roughness begin to develop in A30. The presence of A15 in G15A15 provides the DNA with a low mobility on the surface of the nanoparticle and result in a rough deposition of gold. The location and position of G15A15 on the nanoparticle was probed with AuNP-C and AuNP-T which can hybridize to G and A respectively (shown in Figure 2.18b and c). AuNP-C hybridized at the rough features of the nanoparticle while no attachment of AuNP-T was observed. This result suggest that the A15 region of the G15A15 sequence forms a localized strong binding to the surface of the gold which results in blocking of the growth and formation of a rough surface. The G15 end of the G15A15 sequence does not bind as strongly as A15 on the nanoparticle surface and could hybridize with AuNP-C. When two kinds of bases are combined the effects from both bases are observed where the binding affinity was tuned by the combination of bases and influencing the shape. The effect of localized segments of sequence with low mobility could still be observed in block combinations of bases. Future work focuses on investigating the sequence combination of the bases with the same ratio but different sequence alignment to investigate the effect of having alternating bases or block segments of bases.

Extension of the mechanism into other systems: cube and octahedron seeds

Upon understanding the mechanism of the DNA mediated growth system on gold nanoprisms, we were interested in knowing if a similar mechanism would be observed with seeds

of other shapes and initial facets. To study the effect of particle seed, we extended the growth to two other seed systems: gold nanocubes and gold nanooctahedron which have {100} and {111} facets respectively.

With gold nanocubes as seeds, in the presence of T which is the low binding affinity DNA, the nanoparticles grew on all 8 corners of the nanoparticle forming a truncated stellated octahedron. The (110) faces grew slower than the (100) or the (111) faces hence resulting in the formation of grooves on the particle. On the other hand, the nanocubes grown with A resulted in a rough cubic particle (Figure 2.19a). With gold nanooctahedons as seeds, our experiment results show that the nanoparticles grew with T grew on the corners of the octahedron forming a longer tips while nanoparticles grown with A formed rough structures on the surface (Figure 2.19b).

These two results are still at their preliminary stages hence it is difficult to relate the growth mechanism with the one on gold nanoprisms. The results however shows a more restrained growth with A than with T as observed from the formation of a smaller and rough particle. Further kinetic studies of the growths are required to further understand the mechanism and relate the grow mechanisms with different seed shapes and understand possible roles of facet related growth. More in-depth understanding of the DNA interaction with different facets would be required to fully understand the mechanism. None the less, these results show great promise in the ability to tune nanoparticle growth not only for one shape of seeds but extended to other seed shapes as well.

Extension of the DNA mediated growth to bimetallic nanoparticles

Core-shell NPs consisting of different materials are of great interest as the NPs may adopt properties from both materials. Therefore, bimetallic NPs could have synergistic properties that are different from the individual materials for potential catalytic, photonic, and electronic

applications.[68-71] In the conventional synthesis of core-shell NPs, the shell adopts the shape of the initial NP and is difficult to tune to different shapes with the same starting core.[72,73] The use of DNA as capping agent may allow us to tune the shape of the shell to differ from the seed's shape. Our initial study was to investigate the growth Au-Ag bimetallic nanomaterials using Au nanoprisms as seeds. As shown in Figure 2.20a, different DNA bases resulted in different morphologies of Au-Ag nanomaterials. While A30 and G20 formed structures like hexagonal rods, T30 particles were irregular and C30 formed hexagonal plates. The bimetallic components were imaged in the high-angle annular dark-field (HAADF) mode exhibiting good Z-contrast between the Au seed and the Ag surface. In addition, the identity of the metal was confirmed using energy-dispersive spectroscopy (EDS) and the position of the seed was confirmed with EDS elemental mapping of the bimetallic particle (Figure 2.20b). The diffraction patterns on the hexagonal nanorod like bimetallic particle shows the formation of twinned {110} facets on the sides while {111} facets were still retained on the surface (Figure 2.21). Since the binding affinity of DNA to silver and gold is different,[74] it is not surprising that the growth for silver to be different from the deposition of gold. The growth with silver with A and G results in more growth on the surface to increase the thickness of the nanoparticle with little change in the diameter, while the growth for C30 forms particle with larger diameter and smaller thickness. The result shows preliminary data for DNA mediated growth to tune the formation of bimetallic silver shell gold core nanoparticle.

2.3 Conclusions

We report the mechanistic study of DNA mediated nanoparticle growth. This in depth study is the first of its kind for ligands with fine-tuned binding affinities. The shape transformation of the nanoparticle, the role of DNA and the location of DNA were investigated. The

morphological evolution were observed and correlated with the plasmonic features of the nanoparticle. The growth of nanoprisms using T30 occurs through intermediates of round polyhedron, hexagon and finally forming six-point stars. Contrary to typical knowledge in ligand stabilized growth of nanoparticle where the ligand lowers the surface energy a specific facet, DNA manipulates the growth of nanoparticle by surface passivation and kinetically hindering the deposition of gold. This kinetic control is influenced by the ability of DNA to desorb, DNA density and DNA mobility. The ability of DNA to desorb from the gold surface is related to the binding affinity of the DNA bases to gold while the DNA density would depend on the binding affinity of the DNA base and concentration of DNA. Our studies show a strong correlation of the binding affinity of the DNA bases towards gold in the order of A> C> G> T in affecting the final shape of the resulting nanoparticle. The overgrowth of nanoparticle is also affected by the concentration of DNA, as a result thicker and smaller diameter nanoparticles are obtained with increasing DNA concentration. The effect from mobility of DNA is observed for A and C where both have high binding affinity to gold but C has higher mobility on gold {111} surface as compared to A. The nanoparticle form by C is smooth while the low mobility of A forces uneven gold deposition.

The mechanism for the growth of the nanoprisms by DNA is proposed to occur via two stages, shape control and growth of the thickness. Having identified the origin for such fine control offered by DNA, we believe this elucidation is important to aid in developing methods that would allow fine control over the nanoparticle shape. In addition, this mechanism can be expanded DNA mediated growth of other seed systems and code for formation of a variety of shapes in a more predictable manner.

2.4 Experimental Section

Materials and Methods

Materials. All oligodeoxyribonucleotides were purchased from Integrated DNA Technologies (Coralville, IA). Hydrogen tetrachloroaurate (III) hydrate, hydroxylamine hydrochloride, sodium hydroxide, cetyltrimethlyammonium bromide (≥99%), sodium iodide, L-ascorbic acid and sodium borohydride were purchased from Sigma-Aldrich.

Synthesis and purification of gold nanoprisms. Gold nanoprisms were prepared by following previously published procedures. The as-prepared nanoprism solution was stored in a glass flask overnight to allow the nanoprisms to settle. Afterwards, the supernatant was removed and the gold nanoprisms were redispersed in Millipore water (6-7 mL).

Synthesis of the gold nanoparticles mediated by DNA. The freshly redispersed gold nanoprism solution was purified by centrifugation twice. Its absorbance at 800 nm was then measured by UV-vis spectrometry, and adjusted to 0.7 with appropriate dilutions. 100 µL of this solution was incubated with 2 µM of DNA for 15 min to allow the DNA to adsorb onto the gold nanoseeds. 1 µL of 200 mM NH_2OH (adjusted to pH 5 with NaOH) was then added and the solution was vortexed. 2.5 µL 0.8 % (w/v) $HAuCl_4$ was then introduced to initiate the reduction reaction. A color change was observed in a few minutes, and the reaction was allowed to progress at least 30 minutes. For the phase plot to investigate DNA and gold concentration dependence, the DNA amount added was varied and the concentration of the HAuCl4 solutions were varied.

Kinetic monitoring by quenching of growth. 5 µL of 100 mM mercaptopropionic acid was added to the growth solution at designated time points. The solution was then added with 10 µL 0.2% sodium dodecylsulfate (SDS) before centrifuge to purify the nanoparticles prior to imaging in SEM or TEM.

Cyclic voltammetry was performed on CH Instrument model 620A Electrochemical Analyzer (Austin, TX) at a scan rate of 10 mV/s versus an Ag/AgCl reference electrode. A gold electrode was used as the working electrode and a platinum wire was used as auxiliary electrode. Cyclic scans were performed in the range of 1.2 V to -0.2 V. Gold chloride (0.5 mM) was bubbled with argon gas for 10 min prior to scanning. To test the influence of DNA, cyclic voltammetry measurements were performed on a solution of 0.5 mM gold chloride with an additional 4 μM of DNA.

DNA quantification experiments were performed by replacing fluorescein-labeled DNA with unlabeled DNA for the nanoparticle growth. The particles grown were centrifuged 6 times for 2 minutes each at 5900 rcf in order to remove excess DNA. The nanoparticles were etched using 5 μL of 100 mM KCN. The concentration of DNA was measured through fluorescence measurements. The number of DNA on each particle was the number of DNA attached to the particle after growth divided by the number of particles. The concentration of particles was determined to be approximately 1 nM for absorbance of 0.7 at wavelength 800 nm, as determined using ICP-MS.

Equipment and Characterizations. The particles synthesized as well as the nano-assemblies formed were analyzed using JEOL 2010LaB6/ 2100cryo transmission electron microscope (TEM) operated at 200 kV or Hitachi S4800 SEM with 10 kV and 10 μA. Nanoparticle concentrations were characterized by the absorbance at 800 nm using UV-Vis spectrophotometry (Hewlett–Packard 8453).

2.5 References

(1) Naik, R. R.; Stringer, S. J.; Agarwal, G.; Jones, S. E.; Stone, M. O. *Nat. Mater.* **2002**, *1*, 169.

(2) Kriplani, U.; Kay, B. K. *Curr. Opin. Biotechnol.* **2005**, *16*, 470.

(3) Berti, L.; Burley, G. A. *Nat. Nanotechnol.* **2008**, *3*, 81.

(4) Chiu, C.-Y.; Li, Y.; Ruan, L.; Ye, X.; Murray, C. B.; Huang, Y. *Nat. Chem.* **2011**, *3*, 393.

(5) Oh, J.-W.; Lim, D.-K.; Kim, G.-H.; Suh, Y. D.; Nam, J.-M. *J. Am. Chem. Soc.* **2014**, *136*, 14052.

(6) Erdmann, M.; David, R.; Fornof, A. R.; Gaub, H. E. *Nat. Chem.* **2010**, *2*, 745.

(7) Wang, Z.; Zhang, J.; Ekman, J. M.; Kenis, P. J. A.; Lu, Y. *Nano Lett.* **2010**, *10*, 1886.

(8) Wang, Z.; Tang, L.; Tan, L. H.; Li, J.; Lu, Y. *Angew. Chem. Int. Ed.* **2012**, *51*, 9078.

(9) Richards, C. I.; Choi, S.; Hsiang, J.-C.; Antoku, Y.; Vosch, T.; Bongiorno, A.; Tzeng, Y.-L.; Dickson, R. M. *J. Am. Chem. Soc.* **2008**, *130*, 5038.

(10) Choi, S.; Dickson, R. M.; Yu, J. *Chem Soc Rev* **2012**, *41*, 1867.

(11) Hinds, S.; Taft, B. J.; Levina, L.; Sukhovatkin, V.; Dooley, C. J.; Roy, M. D.; MacNeil, D. D.; Sargent, E. H.; Kelley, S. O. *J. Am. Chem. Soc.* **2005**, *128*, 64.

(12) Tikhomirov, G.; Hoogland, S.; Lee, P. E.; Fischer, A.; Sargent, E. H.; Kelley, S. O. *Nat. Nanotechnol.* **2011**, *6*, 485.

(13) Cha, T.-G.; Baker, B. A.; Salgado, J.; Bates, C. J.; Chen, K. H.; Chang, A. C.; Akatay, M. C.; Han, J.-H.; Strano, M. S.; Choi, J. H. *ACS Nano* **2012**, *6*, 8136.

(14) Chen, Y.-C.; Wen, C.-C.; Liau, I.; Hsieh, Y.-Z.; Hsu, H.-Y. *J. Mater. Chem. B* **2014**, *2*, 4100.

(15) Wu, J.; Tan, L. H.; Hwang, K.; Xing, H.; Wu, P.; Li, W.; Lu, Y. *J. Am. Chem. Soc.* **2014**, *136*, 15195.

(16) Scholl, J. A.; Koh, A. L.; Dionne, J. A. *Nature* **2012**, *483*, 421.

(17) Murphy, C. J.; Sau, T. K.; Gole, A. M.; Orendorff, C. J.; Gao, J.; Gou, L.; Hunyadi, S. E.; Li, T. *J. Phys. Chem. B* **2005**, *109*, 13857.

(18) Tan, S. J.; Campolongo, M. J.; Luo, D.; Cheng, W. *Nat. Nanotechnol.* **2011**, *6*, 268.

(19) Guerrero-Martínez, A.; Alonso-Gómez, J. L.; Auguié, B.; Cid, M. M.; Liz-Marzán, L. M. *Nano Today* **2011**, *6*, 381.

(20) Kuzyk, A.; Schreiber, R.; Fan, Z.; Pardatscher, G.; Roller, E.-M.; Hogele, A.; Simmel, F. C.; Govorov, A. O.; Liedl, T. *Nature* **2012**, *483*, 311.

(21) Yan, W.; Xu, L.; Xu, C.; Ma, W.; Kuang, H.; Wang, L.; Kotov, N. A. *J. Am. Chem. Soc.* **2012**, *134*, 15114.

(22) Mastroianni, A. J.; Claridge, S. A.; Alivisatos, A. P. *J. Am. Chem. Soc.* **2009**, *131*, 8455.

(23) Macfarlane, R. J.; Lee, B.; Jones, M. R.; Harris, N.; Schatz, G. C.; Mirkin, C. A. *Science* **2011**, *334*, 204.

(24) Nykypanchuk, D.; Maye, M. M.; van der Lelie, D.; Gang, O. *Nature* **2008**, *451*, 549.

(25) Park, S. Y.; Lytton-Jean, A. K. R.; Lee, B.; Weigand, S.; Schatz, G. C.; Mirkin, C. A. *Nature* **2008**, *451*, 553.

(26) Hu, M.; Chen, J.; Li, Z.-Y.; Au, L.; Hartland, G. V.; Li, X.; Marquez, M.; Xia, Y. *Chem Soc Rev* **2006**, *35*, 1084.

(27) Lal, S.; Clare, S. E.; Halas, N. J. *Acc. Chem. Res.* **2008**, *41*, 1842.

(28) Huang, X.; Neretina, S.; El-Sayed, M. A. *Adv. Mater.* **2009**, *21*, 4880.

(29) Anker, J. N.; Hall, W. P.; Lyandres, O.; Shah, N. C.; Zhao, J.; Van Duyne, R. P. *Nat Mater* **2008**, *7*, 442.

(30) Murphy, C. J.; Gole, A. M.; Stone, J. W.; Sisco, P. N.; Alkilany, A. M.; Goldsmith, E. C.; Baxter, S. C. *Acc. Chem. Res.* **2008**, *41*, 1721.

(31) Wu, P.; Hwang, K.; Lan, T.; Lu, Y. *J. Am. Chem. Soc.* **2013**, *135*, 5254.

(32) Xiang, Y.; Wu, P.; Tan, L.; Lu, Y. In *Biosensors Based on Aptamers and Enzymes*; Gu, M. B., Kim, H.-S., Eds.; Springer Berlin Heidelberg: 2014; Vol. 140, p 93.

(33) Lim, D.-K.; Jeon, K.-S.; Hwang, J.-H.; Kim, H.; Kwon, S.; Suh, Y. D.; Nam, J.-M. *Nat. Nanotechnol.* **2011**, *6*, 452.

(34) Haruta, M. *Catal. Today* **1997**, *36*, 153.

(35) Corma, A.; Serna, P. *Science* **2006**, *313*, 332.

(36) Lopez-Sanchez, J. A.; Dimitratos, N.; Hammond, C.; Brett, G. L.; Kesavan, L.; White, S.; Miedziak, P.; Tiruvalam, R.; Jenkins, R. L.; Carley, A. F.; Knight, D.; Kiely, C. J.; Hutchings, G. J. *Nat. Chem.* **2011**, *3*, 551.

(37) Zhong, R.-Y.; Sun, K.-Q.; Hong, Y.-C.; Xu, B.-Q. *ACS Catal.* **2014**, 3982.

(38) Grzelczak, M.; Perez-Juste, J.; Mulvaney, P.; Liz-Marzan, L. M. *Chem. Soc. Rev.* **2008**, *37*, 1783.

(39) Tao, A. R.; Habas, S.; Yang, P. *Small* **2008**, *4*, 310.

(40) Mourdikoudis, S.; Liz-Marzán, L. M. *Chem. Mater.* **2013**, *25*, 1465.

(41) Zhao, P.; Li, N.; Astruc, D. *Coord. Chem. Rev.* **2013**, *257*, 638.

(42) Turkevich, J.; Stevenson, P. C.; Hillier, J. *Discuss. Faraday Soc.* **1951**, *11*, 55.

(43) Ji, X.; Song, X.; Li, J.; Bai, Y.; Yang, W.; Peng, X. *J. Am. Chem. Soc.* **2007**, *129*, 13939.

(44) Personick, M. L.; Langille, M. R.; Zhang, J.; Mirkin, C. A. *Nano Lett.* **2011**, *11*, 3394.

(45) Jana, N. R.; Gearheart, L.; Murphy, C. J. *J. Phys. Chem. B* **2001**, *105*, 4065.

(46) Nikoobakht, B.; El-Sayed, M. A. *Chem. Mater.* **2003**, *15*, 1957.

(47) Seo, D.; Park, J. C.; Song, H. *J. Am. Chem. Soc.* **2006**, *128*, 14863.

(48) Jackson, A. M.; Myerson, J. W.; Stellacci, F. *Nat. Mater.* **2004**, *3*, 330.

(49) Liu, X.; Yu, M.; Kim, H.; Mameli, M.; Stellacci, F. *Nat. Commun.* **2012**, *3*, 1182.

(50) Piana, S.; Bilic, A. *J. Phys. Chem. B* **2006**, *110*, 23467.

(51) Langille, M. R.; Personick, M. L.; Zhang, J.; Mirkin, C. A. *J. Am. Chem. Soc.* **2012**, *134*, 14542.

(52) Lee, K.-S.; El-Sayed, M. A. *J. Phys. Chem. B* **2006**, *110*, 19220.

(53) Jain, P. K.; Lee, K. S.; El-Sayed, I. H.; El-Sayed, M. A. *J. Phys. Chem. B* **2006**, *110*, 7238.

(54) Sardar, R.; Funston, A. M.; Mulvaney, P.; Murray, R. W. *Langmuir* **2009**, *25*, 13840.

(55) Jin, R.; Charles Cao, Y.; Hao, E.; Metraux, G. S.; Schatz, G. C.; Mirkin, C. A. *Nature* **2003**, *425*, 487.

(56) Kimura-Suda, H.; Petrovykh, D. Y.; Tarlov, M. J.; Whitman, L. J. *J. Am. Chem. Soc.* **2003**, *125*, 9014.

(57) Demers, L. M.; Östblom, M.; Zhang, H.; Jang, N.-H.; Liedberg, B.; Mirkin, C. A. *J. Am. Chem. Soc.* **2002**, *124*, 11248.

(58) Shen, J.; Xu, L.; Wang, C.; Pei, H.; Tai, R.; Song, S.; Huang, Q.; Fan, C.; Chen, G. *Angew. Chem. Int. Ed.* **2014**, *53*, 8338.

(59) Goebl, J.; Zhang, Q.; He, L.; Yin, Y. *Angew. Chem. Int. Ed.* **2012**, *51*, 552.

(60) Lofton, C.; Sigmund, W. *Adv. Funct. Mater.* **2005**, *15*, 1197.

(61) An, J.; Tang, B.; Ning, X.; Zhou, J.; Zhao, B.; Xu, W.; Corredor, C.; Lombardi, J. R. *J. Phys. Chem. C* **2007**, *111*, 18055.

(62) Langille, M. R.; Personick, M. L.; Mirkin, C. A. *Angew. Chem. Int. Ed.* **2013**, *52*, 13910.

(63) Hong, S.; Shuford, K. L.; Park, S. *Chem. Mater.* **2011**, *23*, 2011.

(64) Lohse, S. E.; Murphy, C. J. *Chem. Mater.* **2013**, *25*, 1250.

(65) Straney, P. J.; Marbella, L. E.; Andolina, C. M.; Nuhfer, N. T.; Millstone, J. E. *J. Am. Chem. Soc.* **2014**, *136*, 7873.

(66) Liao, H.-G.; Zherebetskyy, D.; Xin, H.; Czarnik, C.; Ercius, P.; Elmlund, H.; Pan, M.; Wang, L.-W.; Zheng, H. *Science* **2014**, *345*, 916.

(67) Wang, Y.; He, J.; Liu, C.; Chong, W. H.; Chen, H. *Angew. Chem. Int. Ed.* **2014**, DOI: 10.1002/anie.201402986.

(68) Yang, Y.; Liu, X.; Li, X. B.; Zhao, J.; Bai, S. Y.; Liu, J.; Yang, Q. H. *Angew. Chem. Int. Ed.* **2012**, *51*, 9164.

(69) Oezaslan, M.; Heggen, M.; Strasser, P. *J. Am. Chem. Soc.* **2012**, *134*, 514.

(70) Prado, Y.; Dia, N.; Lisnard, L.; Rogez, G.; Brisset, F.; Catala, L.; Mallah, T. *Chem. Commun.* **2012**, *48*, 11455.

(71) Liu, J.; Qiao, S. Z.; Hu, Q. H.; Lu, G. Q. *Small* **2011**, *7*, 425.

(72) Xia, Y. N.; Xiong, Y. J.; Lim, B.; Skrabalak, S. E. *Angew. Chem. Int. Ed.* **2009**, *48*, 60.

(73) Gu, J.; Zhang, Y. W.; Tao, F. *Chem. Soc. Rev.* **2012**, *41*, 8050.

(74) Basu, S.; Jana, S.; Pande, S.; Pal, T. *J. Colloid Interface Sci.* **2008**, *321*, 288.

2.6 Figures

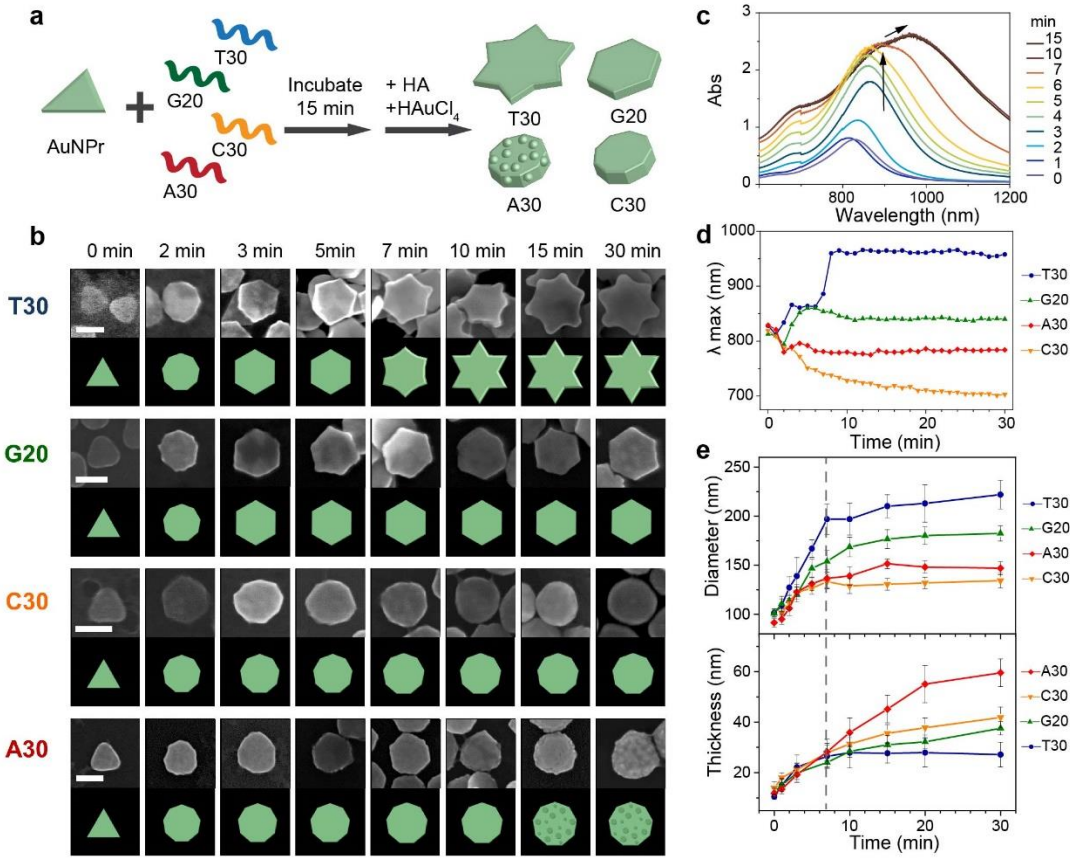

Figure 2.1. (a) Seed mediated method used in DNA encoded the growth of AuNPr seed into four shapes using the four different DNA stands T30, G20, C30, and A30. (b) Enlarged SEM images showing representative images of the morphological evolution of AuNPr prepared with T30, G20, C30, and A30 from 0 -30 min with its corresponding schematic image. Scale bars are 100 nm. (c) Kinetic UV-vis spectra of the AuNPr growth solution in the presence of T30 with time. (d) Change in the λ_{max} with time from kinetic UV-vis spectra for growth solutions with T30, G20, A30 and C30. (e) Measured dimensions of the nanoparticle growth at various time points with T30, G20, A30 and C30 for diameter and thickness.

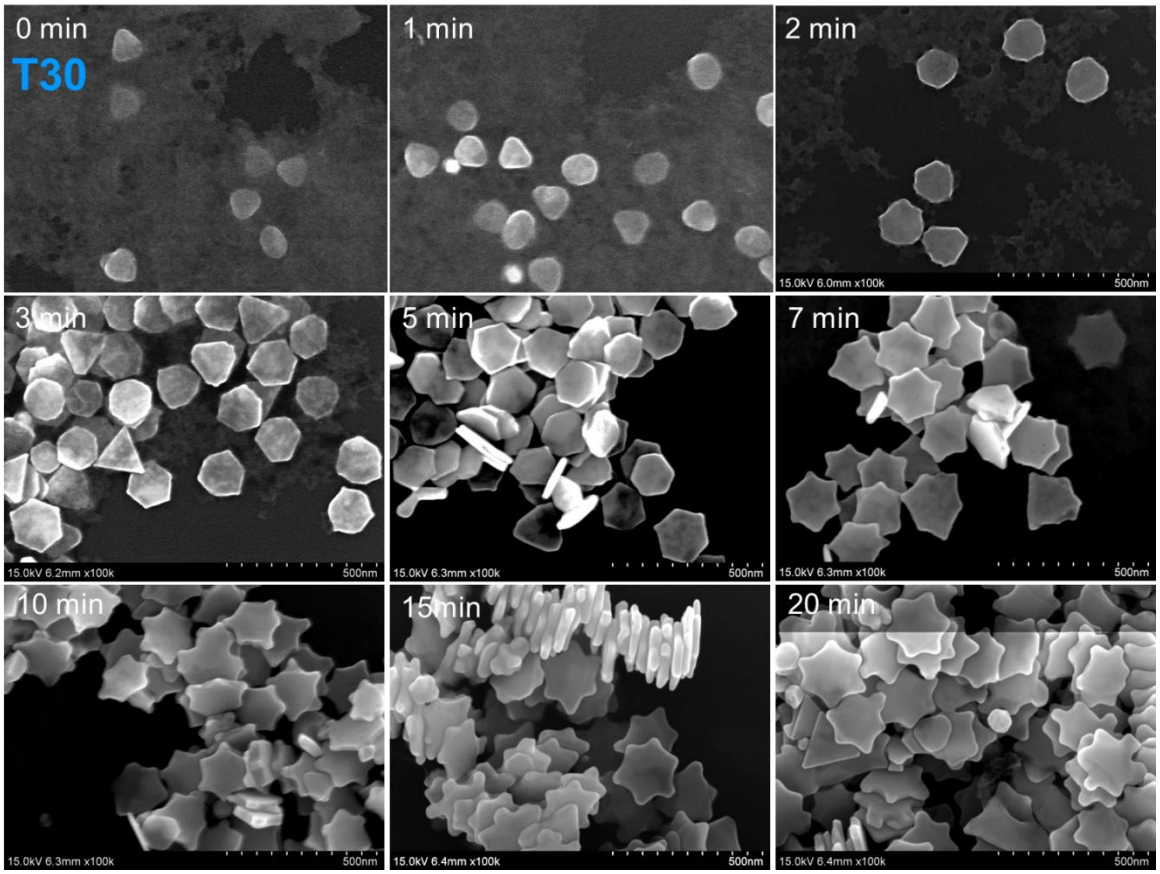

Figure 2.2. SEM images of AuNPr grown with T30 quenched at various time points of 0-20 mins. Scale bars are the same for all SEM images with scale of 500 nm.

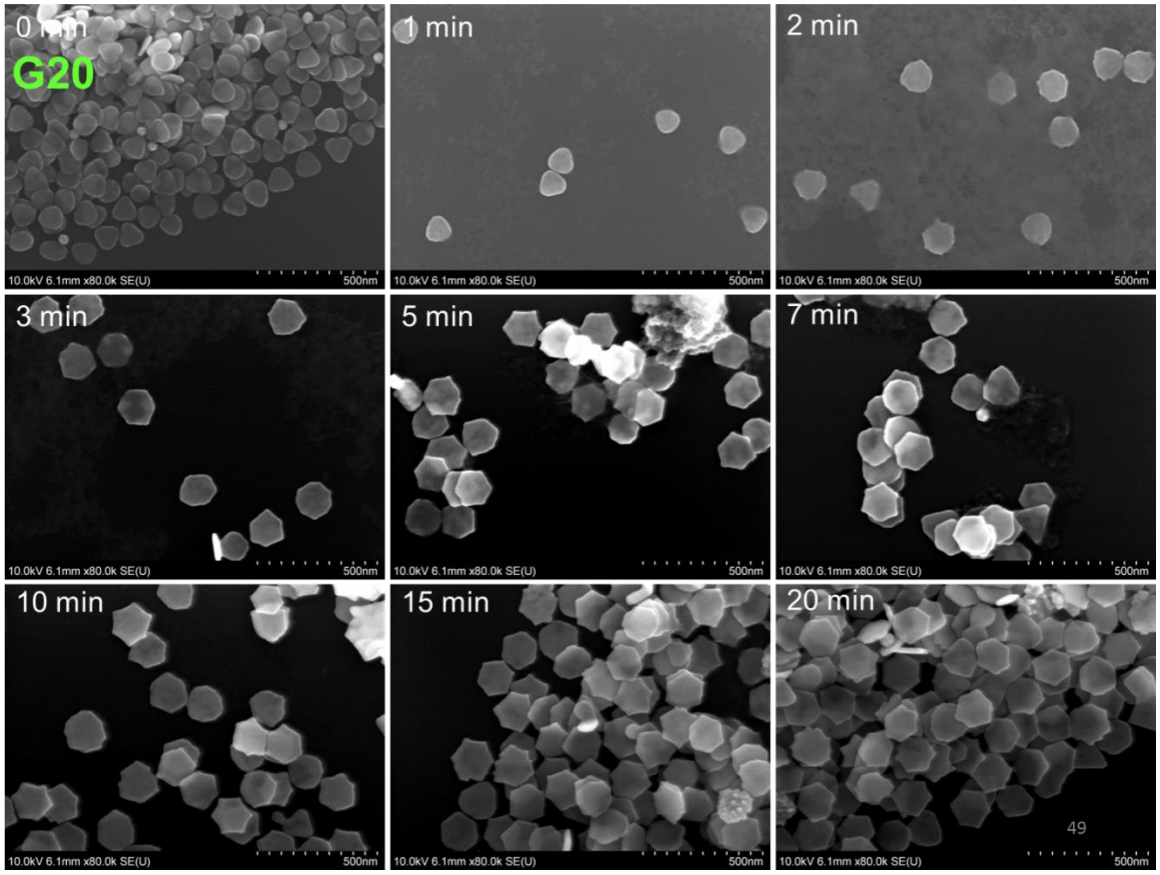

Figure 2.3. SEM images of AuNPr grown with G20 quenched at various time points of 0-20 mins. Scale bars are the same for all SEM images with scale of 500 nm.

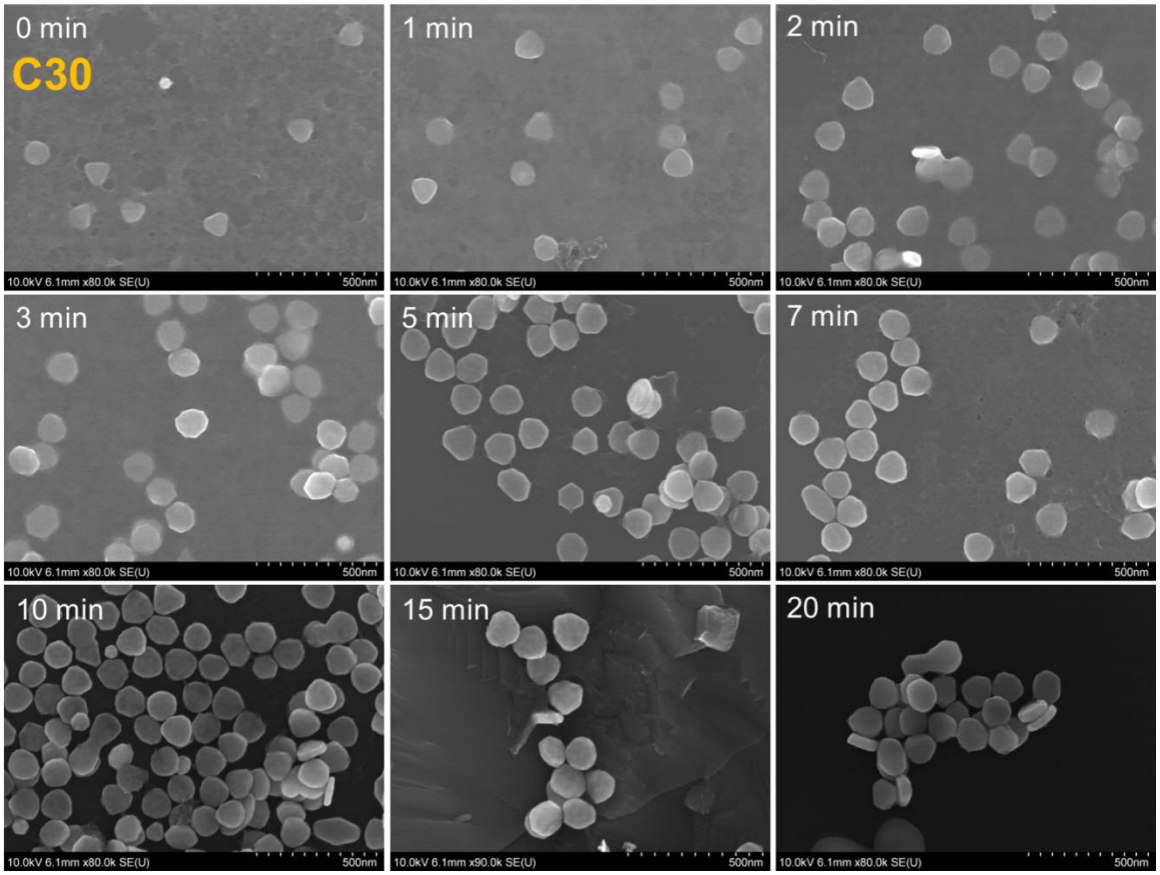

Figure 2.4. SEM images of AuNPr grown with C30 quenched at various time points of 0-20 mins. Scale bars are the same for all SEM images with scale of 500 nm.

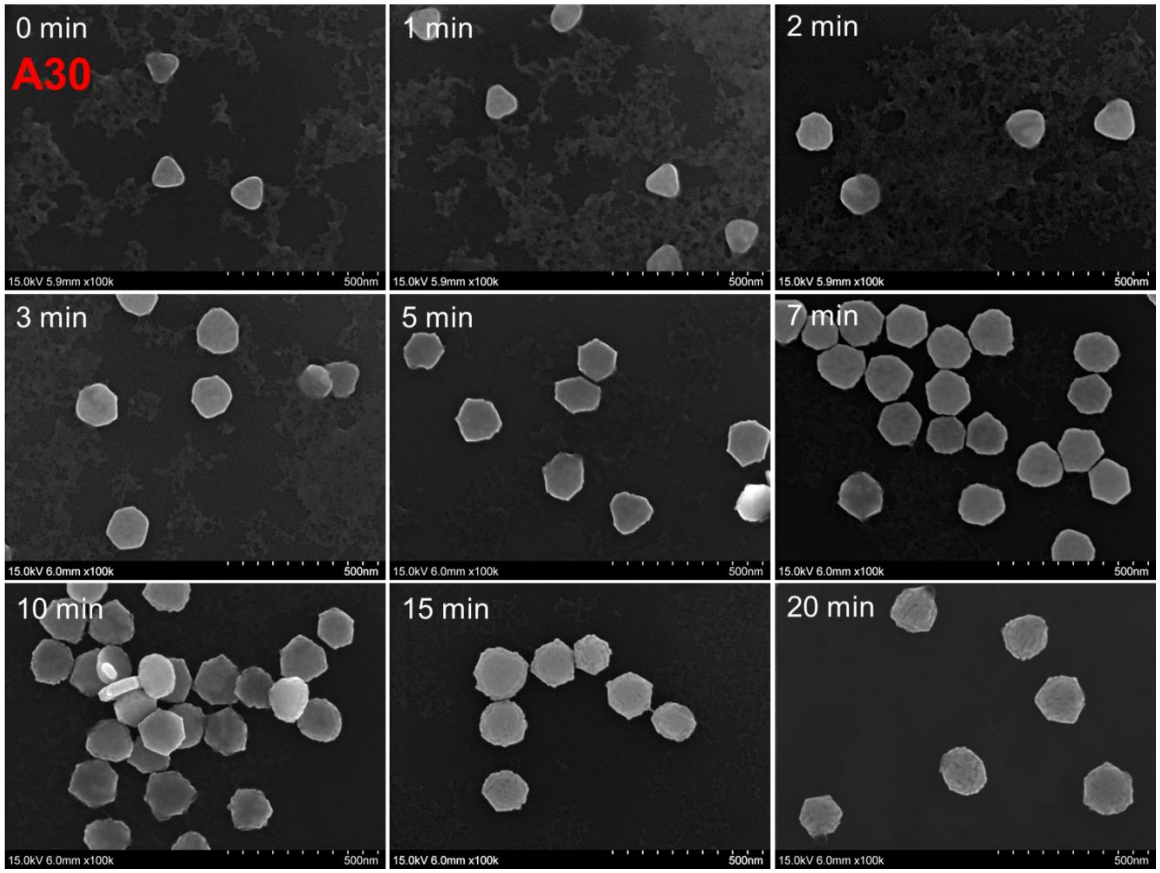

Figure 2.5. SEM images of AuNPr grown with A30 quenched at various time points of 0-20 mins. Scale bars are the same for all SEM images with scale of 500 nm.

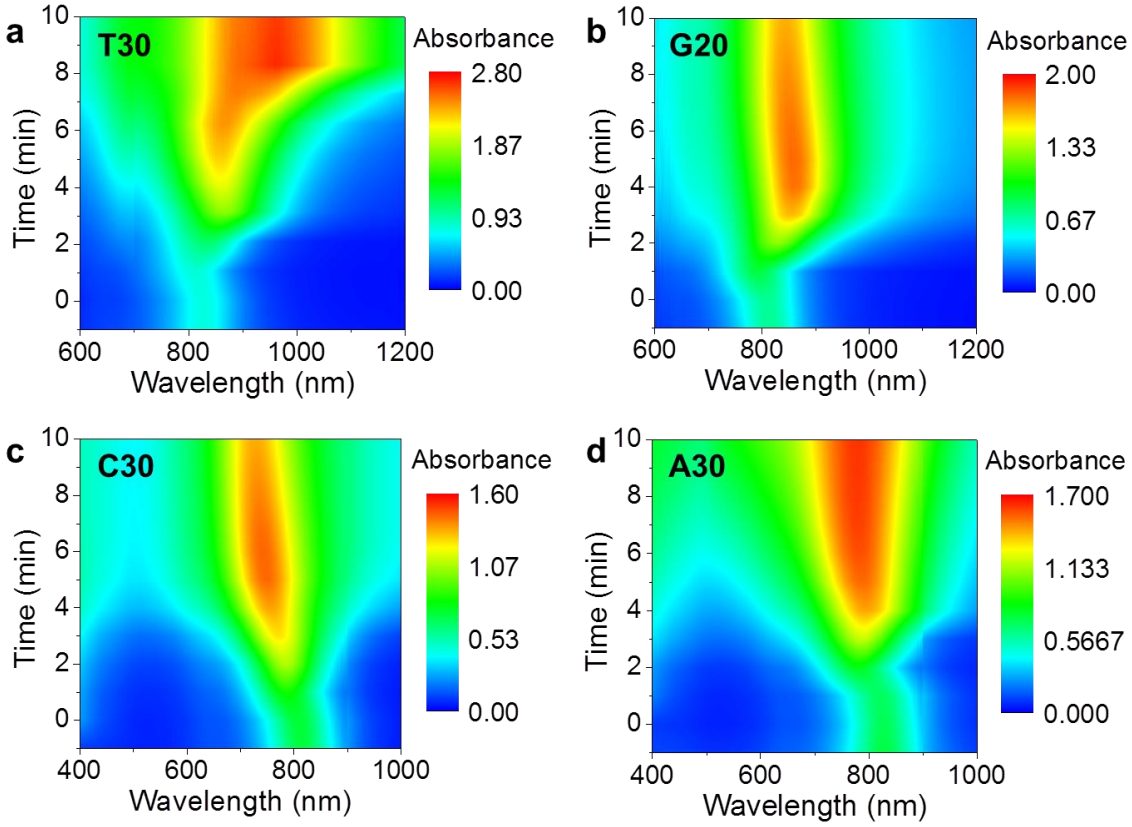

Figure 2.6. Contour plot of UV-vis absorbance spectrum of AuNPr grown with T30, G20, C30 and A30 at every minute for 10 mins. Absorbance values are coded with color spectrum blue to red from low to high absorbance value.

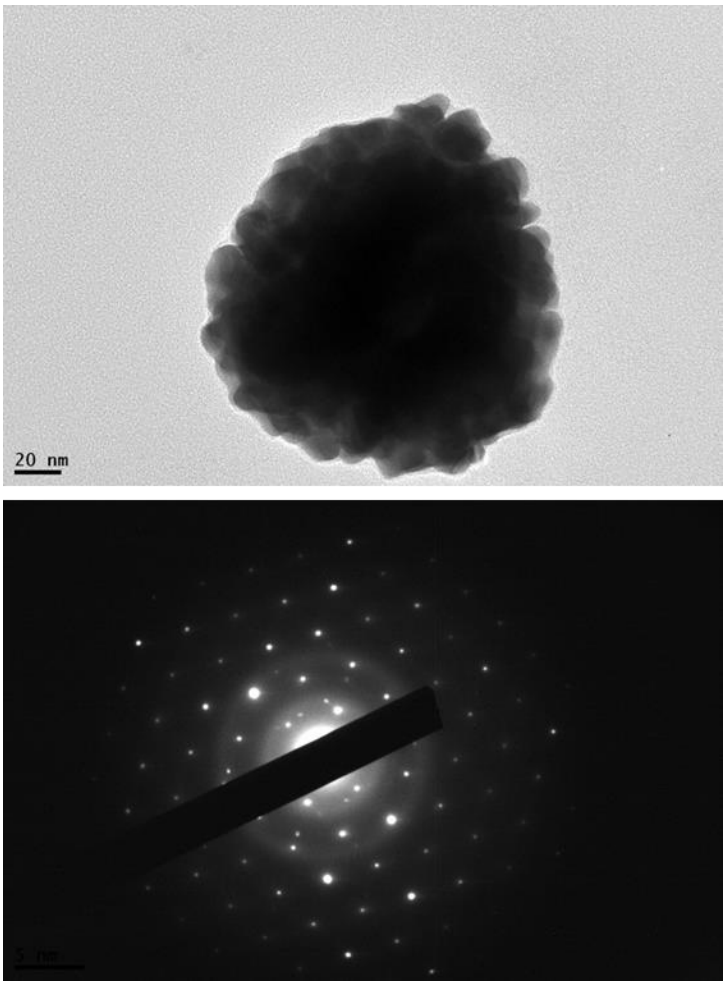

Figure 2.7. TEM image of A30 and the corresponding diffraction pattern of the particle.

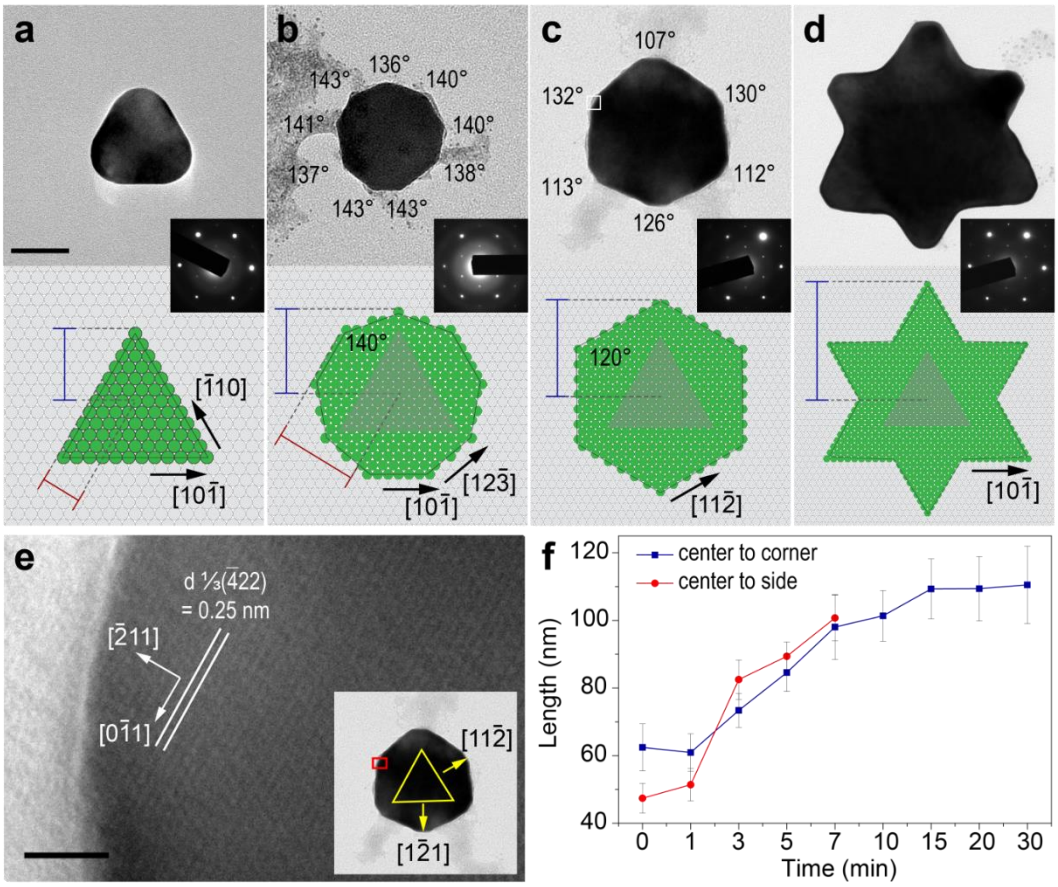

Figure 2.8. TEM images of progression of shape transition from prism to six-pointed star (a-d) with the model of the nanoparticle and diffraction pattern (inset). Scale bar = 50 nm. Blue and red lines on the models indicate the distance measured from the center of the particles to the corners and sides, respectively and plotted in (f). (e) TEM image of the hexagonal nanoparticle after 5 min of growth from AuNPr at high magnification. Scale bar = 2nm. Red box shows the location where the high resolution image was observed. The lattice direction indicates the orientation of the seed as outlined by the yellow trace. (f) Graph of the length of the nanoparticle measured from the center to the corner (blue) and center to the side (red) with time. The measured dimensions are defined on the models in (a-d).

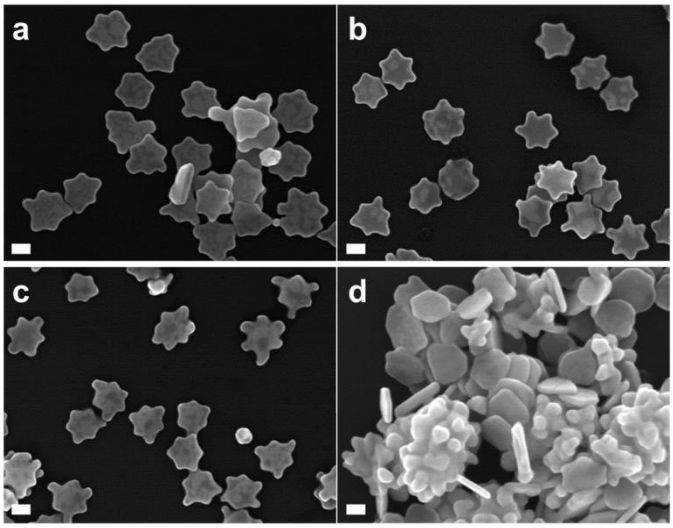

Figure 2.9. SEM images of AuNPr grown with T30 and at various reductant, HA, concentration (a) 0.5 mM, (b) 1 mM, (c) 2 mM, and (d) 4 mM. Scale bars = 100 nm

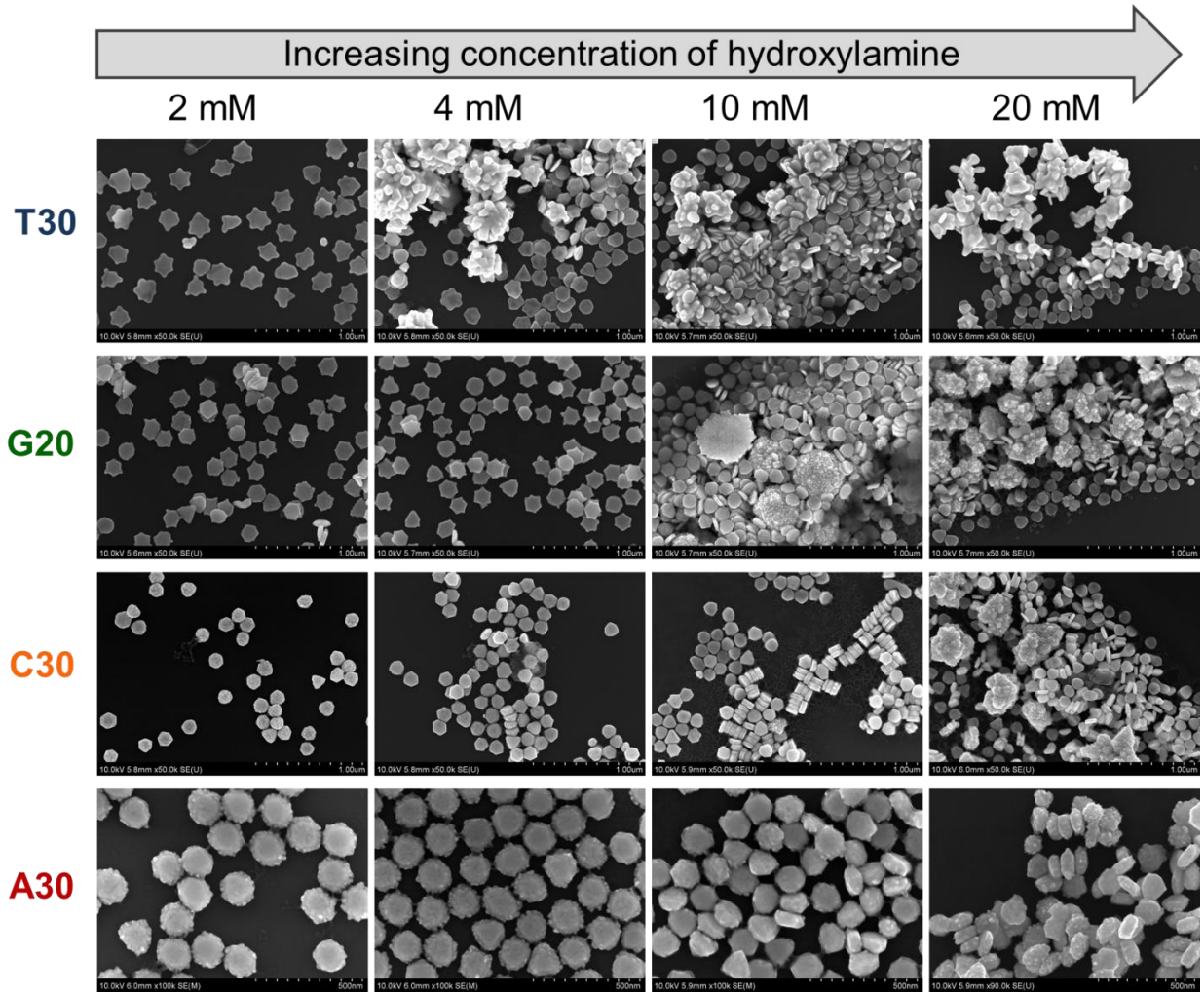

Figure 2.10. SEM micrographs of nanoparticles grown with T30, G20, C30 and A30 at hydroxylamine concentrations of 2, 4, 10 and 20 mM.

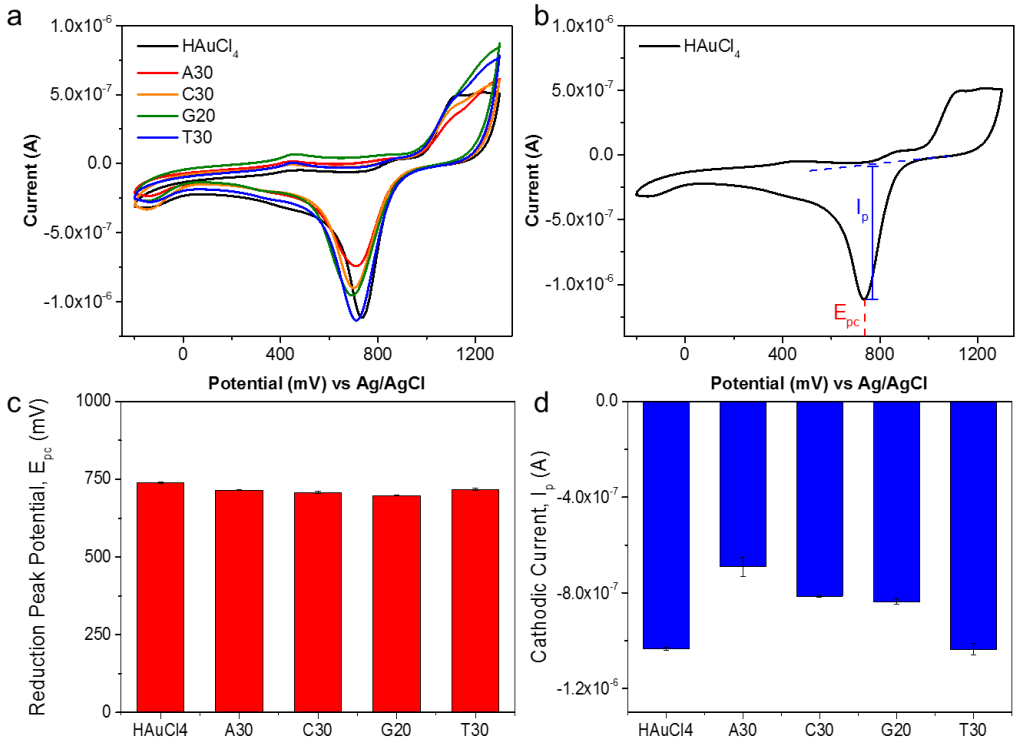

Figure 2.11. (a) Cyclic voltammogram of 0.5 mM $HAuCl_4$ performed on gold electrode and Ag/AgCl reference electrode in the absence and presence of various DNA sequences, (b) cyclic voltammogram showing the definition of reduction peak potential, E_{pc} and cathodic current I_p, (c) Bar graph showing no significant change in E_{pc} values for $HAuCl_4$ only and in the presence of A30, C30, G20 and T30, (d) Bar graph showing change in I_p values for $HAuCl_4$ and in the presence of A30, C30, G20 and T30.

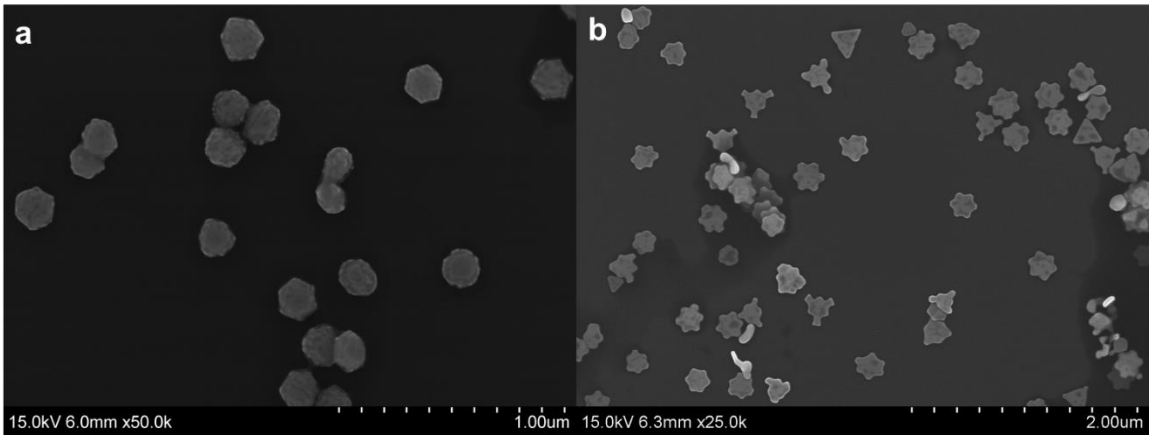

Figure 2.12. SEM images of the nanoparticles grown with fluorophore labelled (a) A30 and (b) T30.

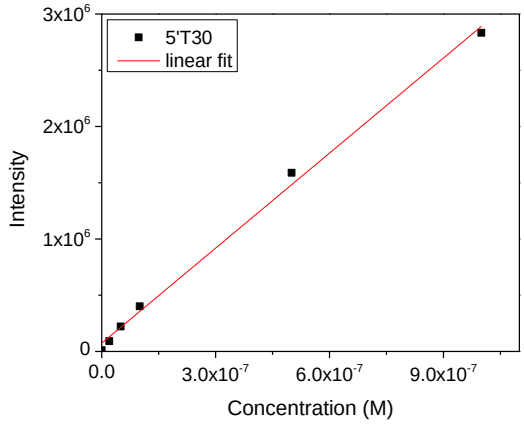

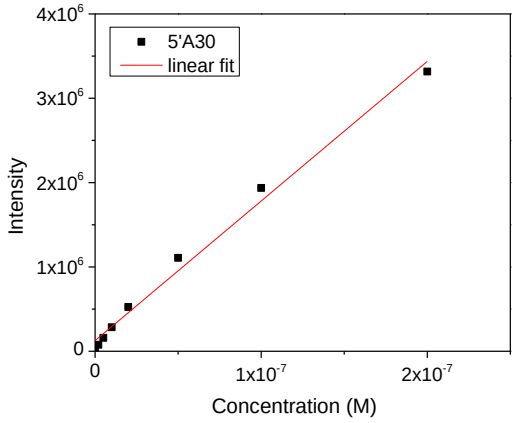

	Intercept	Slope	Adj. R-Square
T30	7E4 ± 4E4	282E10 ± 8E10	0.996
A30	13E4 ± 5E4	166E11 ± 7E11	0.989

	T30	std dev	A30	std dev
Intensity	1.63E+05		3.33E+06	
Supernatant	1.08E+04		6.62E+04	
Concentration of DNA	2.3E-07	2.E-08	1.4E-06	3.E-07
No. mols of DNA in 10ul solution	2.26E-12	2.E-13	1.4E-11	3.E-12
Concentration of AuNP	9.63E-09		5.7E-09	
Ratio	2.34E+01	2.E+00	2.41E+02	5.E+01

Figure 2.13. Calibration graphs of DNA quantification for T30 and A30 with intercept and calculation for the ratio of DNA for every AuNP after growth.

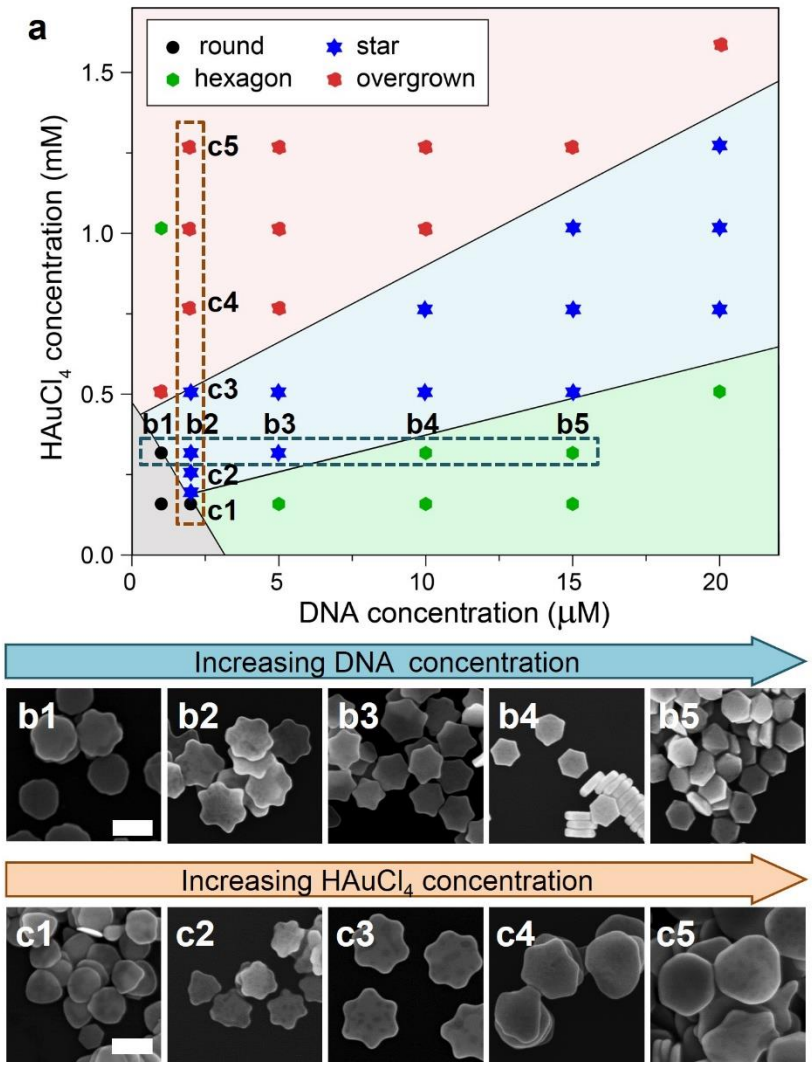

Figure 2.14. (a) Phase diagram for the shape of AuNPs obtained when nanoprism seeds were grown at a range of DNA T30 concentration from 1 μM to 20 μM and $HAuCl_4$ concentration from 0.19 mM to 1.9 mM. Each shape in the plot is experimentally proven. SEM micrographs at the bottom are representative of the samples indicated in the phase diagram with (b) increasing T30 concentration at constant 0.32 mM $HAuCl_4$ and (c) increasing $HAuCl_4$ concentration at constant 2 μM T30. Scale bar = 200 nm.

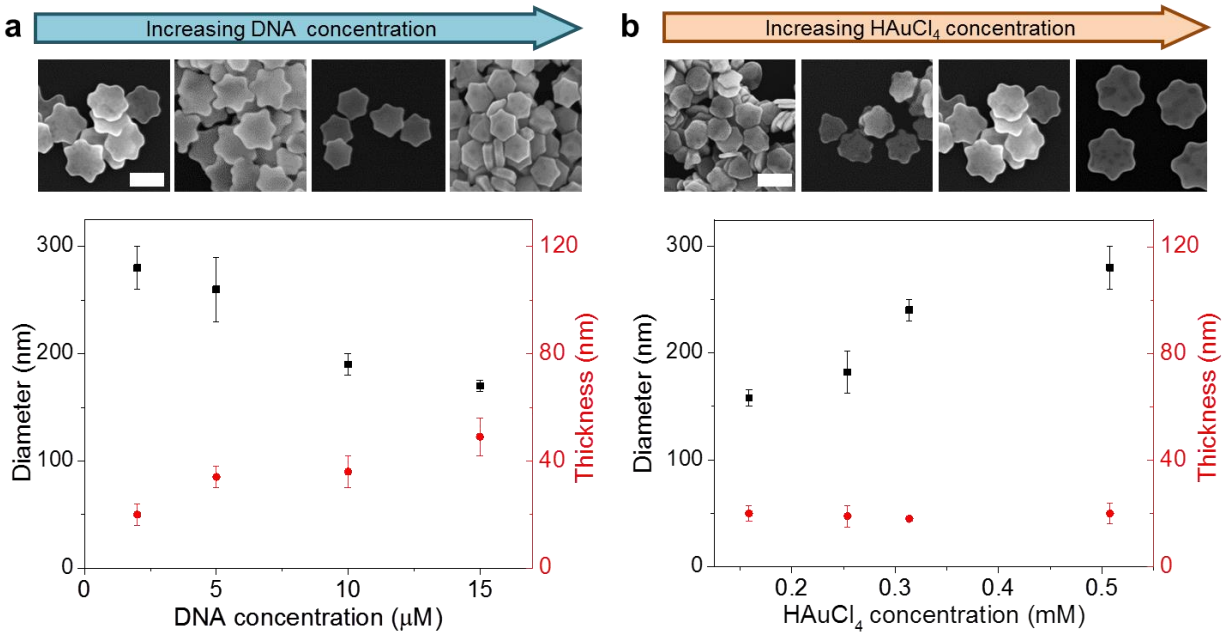

Figure 2.15. Graph showing the diameter and thickness of the nanoparticle measured from SEM micrographs against (a) DNA concentration at 0.5 mM $HAuCl_4$ and (b) $HAuCl_4$ concentration at 2 μM T30. Representative SEM images of each sample shown above the graphs. Scale bars = 200 nm.

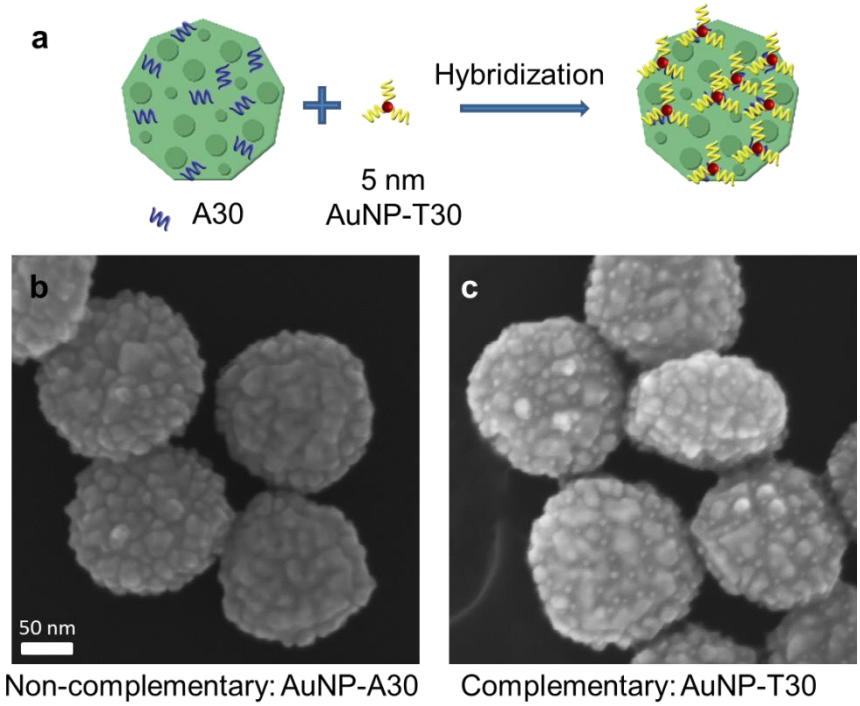

Figure 2.16. (a) scheme showing the approach in tracking the location of DNA on the nanoparticle grown with A30. SEM micrographs of nanoparticles grown with A30 hybridzed with (b) AuNP-A30 and (c) AuNP T30. SEM image of the particle incubated with non-complementary AuNP A30 shows no AuNP 5 nm were attached.

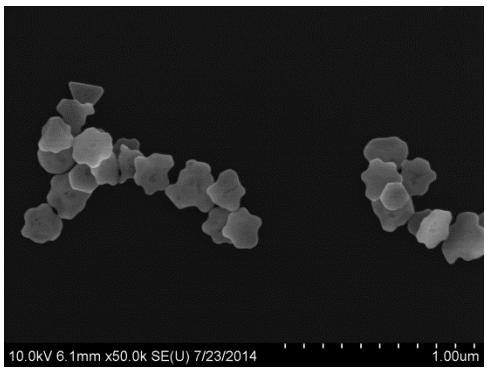

Figure 2.17. SEM micrographs of nanoparticles grown from nanoprism pre-incubated with A30 in the absence of excess DNA.

Scheme 2.1. Proposed mechanism of growth of gold nanoprisms influenced by DNA divided into two stages: shape control and thickness growth.

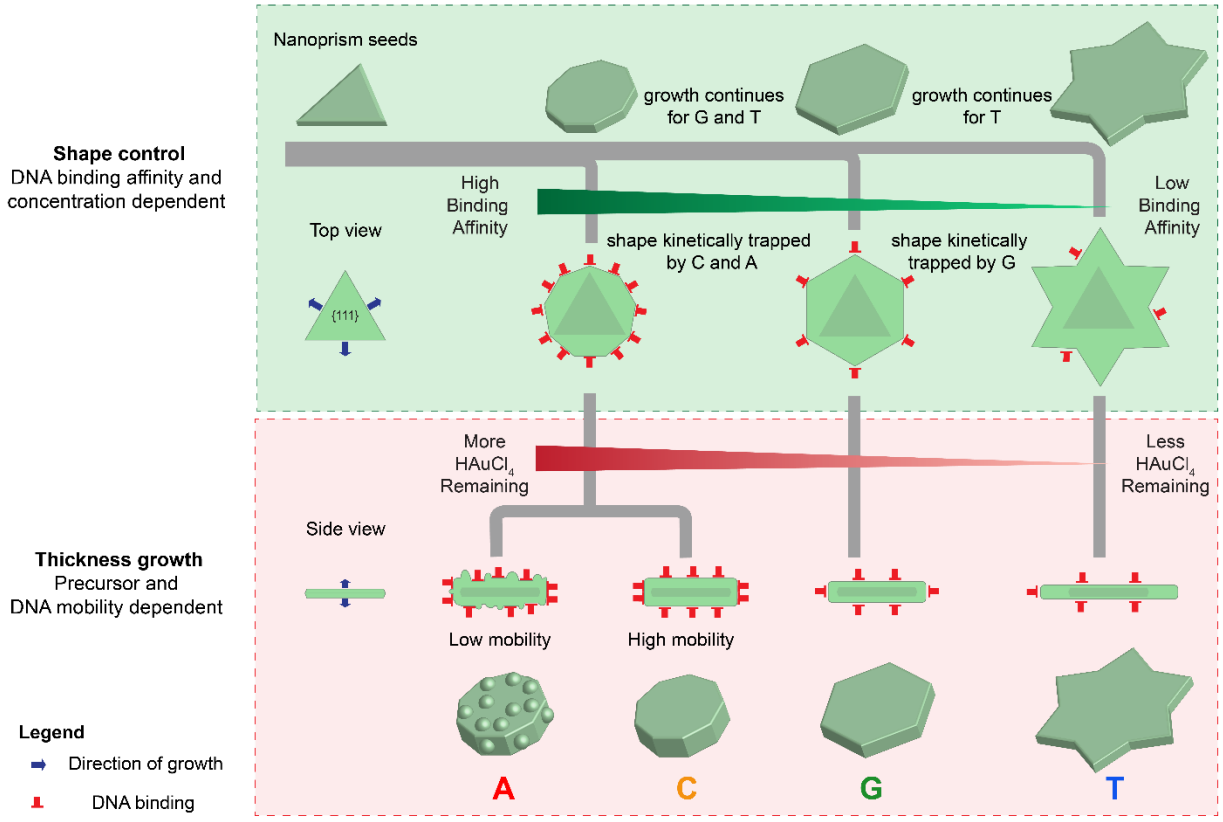

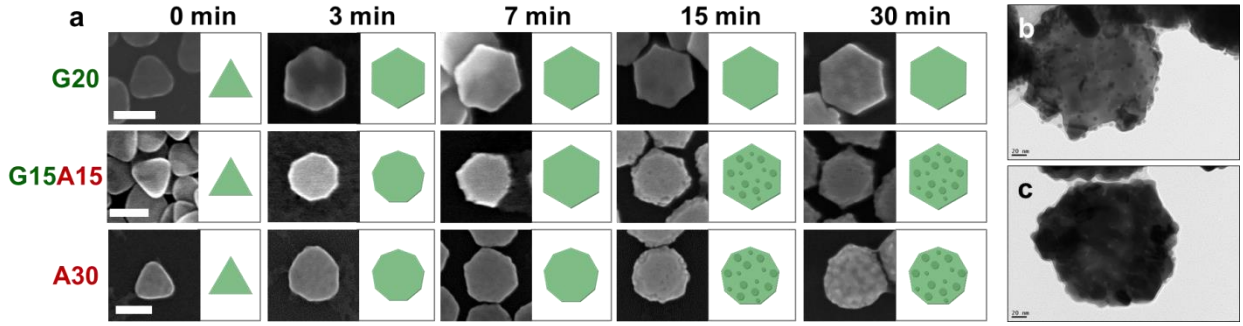

Figure 2.18. (a) Enlarged SEM images showing the morphological evolution of gold nanoparticles prepared with G20, G15A15, and A30 from 0 -30 min. Scale bars are 100 nm. Nanoparticle grown with G15A15 tested for hybridization with (b) AuNP-C and (c) AuNP-T which is complementary to G and C.

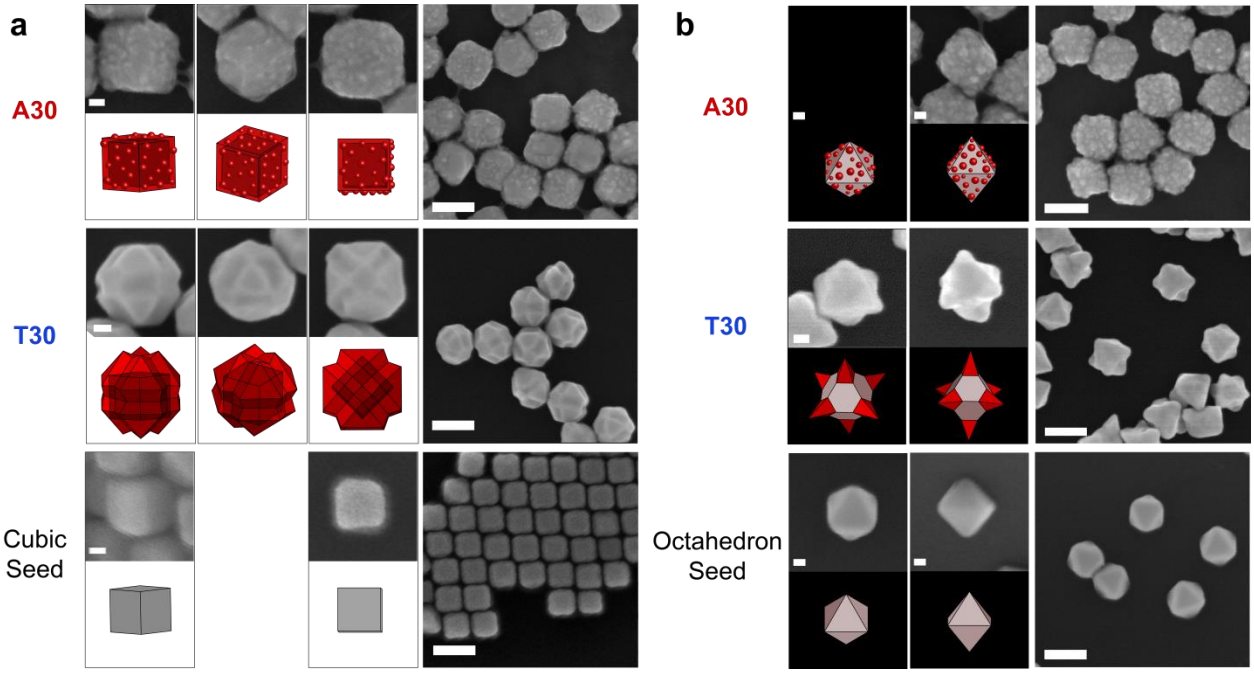

Figure 2.19. SEM images and corresponding schematics showing the morphology of the gold nanoparticles prepared with A30 and T30 with (a) cubic and (b) octahedron seeds on the left with large area image of the growth on the right. Scale bars are 20 and 100 nm respectively.

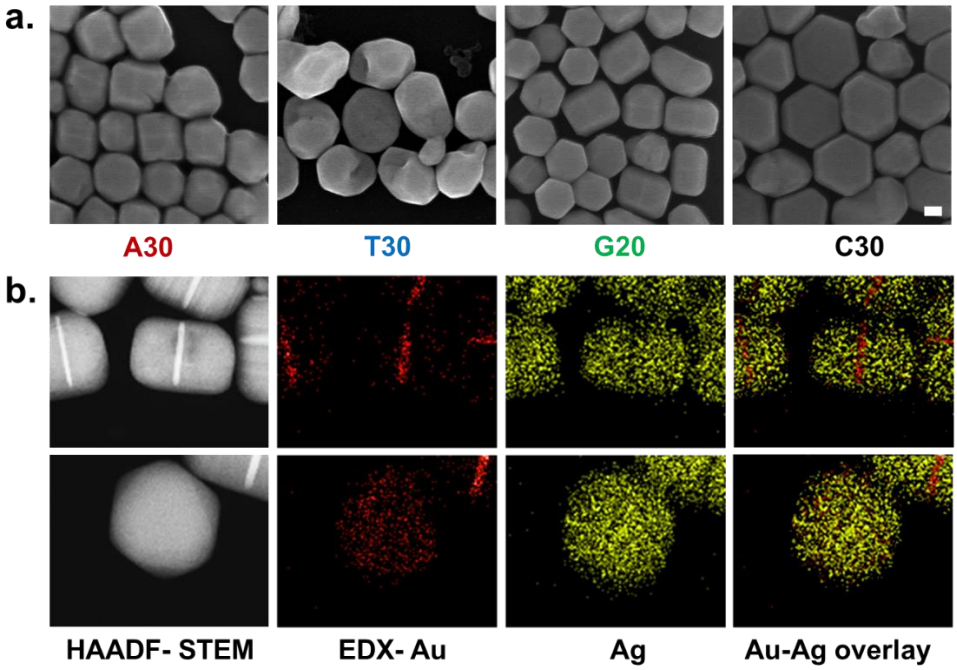

Figure 2.20. (a) SEM images of the Au nanoprism-Ag hybrid nanostructures synthesized in the presence of A30, T30, G20 and C30. Scale bar = 50 nm, (b) HAADF-STEM images for G20 sample in (a) from the sides and the top of the particle with bright regions corresponding to the Au seed. This is reaffirmed with the EDS mapping images for Au, Ag and their overlap.

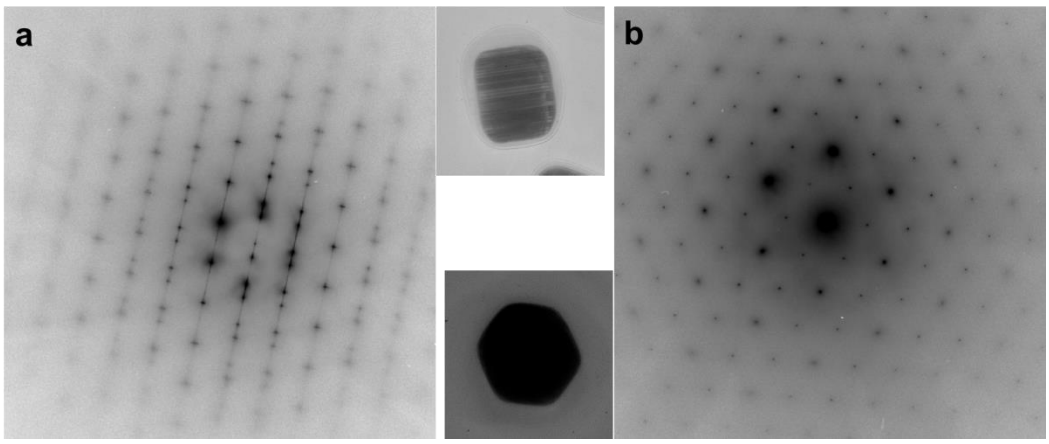

Figure 2.21. Selected area diffraction pattern of the hexagonal nanoparticle rod from the (a) side and (b) top surface of the particle grown with G.

CHAPTER 3

DIRECT IN SITU TEM OBSERVATION OF DNA MEDIATED SHAPE CONTROL OF NANOPARTICLE GROWTH BY CHEMICAL REDUCTION METHODS

3.1 Introduction

There are many models explaining the nucleation and growth of nanoparticles (NPs), however, the exact growth mechanism has not been elucidated until recently. This advancement is due to the development of the *in situ* liquid cell to directly observe the NP growth under transmission electron microscope (TEM).[1-6] Electron microscopy imaging is a powerful tool, as it has great spatial and temporal resolution for determining structures at the nanometer scale. The *in situ* study of colloidal NP synthesis was first reported by Zheng *et al.* where the authors demonstrated the growth of platinum NPs in the liquid cell with subnanometer resolution.[7] In this report, two mechanisms were observed: (1) nucleation from monomer attachment and (2) coalescence of nuclei to form a bigger particle. A combination of both processes occurs in the formation of NPs to result in a final colloidal solution of monodisperse particles. The growth of anisotropic NPs has also been investigated *in situ*. The formation of Pt_3Fe nanorods was observed to occur via attachment of NPs into long chains which then undergo fusion and straightening, and slowly undergo atomic rearrangement to result in formation of single-crystal nanorods.[8] In addition to the fusion process, breakdown of the NPs were also observed when the surfactant concentration was low and unable to stabilize the nanorods.[9] In addition to observing the morphological transition, the growth rates of different facets from a platinum seed to form platinum nanocubes were also determined. *In situ* TEM techniques have been used extensively to study other various aspects of NP growth including defect formation,[10] particle growth rates,[11] galvanic replacement

reactions,[12], oxidative etching,[13], Kirkendall effect,[14] preferential deposition and migration,[15] and formation of alloy NPs.[16]

We have recently report the use of DNA to tune the growth of gold (Au) nanoprisms in to various NP morphologies depending on the sequence of the DNA. The ability of DNA to program the growth is unprecedented and not observed with other ligands. Understanding how DNA could fine tune the shape of NPs is important to expand the programmability and predictability of NP growth. To shed light on the mechanism, we adopted the *in situ* TEM technique to monitor the NP growth using both the wet-cell and the flow-cell method. We first tested the use of wet-cell to observe the growth of Au nanoprisms in the presence of DNA and Au precursor by electron induced reduction. This method is more established but the growth through beam induced reduction may be different from the chemical based reduction.[17] Hence, we also tested the growth in a flow-cell where chemical reductants can be used in place of beam induced reduction. This condition better mimics the growth condition *ex situ*. However, the technique is fairly new and there are no reports yet on direct observation of NP growth from chemical induced reduction.

3.2 Results and Discussions

Wet-cell observation of growth: in collaboration with Liu Ying from Prof. Shen Dillon's group.

In a wet-cell setup, a reaction mixture, consisting of Au nanoprisms pre-incubated with DNA and solution, was added in between two layers of silicon nitride chips. One of the chips was deposited with a silicon oxide spacer of 100 nm to allow liquid to be trapped in between two chips. The assembled cell was sealed between two O-rings in a customized wet-cell holder to prevent evaporation of the liquid in the high vacuum environment of the TEM. The Au precursor was

added to the solution right before assembly of the cell. The electron dosage was controlled to induce or minimize deposition.

The stability of the Au nanoprisms in the presence of DNA without the addition of Au precursor was first monitored *in situ* to study the interaction of the electron beam with the Au nanoprisms. For Au nanoprisms incubated with T30 DNA strands, the Au nanoprisms were not stable in the wet-cell upon electron beam irradiation. We observed three effects on the NPs: dissolution, deposition and constant morphing of the NPs under the electron beam (Figure 3.1). Initially, the Au nanoprisms rapidly dissolved upon coming into view in the observation panel (Figure 3.1a). After observing dissolution at the initial stage, some of the observed NPs showed deposition of Au, where the NPs grew into larger structures (Figure 3.1b). The NPs grown under the influence of the electron beam constantly changed their shape (Figure 3.1c), indicating that both dissolution and deposition takes place simultaneously under the electron beam at a certain equilibrium concentration of Au precursor. This observation of both dissolution and deposition have been previously observed by Noh *et al.* for silver NPs.[18] Etching of NPs was observed to be due to generation of $OH^{\bullet}$ by electron beam interaction with the liquid.[7,20,21] The $OH^{\bullet}$ serves as an oxidant to oxidize Au(0), resulting in dissolution of the Au seeds. The conditions that would result in etching or deposition depended on the ratio of concentration of the hydrated electrons e_h^- which acts as the reducing agent, and $OH^{\bullet}$, the oxidizing agent.[19]. These observations indicate that the conditions in our experiments needed to be modified and finely tuned to balance the oxidation and reduction process to observe controlled growth of NPs under the TEM.

In addition to etching of the NPs, generation of the $OH^{\bullet}$ can also result in damage of the DNA ligand. To investigate the integrity of the DNA in the wet-cell, we tested the stability of AuNP clusters that were brought together by hybridization of DNA under the electron beam. If the

DNA was extensively damaged through cleavage at the phosphate backbone or removal of bases, the NPs would dehybridize and separate. For ease of observation AuNP of two sizes were used one 20 nm and the other 5 nm. Two examples of the NP clusters observed in the wet-cell are shown in Figure 3.2. The NP clusters were observed for approximately 4 min at different e-beam intensity in Figure 3.2a and approximately 11 min for the cluster in Figure 3.2b. However, none of the 5 nm AuNPs observed left the NP clusters, suggesting that the hybridization still remained. The distance between the 5 nm AuNP and 20 nm AuNP decreased or remain the same though the duration of beam exposure. There was no observation of merging or fusion of NPs, suggesting that the DNA still served as a good protecting layer for the AuNPs. These observation suggests that within the time frame observed, the extent of DNA degradation induced by hydroxyl radicals, if present, is not significant to the point that the AuNPs dehybridize or fuse with each other. Since the degradation of DNA is not extensive under the electron beam, the *in situ* TEM observation is a promising method for the DNA mediated NP growth.

The use of wet-cell to investigate the deposition of Au on Au nanoprisms in the presence of DNA was challenged by other difficulties mainly, the control of liquid cell thickness and the uncontrollable reduction of Au by the electron beam. The liquid thickness in the wet-cell varied depending on the assembly of the cell and influenced by the silicon spacer, the surface tension, and presence of excess liquid.[18] When a thick layer of sample is trapped in the cell, the signal to noise level is low as the background electron absorbance by the water layer is high. This is seen in Figure 3.3a where the NP is observed as a fuzzy grey shadow. A30 was used in this experiment and the Au seeds were expected to grow into round, rough structures. The NPs morphed from the seed into fuzzy rough structures but a detailed growth mechanism was not observed because of the high background.

The second issue is the ease of Au reduction under the electron beam which resulted in self-nucleation. The self-nucleation was observed at an Au precursor concentration of 0.5 mM in the wet-cell in the presence of T30 and was observed to be present even after the electron energy was lowered from 200 kV to 10 kV (Figure 3.3b). These results indicate that the concentration of Au precursor has to decrease to minimize self-nucleation. On the other hand, the amount of Au precursor supplied to the seed needs to be sufficient enough to allow growth of the NPs into the desired shape. These two problems are rather significant and needs to be addressed in order to directly observe the growth of NPs under the TEM microscope.

One method to solve the issues observed in our wet-cell experiments was to switch to a flow-cell system. The flow-cell system would have an open system for solution to flow in and out of the cell, offering several advantages.

1) The cell thickness is more controlled. Excess liquid can flow out of the cell during assembly thereby minimizing the cell thickness. With smaller cell thickness, better resolution will be obtained under the microscope.
2) Constant flow of solution minimizes the generation of hydroxyl radicals. The hydroxyl radicals generated from water, by the electron beam, will be constantly removed from the cell by the continuous flow of precursor, thereby minimizing effect of hydroxyl radical based oxidation of Au seeds or DNA degradation.
3) The concentration of Au precursor is controlled. With constant flow of Au precursor, a low concentration of Au precursor can be used to minimize self-nucleation or beam induced reduction. This method also supplies sufficient Au precursor to allow complete growth of the NPs.

4) Chemical reduction instead of electron beam reduction. The purpose of this project is to understand the growth of Au nanoprisms in the presence of DNA reduced by a mild reductant of hydroxylamine. The effect of electron based reduction might be different from chemical based reduction. The flow-cell design allows the precursor and reductant to be separated initially which was not possible with the wet-cell.
5) Induction of growth can be controlled. While the growth in the wet-cell is spontaneous upon electron beam irradiation, the flow-cell design allows control over the reduction depending on the introduction of Au precursor.

Flow-cell *in situ* monitoring of the growth

In a flow-cell setup, Au nanoprisms, DNA and hydroxylamine were first placed into the cell. The initial seeds were observed under the TEM prior to the growth where a flow of Au precursor of 0.2 mM will be introduced. The concentration of Au source was kept low to prevent self-nucleation or electron beam induced deposition.

In our first trial with the wet-cell, the nanoprisms incubated with T30 and hydroxylamine were clearly observed under the microscope indicating a smaller solution layer thickness in between the silicon nitride chips. Figure 3.4a shows an example of the NP before the reduction, which is prism in shape and stable under the electron beam. However, upon introduction of Au precursor, the sudden wave of solution washed away of a large amount of seed. When we found NPs back in the viewing screen, most of the growth had occurred and the shape remained stagnant even though more precursor was flowed into the flow-cell. Figure 3.4b shows the NPs after the flow of Au precursor, which grew into hexagonal structures. The shapes of the NPs were not the six-pointed stars that we expected but a possible intermediate in the formation of the six pointed

star. The arrested growth despite continuous flow of Au precursor indicated that NP growth was mainly controlled by the presence of the chemical reductant instead of the electron beam. The depletion or complete displacement of the hydroxylamine by Au precursor may have resulted in termination of particle growth.

With such promising results, we then collaborated with Dr. Tanya Prozorov and Dr. Taylor Woehl from Ames Laboratory. Dr. Prozorov and Dr. Woehl both have valuable experience in in situ monitoring of NPs and bacteria and were able to provide advice on the imaging the DNA mediated growth process of NPs. Subsequent *in situ* TEM experiments were carried out in Ames Laboratory.

Based on the previous experiment, the experiment design was modified to first flow hydroxylamine into the cell. The flow would minimize sudden fluid pressure and would supply the rest of the cell with a reservoir of hydroxylamine. The second change is that the STEM mode was used for imaging. STEM mode uses a small electron beam that scans across the imaging area. This limits the sample from having constant exposure to the electron beam and thereby minimizing the electron beam effect. In addition, STEM uses an annular dark-field detector which can detect heavy elements at a better signal to noise ratio.

Observation with A30

When the cell was assembled with prisms that were pre-incubated with A30, the prisms did not stick well to the window on the silicon nitride membrane. Only some of the NPs were attached to the window while many were flowing around, resulting in the observation of white streaks on the image when solution was pumped through the cell, as shown in the middle left side

of Figure 3.5a. The lack of NPs attached to the window might be due to strong charge repulsion between the negatively charged backbone of DNA and the negatively charged surfaces of the Si_3N_4 membrane upon plasma treatment. Despite that, a few NPs adhered to the window and we were able to observe growth of the fixed NP clusters. Initially, we did not observe any growth or Au deposition with 0.1 mM of $HAuCl_4$ (Figure 3.5b). At a higher concentration of $HAuCl_4$ (1 mM), the prisms started to grow into big, rough structures (Figure 3.5c). Although the formation of a rough particle is consistent with A30 growth, we suspect that the reduction may have occurred through both rapid electron beam reduction and chemical reduction as small amount of self-nucleation was observed during the growth. Using a lower concentration of 0.5 mM $HAuCl_4$, we observed that the Au nanoprisms also grew into rough structures (Figure 3.5d). However, the prism shape of the NP did not change significantly and only became rough. In the future, we intend to determine if the reduction and formation of roughness is due to the presence of A30 by observing *in situ* growth of Au nanoprism seeds without DNA and with different DNA nucleobases.

Observation with T30

For *in situ* growth with T30, we chose 0.2 mM $HAuCl_4$ to be flowed into the cell. This lower concentration is chosen based on our experience with A30 to prevent self-nucleation of Au but still high enough to allow for NP growth. Unlike the samples with A30, there were fewer clustered NPs and several NPs were found close to the edge of the window where the layer of liquid is thinner and the resolution is better. The growth progressions of the prisms mediated by T30 are shown in figure 3.6. Before the flow of precursor, some of the seeds remain triangular in shape, while some are round, due to the truncation of the tips of the prism. Upon introduction of $HAuCl_4$, we observe a small amount of deposition on each of the NPs. Even though we continued

to flow the Au precursor for another 1 hr and 30 min, there was little growth after initial deposition. This observation was similar to our previous observation, when the reductant has been depleted and no further deposition was observed. We subsequently switched to flowing 50 µL of hydroxylamine into the cell and continued with another 60 to 70 µL of Au precursor. With re-introduction of hydroxylamine and Au precursor, we observed additional growth on the NPs. The times when Au precursor was reintroduced are indicated by yellow arrows in Figure 3.6. This process was repeated three times before we observed the formation of six-pointed stars on some of the NP seeds.

Morphological evolution of the NPs was analyzed. For seeds which are initially triangular in shape, it was noted the sides of the prisms grew outwards to form a hexagonal shape (Figure 3.6a, b, and c). The tips of the hexagonal shape then continued to grow into six-pointed stars. When the seeds were round plates, it was observed that the round NPs started to grow specifically on 6 regions to form into hexagonal plates (Figure 3.6d and e). The subsequent growth from hexagon shape into six pointed star was similar. These observations where the sides of the nanoprisms would grow, are consistent with our *ex situ* mechanistic studies. However, there were slight differences, we did observe the formation of a nonagon intermediate our *ex situ* studies, but the *in situ* TEM results from Figure 3.6a–c suggest that the round/nonagon intermediate is not a necessary intermediate. Nevertheless, if the NPs did transform through a spherical intermediate, the hexagonal shape intermediates will be similarly formed. Unfortunately, we were not able to observe the growth of the NPs directly without continuous switching of the reactants. This limits our ability to determine the growth kinetics of the NPs.

Using a Y-connector

As the cell is rather small, at hundreds of nanometers, fluid mixing in the cell is challenging, and what we observed was the active displacement of one reactant by another reactant, hence the growth only occurred at the interface where the two reactants meet. To allow continuous flow of reactant, we decided to use a Y-connector to combine and mix both reductant and Au precursor together at a joint prior to entering the TEM holder and the cell. However, when the two reductant and Au precursor was mixed together prior to entering the cell, we did not observe any growth on the prisms. Small fuzzy NPs of approximately 5 nm were observed to attach on to the seed. When the reductant flow was removed and only the Au precursor was used, we started observing deposition on the Au nanoprisms. This suggested that the precursor and reductant reacted completely in the lines prior to entering the cell. When the rate of the flow was increased from 5 μL/ min to 10 μL/ min to reduce the time for the precursor and reductant to react, similar phenomenon was observed (Figure 3.7a). The fuzzy particles continued to grow as a layer of aggregated particles on the seed surface. Figure 3.7b shows enlarged images of the nanoprism coated with a layer of these small particles, further confirming that the reactant fully reacted in the lines and formed NPs prior to reaching the cell. In order to improve the design, mixing of the two reactant has to be done in the cell, or the time taken for the reactants to reach the cell after mixing should be minimized.

3.3 Conclusions

We performed *in situ* investigation of the growth of the Au nanoprisms guided by DNA using both the wet-cell and the flow-cell design under the TEM. Using the wet-cell, we observed electron beam induced dissolution, deposition and shape changes. The parameters in the wet-cell were less controlled as self-nucleation occurred under the electron beam and both homogeneous

and heterogeneous growth occurs. Using the flow-cell, the growth of NPs with A30 and T30 were more controllable, as the flow of precursor could be lowered in concentration to minimize electron beam induced self-nucleation and growth. Using the flow-cell also allowed the use of reductant prior to addition of the Au precursors. The addition of a chemical reductant allowed direct observation of chemically induced reduction of Au, similar to *ex situ* growth conditions. We observed, for T30, the transition from nanoprisms to six-pointed star by flowing an alternating source of reductant and precursor. This observation suggests that the method shows promise in observing *in situ* growth of NPs.

Pre-mixing of the reductant and precursor using a Y–connector prior to entering the cell unfortunately did not work as the complete reaction of the reductant and precursor formed small NPs by the time the solution reached the cell. Future directions should focus on improving the mixing of the two reactants by changing the cell design or developing a micro-mixing connector that is installed close to where the solutions enter the cell.

3.4 Experimental Section

Wet-cell TEM investigation

Commercial silicon nitride support windows were purchased from Ted Pella Inc., Redding, CA. Some of the silicon nitride support windows were patterned with a silica spacer of a 100 nm thickness via shadow masked electron beam physical vapor deposition. To assemble into a cell, a solution of Au nanoprisms, pre-incubated with DNA (1.0 μL), was added in between two silicon nitride windows (500 μm×500 μm×200 nm), one with a silica spacer and one without. When deposition was investigated, Au precursor was added into the solution. The wet-cell used for this

study was custom designed by the Dillon group.[22] The sample was confined between the windows and sealed in the cell with two O-rings (see scheme of the wet-cell in Figure 3.8[18]). The cell was assembled by Mr. Liu Yin from the Dillon group. Gold nanoprisms were synthesized from a previously reported method and described in detail in chapter 2. The samples were characterized under the JEOL 2010 LaB_6 TEM. The beam current density used was limited to between 0.05 mA/cm^2 to 947 mA/cm^2 to control the electron beam effect of dissolution or induced deposition. Videos of the experiments were recorded using Ulead DVD Movie Factory and Gatan Digital Micrograph at a frame rate of five frames per second.

Flow-cell TEM investigation

The flow-cell TEM investigation in UIUC was performed under the guidance of Dr. Jianbo Wu from Prof. Hong Yang and Prof Jim Zuo's group. The protocol was adapted from the experiments carried out by Dr. Jianbo in a recent report.[15] The *in situ* TEM observation was carried out on a JEOL2100Cryo TEM with a LaB6 emitter at 200 kV using the Hummingbird Scientific Liquid Flow TEM Holder. During observation, a beam current density of 2 pA/cm^2 on screen was used. Electron images were recorded using a Gatan Ultrascan CCD camera installed on the JEOL2100Cryo TEM. The bright field TEM images were taken using an exposure time of 1 s.

Flow-cell STEM investigation

The flow-cell protocol was adopted from the previous report by Prozorov and coworkers in imaging bacteria cells in the flow-cell.[23] A continuous flow fluid cell holder platform (Hummingbird Scientific, Lacey, WA, USA) was used. To assemble the cell, a thin layer of sample (typically 100–500 nm thick) was formed by sandwiching two silicon nitride coated silicon chips.

The silicon nitride layer is 50 nm thick and is electron transparent. Two silicon nitride spacer chip (100 nm spacer) were treated in UV/O_3 plasma for 30 min to clean the chips and render them hydrophilic. A spacer chip was first placed in the fluid cell holder. 0.5 µL of sample was added to another cleaned spacer chip and was flipped over and sandwiched on top of another spacer chip in the fluid cell holder. Scanning Transmission Electron Microscopy (STEM) imaging and characterization was performed using a 200 kV FEI Tecnai G^2 F20 (S)TEM equipped with a Tridium Gatan image filter. The cell was imaged in STEM mode with a HAADF detector.

The sample of prisms were prepared using 10x concentrated prism. 10 µL of Au prism were incubated with 2 µL of 100 µM DNA. After incubation of at least 15 min, 0.1 µL of hydroxylamine 200mM was added to the mixture. This mixture was added in between the two spacer chips. The line in the TEM holder was rinsed with 2 mM hydroxylamine.

After the sample holder was inserted into the TEM, 100 µL of 2 mM hydroxylamine was pumped through the cell. Subsequently, 0.2 mM $HAuCl_4$ was pumped at 5 µL/min for about 60 – 70 µL before growth was observed. When no further growth was observed, 50 µL of hydroxylamine was pumped into the cell followed by another 60 – 70 µL of 0.2 mM $HAuCl_4$.The images were taken at spot size 9 and 110k magnification.

3.5 References

(1) Grogan, J. M.; Bau, H. H. *J. Microelectromech. Syst.* **2010**, *19*, 885.

(2) Klein, K. L.; Anderson, I. M.; De Jonge, N. *J. Microsc.* **2011**, *242*, 117.

(3) de Jonge, N.; Ross, F. M. *Nature Nanotech.* **2011**, *6*, 695.

(4) Parsons, D. F. *Science* **1974**, *186*, 407.

(5) Jonge, N. d.; Peckys, D. B.; Kremers, G. J.; Piston, D. W. *Proc. Natl. Acad. Sci.* **2009**, *106*, 2159.

(6) Ring, E. A.; de Jonge, N. *Microsc. Microanal.* **2010**, *16*, 622.

(7) Zheng, H. M.; Smith, R. K.; Jun, Y. W.; Kisielowski, C.; Dahmen, U.; Alivisatos, A. P. *Science* **2009**, *324*, 1309.

(8) Liao, H. G.; Cui, L. K.; Whitelam, S.; Zheng, H. M. *Science* **2012**, *336*, 1011.

(9) Liao, H.-G.; Zheng, H. *J. Am. Chem. Soc.* **2013**, *135*, 5038.

(10) Aabdin, Z.; Lu, J.; Zhu, X.; Anand, U.; Loh, N. D.; Su, H.; Mirsaidov, U. *Nano Lett.* **2014**, *14*, 6639.

(11) Woehl, T. J.; Park, C.; Evans, J. E.; Arslan, I.; Ristenpart, W. D.; Browning, N. D. *Nano Lett.* **2014**, *14*, 373.

(12) Sutter, E.; Jungjohann, K.; Bliznakov, S.; Courty, A.; Maisonhaute, E.; Tenney, S.; Sutter, P. *Nat. Commun.* **2014**, *5*.

(13) Jiang, Y.; Zhu, G.; Lin, F.; Zhang, H.; Jin, C.; Yuan, J.; Yang, D.; Zhang, Z. *Nano Lett.* **2014**, *14*, 3761.

(14) Niu, K.-Y.; Park, J.; Zheng, H.; Alivisatos, A. P. *Nano Lett.* **2013**, *13*, 5715.

(15) Wu, J.; Gao, W.; Wen, J.; Miller, D. J.; Lu, P.; Zuo, J.-M.; Yang, H. *Nano Lett.* **2015**.

(16) De Clercq, A.; Dachraoui, W.; Margeat, O.; Pelzer, K.; Henry, C. R.; Giorgio, S. *J. Phys. Chem. Lett.* **2014**, *5*, 2126.

(17) Liu, Y.; Tai, K.; Dillon, S. J. *Chem. Mater.* **2013**.

(18) Noh, K. W.; Liu, Y.; Sun, L.; Dillon, S. J. *Ultramicroscopy* **2012**, *116*, 34.

(19) Schneider, N. M.; Norton, M. M.; Mendel, B. J.; Grogan, J. M.; Ross, F. M.; Bau, H. H. *J. Phys. Chem. C* **2014**, *118*, 22373.

(20) Hart, E. J. *Science* **1964**, *146*, 19.

(21) Evans, J. E.; Jungjohann, K. L.; Browning, N. D.; Arslan, I. *Nano Lett.* **2011**, *11*, 2809.

(22) Chen, X.; Noh, K. W.; Wen, J. G.; Dillon, S. J. *Acta Mater.* **2012**, *60*, 192.

(23) Woehl, T. J.; Kashyap, S.; Firlar, E.; Perez-Gonzalez, T.; Faivre, D.; Trubitsyn, D.; Bazylinski, D. A.; Prozorov, T. *Sci. Rep.* **2014**, *4*.

3.6 Figures

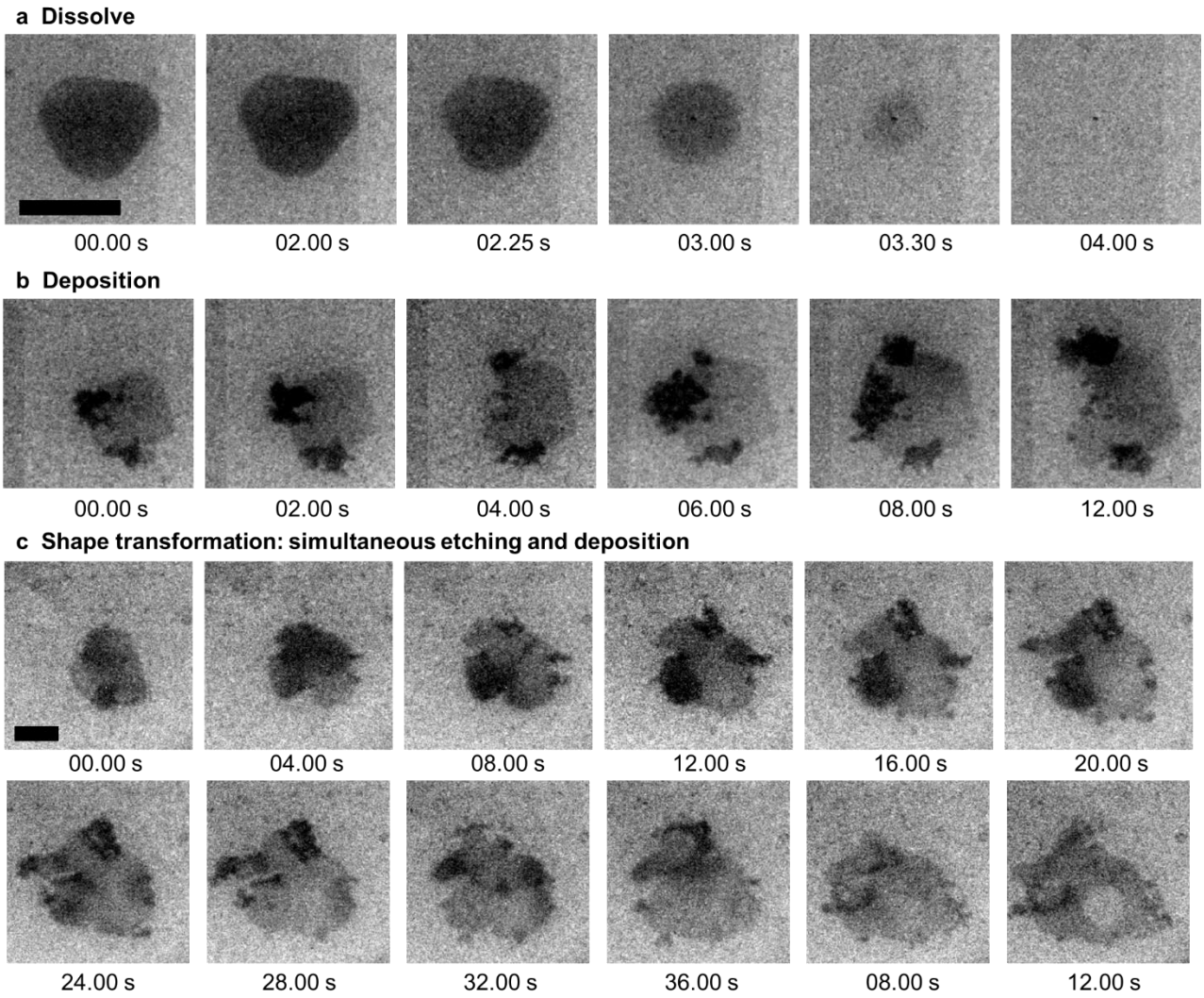

Figure 3.1 Snap-shots from a video recorded while *in situ* monitoring the effects of the electron beam on Au nanoprisms incubated with T30 in the wet-cell showing (a) dissolution of the nanoprism, (b) dendritic deposition of Au on the nanoprism, and (c) simultaneous etching and deposition of Au. Scale bar: 100 nm

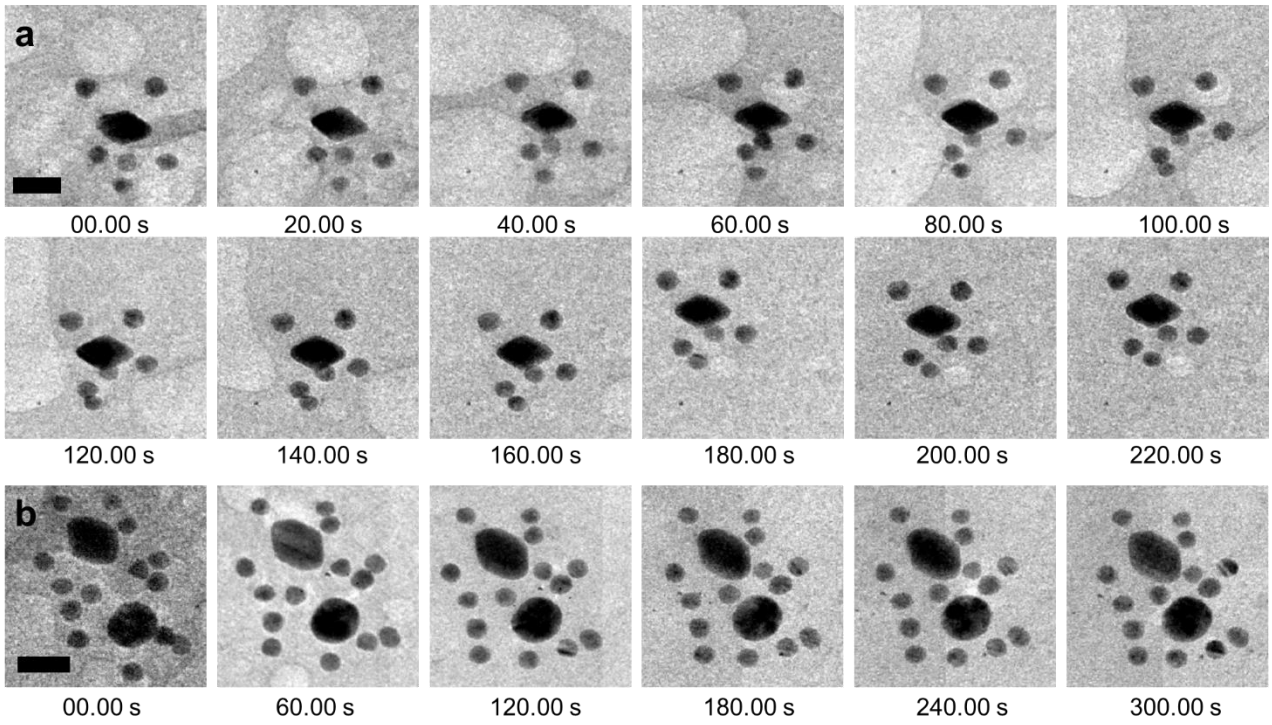

Figure 3.2 Snap-shots from *in situ* monitoring of the stability of DNA under the electron beam. The extent of DNA degradation was determined by observing the stability of AuNP cluster assembled together by DNA hybridization. (a) and (b) show two different set of NP clusters and their changes with time. Scale bar: 20 nm

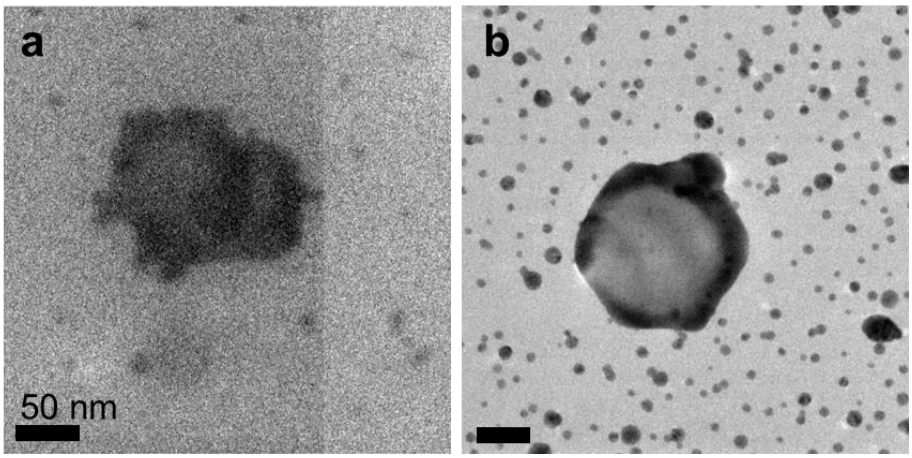

Figure 3.3 (a) A TEM snap-shot from *in situ* monitoring of the growth of Au nanoprisms incubated with A30 by electron beam induced deposition of Au precursor in the wet-cell. Note that the shape of the NP is not clear due to high background from the thick layer or water. (b) A TEM image of the Au nanoprism pre-incubated with T30 and growth induced by 10 kV of electron beam using SEM at 0.5 mM $HAuCl_4$ concentration. The wet-cell was placed in the SEM for electron irradiation and the cell was opened, dried and observed under normal TEM imaging conditions.

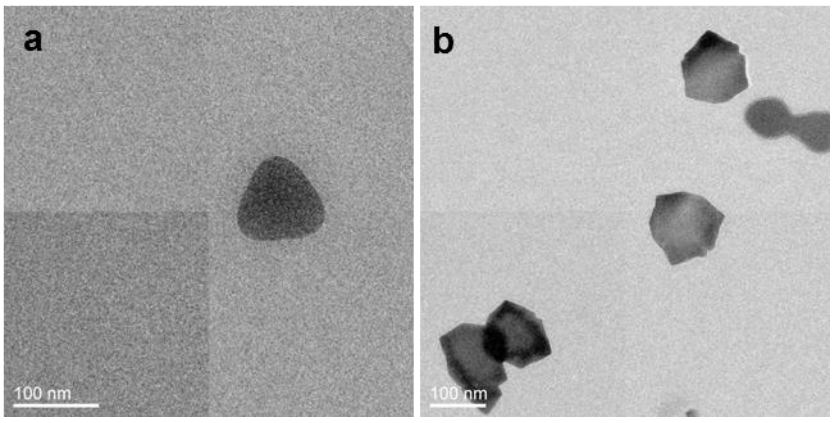

Figure 3.4 TEM images of the Au nanoprisms pre-incubated with T30 (a) before the flow of $HAuCl_4$ and (b) after the flow of $HAuCl_4$.

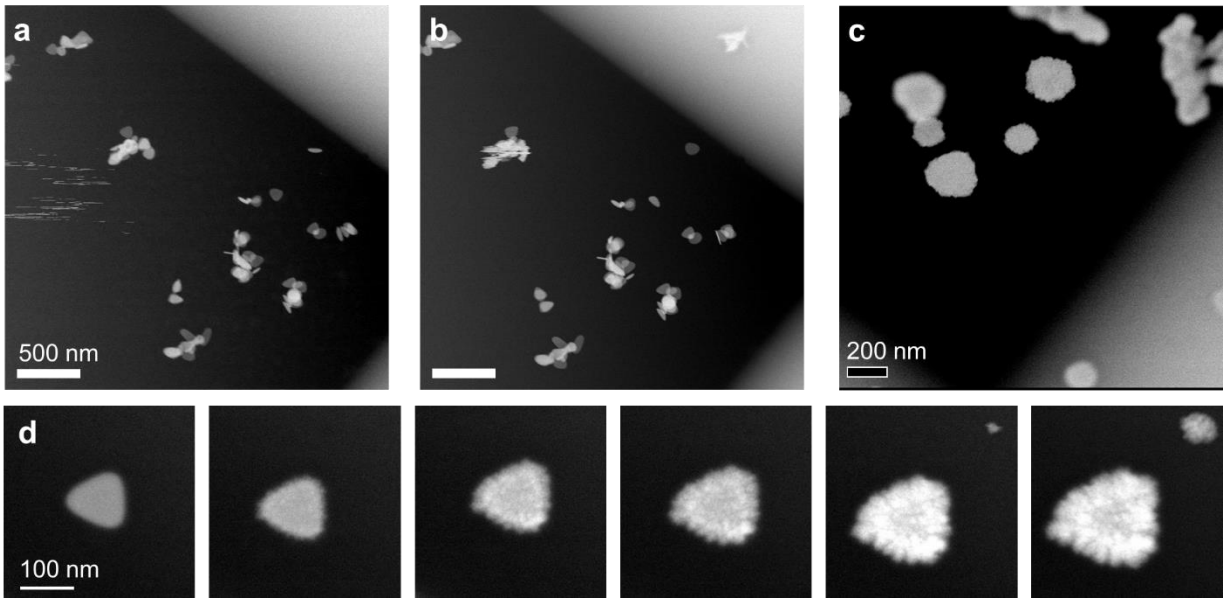

Figure 3.5 STEM images of the Au nanoprism pre-incubated with A30 (a) before the flow of $HAuCl_4$ and (b) after the flow of 0.1 mM $HAuCl_4$ and (c) 1 mM $HAuCl_4$. (d) Snap-shots of STEM images of the growth of Au nanoprism pre-incubated with A30 over time while flowing 0.5 mM $HAuCl_4$.at 5 μL/mL.

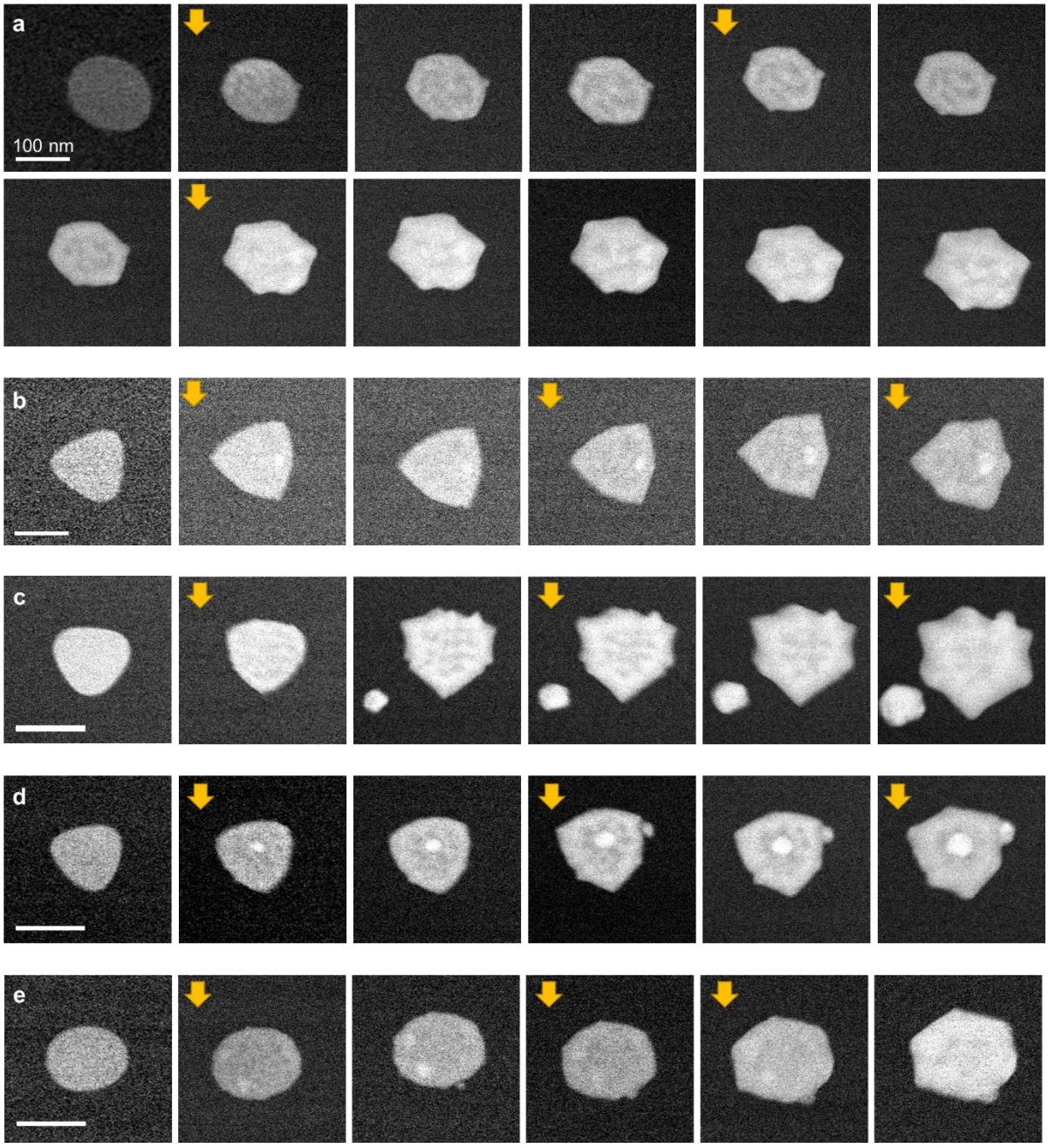

Figure 3.6 Snap-shots of STEM images of the growth of Au nanoprism pre-incubated with T30 with time, upon flow of 0.2 mM $HAuCl_4$ at 5 µL//mL for five different nanoparism a-e. Each yellow arrow indicates flow of 2 mM HA into the cell followed by 0.2 mM $HAuCl_4$.

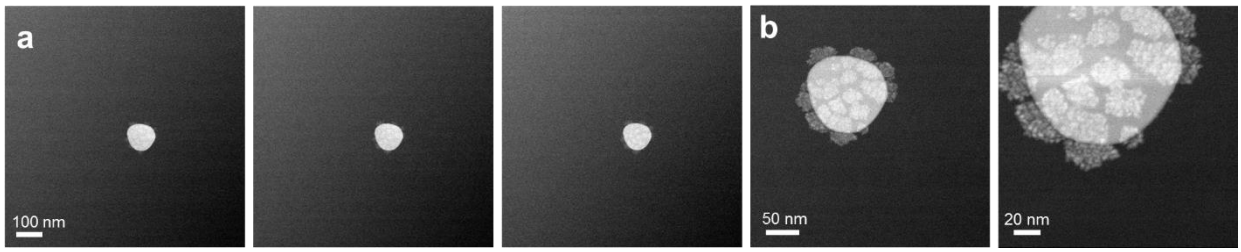

Figure 3.7 (a) Snap-shots of STEM images of the growth of Au nanoprism pre-incubated with T30 with time, upon flow of a mix of 2 mM HA and 0.5 mM $HAuCl_4$ using a Y-connector showing no change in the shape of the prism seed and the growth of a fuzzy coating on the NP. (b) Magnified STEM micrographs of the prism showing that the fuzzy coating consists of AuNPs 5 nm in size.

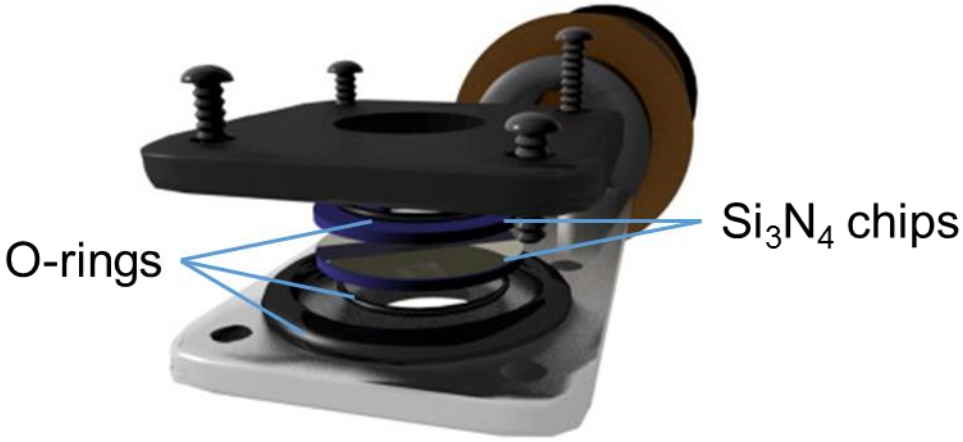

Figure 3.8 Schematic of the wet-cell assembly showing the silicon nitride chips sandwiched together to form the cell and sealed by O-rings in the wet-cell holder. Figure adopted from ref. 18.[18]

CHAPTER 4

PH-DEPENDENT EVOLUTION OF NANOPARTICLE GROWTH MEDIATED BY DNA

4. 1 Introduction

The formation of nanoparticles with specific sizes and shapes are important as the shape and size determine the properties of the nanoparticles.[1-4] Understanding the reaction mechanism is important to allow better control over nanomaterial synthesis.[5-7] In an aqueous based nanoparticle synthesis reaction, the growth can be affected by various factors, including chemical precursor, concentration, impurities, temperature, pH, time, and light.[3,5,8] One factor that is important but not emphasized is the pH of the reaction solution. The nanoparticles synthesis are typically performed in water where the reaction pH is dependent on the reactants and no buffering agent are used to maintain reaction pH. The importance of pH was highlighted when long establish Turkevich method was improved significantly by tuning the reaction pH.[9] Through studying the influence of pH, Ji et al. reported that a high pH was found to be a key for controllable and homogenous nanoparticle synthesis for the citrate reduction method as the gold species became hydroxylated and reduced in reduction potential.[10,11] Acid or base additives in reactions can influence nanoparticle growth,[10,12-17] metal deposition on nanoparticle seeds,[18-20] formation of clusters,[21,22] galvanic replacement reactions,[23] underpotential deposition,[24] and oxidative etching process on nanoparticles[25]. The three major effects of pH are the species of metal precursor,[11,16,26] the reduction rate of the reactants,[13,14,17,27] and binding of the ligands[21,22,28].

The use of biomaterials in controlling the growth of nanomaterials is a promising field.[29] DNA has demonstrated unparalleled control over tuning the shape of nanoparticles. We have

previously reported the use of DNA to programmably control the growth of nanoparticle.[30-32] The programmable growth was achieved using homopolymer of DNA bases thirty bases of adenine (A30), thymine (T30), cytosine (C30), and twenty bases of guanine (G20) to direct the reduction of gold on to gold prism seeds using hydroxylamine (HA) as the reductant.[30] The gold nanoprism were grown into round rough plates for A30, six-pointed star for T30, hexagon plates for G20 and round flat plates for C30. In addition we found that by using diblock homopolymers of DNA bases, we can fine tune the morphology of the nanoparticle. For example, combination of G20 which forms hexagon plates and A30 which forms round rough plates, G15A15 grows into rough hexagon plates.

Despite the promise, one of the biggest challenge in DNA mediated synthesis is that like many other nanoparticle synthesis reactions the process can be influenced by small variations in condition. Here we aim to understand the mechanism of DNA mediated nanoparticle synthesis by monitoring the pH evolution and tuning the pH profile by addition of small amount of buffer into the growth solution.

4. 2 Results and Discussions

We first investigated the pH profile of the growth of the nanoparticle in the presence of different DNA (Figure 4.1). In our reaction we observed a rapid decrease in the pH of the reaction from around pH 3.5 initially to about pH 2.75 in 30 min. The change in the pH was found to be more significant for T, as compared to G, A or C. To understand the contribution to the initial pH, the pH of prism and DNA solution were measured to be approximately 5.5, pH of hydroxylamine at 2 mM concentration was approximately 4.9 and pH of $HAuCl_4$ at a concentration of 0.5 mM was 2.9. The acidity observed at initial time is due to the presence of $HAuCl_4$ which will dissociate

rapidly to form H^+ and $AuCl_4^-$. As the reaction progressed, the pH of the reaction drops. The protons generated were mainly contributed by the oxidation process of hydroxylamine. The oxidation reaction of hydroxylamine are shown in equation (1) and (2). One or two protons were generated for every hydroxylamine oxidized depending if the reaction is a one electron oxidation or two electron oxidation process. [33-35]

$$NH_2OH \rightarrow \frac{1}{2}N_2 + H_2O + H^+ + e^- \quad (1)$$

$$NH_2OH \rightarrow \frac{1}{2}N_2O + \frac{1}{2}H_2O + 2H^+ + 2e^- \quad (2)$$

Hence the drop pH can be used to indicate reaction progression as it reflects how much gold would have been reduced. While the reaction is completed within 10 min for T, the other bases up to 30 min for the reaction to be completed.

Effect of pH on the growth of nanoparticles

To study the effect of pH on the growth of nanoparticles, a small amount of buffer at various pHs were added to the growth solutions and the resulting nanoparticles grown were characterized under scanning electron microscopy. Based on our previous measurements of the reaction pH profiles, we prepared buffers that ranges from pH 1.5 to pH 5 to test the effect of the pH on the growth. Buffers at low pHs, between pH 1.5 to 3 were prepared using phosphate buffers as phosphates have pK_{a1} at 2.15. In pH ranges between pH 3 to 5, we used citrate buffers with the pK_a of 3.14. In order to compare the effect of buffers, citrate and phosphate buffer at pH 2.5 were used for low pH, and acetate (pK_a = 4.76) and citrate buffers at pH 5 were used for testing at high pH.

A concentration of 4 mM buffer at various pHs were added to the growth solution in our experiments. This concentration was chosen as the Au prisms stabilized by 4 μM of T30 DNA

strands would show signs of aggregation when salt concentration was above 4 mM. Despite the low concentration of buffer, the amount of buffer in solution were still more than the concentration of other components ([HA] = 2 mM, [DNA] = 4 μM, [$HAuCl_4$] = 0.51 mM). The buffer conditions tested were shown below in the Table 4.1.

The growth of nanoparticles in the presence of these buffering components were tested for all four bases shown in Figure 4.2, 3, 4 and 5. For T30, the six-point stars were well formed in the presence of buffers with pHs below 3 (Figure 4.2b-d). Starting from buffers of pH 3, the growth starts to become less controlled and the six-pointed stars look overgrown. Growth with buffers of pH of 4.5 and 5.0, we observed the formation of large spiky structures (Figure 4.2e-i). For G20, the growth were rather controlled for the buffer condition with pH below 4 forming hexagon plates (Figure 4.3c-f). At pH of 1.5 and 2 buffers, however, the particles were observed to be more round with edge truncation of the hexagon shape (Figure 4.3b). For growth with buffers of pH 4, 4.5 and 5, large rough aggregates and spiky flower like particles were observed. When buffers were used for C30, the nanoparticles formed were observed to be rougher than without buffer. The rough round particles were formed for buffers with pH ranges between 1.5 -3. Larger rough structures were observed for buffers at pH 3.5 and 4 while large spiky structures were observed in the presence of buffers of pH 4.5 and 5. The growth of A30 to form rough round structures were consistent between buffers of pH 1.5 to 3.5. Beyond that pH, rough aggregates were formed at pH 4 buffer and large spiky particles were observed for buffers of pH 4.5 -5.

Due to the low concentration of buffer used, the pH of the reaction is slightly different from the pH of the buffer. The true pH of the reactions for each buffers are shown in Figure 4.6. Summarizing the data from all 4 of the bases, we observed that the optimal pH at which DNA mediated growth was the best between pH 2.5 to 3. The reaction pH cut off where the particles no

longer grow well was around pH 3.8 (Figure 4.6). Large aggregates and huge spiky flower structures were observed for reaction pHs above 3.8 regardless of what bases were used. The presence of an optimal growth window and a sharp cut where the nanoparticles no longer grow well indicates that the control of pH of this reaction is important.

The effect of different buffer components

Since the pH that we tested were using two different buffer sets, citrate and phosphate, it is important determine whether the growth is caused by the change in pH or the change in buffer components. We tested the growth using both buffer component with the same pH. Since the buffering region of both phosphate ($pK_a = 2.15$) and citrate ($pK_a = 3.14$) overlaps, we chose to test the growth with addition of both buffer solutions at pH 2.5. By monitoring the growth using the two buffers with T30, both buffers resulted in the formation of six-pointed stars. Our results indicate that the growth was independent of the buffer component (Figure 4.7). To further reaffirm that our observation is pH controlled rather than the buffer component, we also tested the growth at pH 5 for two different buffers, citrate and acetate. Both of the buffer resulted in formation of spiky particles when grown in the presence of T30 (Figure 4.7). These results clearly demonstrate that the addition of 4 mM buffer influences the growth through changing the reaction pH and not due to the change in buffer components.

PH profile of the growth in the presence of buffer.

While it is noted that different pH of the buffer would affect the growth of the nanoparticles, it is unclear how the pH change influences the reactions. To get a better understanding of the reaction progression at different pH, we monitored the pH changes of the reaction with time in the

presence of various buffer components. Since the concentration of the buffer used is not very high at 4 mM, the reaction pH will be influenced but the reaction will only be slightly buffered.

The pH profile for the growth with T30 was monitored (Figure 4.8). In general for low pH buffers, as the reaction proceeds, we observed a plateau or an induction period prior to a sudden drop in pH. After the pH drop, the pH continues to stabilize suggesting completion of the reaction. The rate of proton generation corresponds to the rate at which the HA oxidizes to generate H^+ and the rate of reduction of the precursor. The pH drop occurred at a faster time when buffers with increasing pH were used. This corresponds to an increase in the rate of the reaction for higher reaction pHs. For reactions at pH 2.5, the pH profile seems to best match with the pH profile in the absence of the buffer consistent with our observation of growth into six-pointed stars at pH 2.5. At higher buffer pHs, the pH decreased rapidly and the final pHs of the solutions were observed to be higher than the reaction pH in the absence of buffer. This observation may provide insight to understand the contributing factor of the change in growth since the particles formed at these pHs formed into large aggregates or form large spiky particles.

Effect of buffer concentration

To clearly understand if the pH or the change in pH is the factor that influence the growth, we increased the buffer of the reaction to 50 mM so that the pH of the reaction solution remains consistent throughout the reaction. Unfortunately at high salt concentration, the nanoparticles incubated with the weak binding DNA, T30, was not stable and aggregated before the growth occurs. Hence the study of the growth at various pH values were performed using A30, whose strong binding affinity to gold allows the particle to be stabilized (Figure 4.9)

At 50 mM buffer concentrations, the nanoparticles under pH 3.5 grew rather homogenously (Figure 4.9). The final shape and morphology of the nanoparticles were found to have a larger diameter and lesser roughness at pH below 3.0 compared to the growth at low buffer concentrations. At pH 3.0, the nanoparticles were rough and round similar to the growth without buffer but rougher. At pH above the 3.0, the nanoparticles were very rough and formed irregular shapes. These observations are interesting as it indicates an optimal pH for the reaction to occur. If we compare the reaction pH to the range of pH tested at 4 mM, we find that A30 grew in the range of pH between 2.4 to 3.6. The lower bound of the pH was not tested at 4 mM as pH 1.5 was the lowest buffering pH for phosphate. The pH 3.0 is exactly in the middle of the range of reaction pHs. The reaction at 50 mM indicates that the rate at pH 2.5, which close to the lower pH reaction range, is probably too slow; while the pH 3.5, which is close to the upper limit, is too fast for the reaction.

Discussions

From our experiments, it is clear that the pH of the growth solution greatly affects the growth of the nanoparticle. Under pH 3, most of the nanoparticles grew well into the shape and morphology similar to the case when there is no buffer. The nanoparticle growth is rather sensitive to this value in which above that pH, all the growth starts to deviate from DNA sequence dependent growth. It is important to identify the key player in this reaction that controls the formation of the nanoparticle. There are several factors that may affect the growth of nanoparticles as the pH changes: (1) protonation state of the DNA, (2) speciation of gold under various pH conditions, (3) speciation of hydroxylamine and its reduction potential at various pH conditions.

First we look into the effect of protonation state of the DNA bases. The relevant pK_a of the bases in the range of the reaction are shown in Figure 4.10. Most of the bases have its pKa out of

the range of the reaction, with the exception of protonation of adenine which has a pKa of 3.5. First pK_a of guanine is low at 2.1, while cytosine with pK_a of 4.2, thymine with pK_a 9.2 and deprotonation of guanine with a second pK_a value of 9.9 are beyond the range of pH effects observed here. The pK_a of each of the bases which are diverse, unlike the narrow range observed for controlled growth of nanoparticles which is between 2.4 to 3.7 (Figure 4.6). This suggest that the reaction has little correlation with the pK_a of the bases.

Next we investigated the possible speciation of gold which may affect the reaction. The speciation of metals ions are known to affect the reduction potential of the metal complex.[26,36,37] $HAuCl_4$ in water can undergo ligand substitution where the chloride ligands substituted by with hydroxyl groups. Monosubstituted species $[AuCl_3(OH)]^-$, disubstituted $[AuCl_2(OH)_2]^-$ and trisubstituted $[AuCl(OH)_3]^-$ can form depending on the pH of the solution.[38-40] In the absence of excess chloride ions, the gold chloride solution of 0.5 mM was determined to consist mainly of $[AuCl_3(OH)]^-$ between pH 2 and 3 using Raman spectroscopy measurements.[39] In our reaction conditions, the pH of the solution is typically around pH 3 which meant that the $[AuCl_3(OH)]^-$ species the predominant reactive species in our reaction.

The reduction potential of gold chloride is influenced by the ligands on the gold complex. At pH 2.91, the reduction potential is 0.66 V while pH 6.16 and 8.01 result in reduction potential of 0.59 V and 0.53 V. [26] The reduction of $HAuCl_4$ at high pH is more difficult than that at low pH.[26] Therefore the reduction of $[AuCl_4]^-$ and $[AuCl_3(OH)]^-$ results in fast nucleation and more homogenous nanoparticles while the more hydroxylated species will have slow nucleation resulting in large size distribution.[41] In our reaction, the pH of the reaction drops as the reaction progresses. Hence there will be an increase in the $[AuCl_4]^-$ species and subsequent increase in reaction rate. However, our results suggest that the reactions are faster and less controllable at pH

above 3.8, and slower at lower pHs. This observation is not consistent with the speciation of the gold precursor where a faster reaction should be observed at lower pH for $[AuCl_4]^-$ than the hydroxyl substituted complex at higher pHs. This suggest that the speciation of gold is not the main factor that determines the growth.

The final factor is the pH effect on the reductant hydroxylamine. Simic and Hayon investigated the one electron oxidation of hydroxylamine using hydroxyl radicals. The rate of the reaction with protonated form of hydroxylamine is slower at $k \leq 5.0 \times 10^8$ $M^{-1}s^{-1}$ while the rates with the unprotonated form is much faster at $k = 9.5 \times 10^9$ $M^{-1}s^{-1}$.[42] Hence at different pH the reaction rates would vary depending on the species of unprotonated hydroxylamine. The hydroxylamine is reported to have a pK_a of 5.97 which we expect to be well beyond the range of pH in our reaction. However, using stopped-flow, the reaction rates of hydroxylamine with iodine has been reported to be 0.851 ± 0.008 s^{-1} at pH 3.44 while the reaction rates increased nearly 10 fold to 8.22 ± 0.11 s^{-1} with increase of pH to 4.00 which is only a 0.55 pH difference. This rapid increase in reaction rates with pH would explain our observation where the growth becomes less controllable at sharp pH cut off value 3.8.

The increase in reaction rates with pH also explains the formation of spiky nanoflowers regardless of the DNA ligand present. This observation is consistent with a fast reduction and diffusion limited reaction which forms dendrite structures.[43] Hence, preferential attachment of gold on sites that would lower the overall surface energy or gold deposition guided by DNA is not observed at higher pHs. For reactions to be controlled and mediated by DNA, the rate of reduction and pH has to be lowered. When reactions with 50 mM buffer was used, we can clearly observe the effect of the reduction rates on the shape of the particle. A balance of reduction rate is required for optimal growth. Our results clearly suggest that minor changes in the reaction pH can greatly

influence the growth of the nanoparticles mediated by DNA. By identifying the key contributor that is affected by pH, we can better control the growth by tuning the reaction conditions.

4.3 Conclusions

We have investigated the effect of change in pH in the reaction of DNA mediated shape control of nanoparticles by adding small amounts of buffers at various pHs from 1.5 to 5 into the growth solution. The DNA mediated growth reaction was found to be highly pH dependent where all of the bases grew well for buffer pH below 3 or 3.5. A sharp cut off was observed where addition of buffers beyond pH 3.5 resulted in the growth of irregular and spiky structures. The growth was found to be independent of the buffer component, indicating that the pH is the main contributing factor for controllable growth. The range of the pH of reactions were between 2.4 and 5.2. This range is small but significant changes to the final shape of the particles were observed. The key in the pH mediated control was the rapid change in reduction rate of hydroxylamine with only slight pH changes. At low pH, the rate is slower which allows the DNA dependent deposition while at high pH, the reaction rates are fast and diffusion controlled. These experiments suggest that the control of pH is very important to allow ligand mediated synthesis as minor changes to pH can significantly affect the growth of the nanoparticle.

4.4 Experimental Section

Materials. All oligodeoxyribonucleotides were purchased from Integrated DNA Technologies (Coralville, IA). Hydrogen tetrachloroaurate (III) hydrate, hydroxylamine hydrochloride, sodium hydroxide, cetyltrimethlyammonium bromide (≥99%), sodium iodide, L-ascorbic acid and sodium borohydride were purchased from Sigma-Aldrich. Sodium citrate

anhydrous was purchased from Alfa Aesar. Phosphoric acid was purchased from Fisher Scientific Co.

Synthesis and purification of gold nanoprisms. Gold nanoprisms were prepared by following previously published procedures. The as-prepared nanoprism solution was stored in a glass flask overnight to allow the nanoprisms to settle. Afterwards, the supernatant was removed and the gold nanoprisms were redispersed in Millipore water (6-7 mL).

Synthesis of the gold nanoparticles mediated by DNA. The freshly redispersed gold nanoprism solution was purified by centrifugation twice. Its absorbance at 800 nm was then measured by UV-vis spectrometry, and adjusted to 0.7 with appropriate dilutions. 100 µL of this solution was incubated with either 4 µM of T30 or 2 µM of other DNA sequences for 15 min to allow the DNA to adsorb onto the gold nanoseeds. 1 µL of 200 mM NH_2OH (adjusted to pH 5 with NaOH) was then added and the solution was vortexed. 2.5 µL 0.8 % (wt/wt) $HAuCl_4$ was then introduced to initiate the reduction reaction. A color change was observed in a few minutes, and the reaction was allowed to progress at least 30 minutes. For reactions in the presence of buffer, 2 µL of 200 mM of the various buffer components were added to the reaction mixture after the DNA incubation step but prior to addition of reductant and precursor. The reaction solutions were centrifuged three time to remove excess salt and reactants and the nanoparticles formed were characterized using SEM.

Equipment and Characterizations

The particles synthesized were characterized using Hitachi S4800 SEM with 10 kV and 10 µA. Nanoparticle concentrations were characterized by the absorbance at 800 nm using UV-Vis

spectrophotometry (Hewlett–Packard 8453). Accumet AB15 pH meter and microprobe electrode were used for all pH measurements.

4.5 References

(1) Zhao, P.; Li, N.; Astruc, D. *Coord. Chem. Rev.* **2013**, *257*, 638.

(2) Lu, Z.; Yin, Y. *Chem. Soc. Rev.* **2012**, *41*, 6874.

(3) Grzelczak, M.; Perez-Juste, J.; Mulvaney, P.; Liz-Marzan, L. M. *Chem. Soc. Rev.* **2008**, *37*, 1783.

(4) Pelaz, B.; Jaber, S.; de Aberasturi, D. J.; Wulf, V.; Aida, T.; de la Fuente, J. M.; Feldmann, J.; Gaub, H. E.; Josephson, L.; Kagan, C. R.; Kotov, N. A.; Liz-Marzán, L. M.; Mattoussi, H.; Mulvaney, P.; Murray, C. B.; Rogach, A. L.; Weiss, P. S.; Willner, I.; Parak, W. J. *ACS Nano* **2012**, *6*, 8468.

(5) Sau, T. K.; Murphy, C. J. *J. Am. Chem. Soc.* **2004**, *126*, 8648.

(6) Personick, M. L.; Mirkin, C. A. *J. Am. Chem. Soc.* **2013**, *135*, 18238.

(7) Liao, H.-G.; Niu, K.; Zheng, H. *Chem. Commun.* **2013**, *49*, 11720.

(8) Xia, Y.; Xiong, Y.; Lim, B.; Skrabalak, S. E. *Angew. Chem. Int. Ed.* **2009**, *48*, 60.

(9) Turkevich, J.; Stevenson, P. C.; Hillier, J. *J. Phys. Chem.* **1953**, *57*, 670.

(10) Ji, X.; Song, X.; Li, J.; Bai, Y.; Yang, W.; Peng, X. *J. Am. Chem. Soc.* **2007**, *129*, 13939.

(11) Bastús, N. G.; Comenge, J.; Puntes, V. *Langmuir* **2011**, *27*, 11098.

(12) Shou, Q.; Guo, C.; Yang, L.; Jia, L.; Liu, C.; Liu, H. *J. Colloid Interface Sci.* **2011**, *363*, 481.

(13) Zhang, J.; Langille, M. R.; Mirkin, C. A. *J. Am. Chem. Soc.* **2010**, *132*, 12502.

(14) Sirajuddin; Mechler, A.; Torriero, A. A. J.; Nafady, A.; Lee, C.-Y.; Bond, A. M.; O'Mullane, A. P.; Bhargava, S. K. *Colloids Surf. A Physicochem. Eng. Asp.* **2010**, *370*, 35.

(15) Young, J.; Lewinski, N.; Langsner, R.; Kennedy, L.; Satyanarayan, A.; Nammalvar, V.; Lin, A.; Drezek, R. *Nanoscale Res. Lett.* **2011**, *6*, 428.

(16) Straney, P. J.; Marbella, L. E.; Andolina, C. M.; Nuhfer, N. T.; Millstone, J. E. *J. Am. Chem. Soc.* **2014**, *136*, 7873.

(17) Shahzad, A.; Kim, W.-S.; Yu, T. *RSC Adv.* **2015**, *5*, 28652.

(18) Gilroy, K. D.; Hughes, R. A.; Neretina, S. *J. Am. Chem. Soc.* **2014**, *136*, 15337.

(19) DeSantis, C. J.; Peverly, A. A.; Peters, D. G.; Skrabalak, S. E. *Nano Lett.* **2011**, *11*, 2164.

(20) Bower, M. M.; DeSantis, C. J.; Skrabalak, S. E. *J. Phys. Chem. C* **2014**, *118*, 18762.

(21) Ritchie, C. M.; Johnsen, K. R.; Kiser, J. R.; Antoku, Y.; Dickson, R. M.; Petty, J. T. *J. Phys. Chem. C Nanomater. Interfaces* **2007**, *111*, 175.

(22) Kennedy, T. A. C.; MacLean, J. L.; Liu, J. *Chem. Commun.* **2012**, *48*, 6845.

(23) Lee, K.-J.; Lee, Y.-I.; Lee, J.; Myung, N. V.; Choa, Y.-H. *Curr. Appl. Phys.* **2012**, *12*, *Supplement 2*, S53.

(24) Yu, Y.; Zhang, Q.; Xie, J.; Lee, J. Y. *Nat. Commun.* **2013**, *4*, 1454.

(25) Zhang, J.; Feng, C.; Deng, Y.; Liu, L.; Wu, Y.; Shen, B.; Zhong, C.; Hu, W. *Chem. Mater.* **2014**, *26*, 1213.

(26) Wang, S.; Qian, K.; Bi, X.; Huang, W. *J. Phys. Chem. C* **2009**, *113*, 6505.

(27) Yagi, S.; Oeda, N.; Kojima, C. *J. Electrochem. Soc.* **2012**, *159*, H668.

(28) Sun, D.; Gang, O. *Langmuir* **2013**, *29*, 7038.

(29) Berti, L.; Burley, G. A. *Nature Nanotech.* **2008**, *3*, 81.

(30) Wang, Z.; Tang, L.; Tan, L. H.; Li, J.; Lu, Y. *Angew. Chem. Int. Ed.* **2012**, *51*, 9078.

(31) Wang, Z.; Zhang, J.; Ekman, J. M.; Kenis, P. J. A.; Lu, Y. *Nano Lett.* **2010**, *10*, 1886.

(32) Wu, J.; Tan, L. H.; Hwang, K.; Xing, H.; Wu, P.; Li, W.; Lu, Y. *J. Am. Chem. Soc.* **2014**, *136*, 15195.

(33) Bengtsson, G.; Fronaeus, S.; Bengtsson-Kloo, L. *J. Chem. Soc., Dalton Trans.* **2002**, 2548.

(34) Li, J.; Lin, X. *Sens. Actuators B Chem.* **2007**, *126*, 527.

(35) Kannan, P.; John, S. A. *Anal. Chim. Acta* **2010**, *663*, 158.

(36) Hubbard, A. T.; Anson, F. C. *Anal. Chem.* **1966**, *38*, 1887.

(37) Kohl, P. A. In *Modern Electroplating*; John Wiley & Sons, Inc.: 2010, p 115.

(38) Moreau, F.; Bond, G. C.; Taylor, A. O. *J. Catal.* **2005**, *231*, 105.

(39) Murphy, P. J.; LaGrange, M. S. *Geochim. Cosmochim. Acta* **1998**, *62*, 3515.

(40) Usher, A.; McPhail, D. C.; Brugger, J. *Geochim. Cosmochim. Acta* **2009**, *73*, 3359.

(41) Burke, L. D.; Nugent, P. F. *Gold Bull.* **1997**, *30*, 43.

(42) Simic, M.; Hayon, E. *J. Am. Chem. Soc.* **1971**, *93*, 5982.

(43) Wang, Z.; Bharathi, M. S.; Hariharaputran, R.; Xing, H.; Tang, L.; Li, J.; Zhang, Y.-W.; Lu, Y. *ACS Nano* **2013**, *7*, 2258.

4.6 Figures

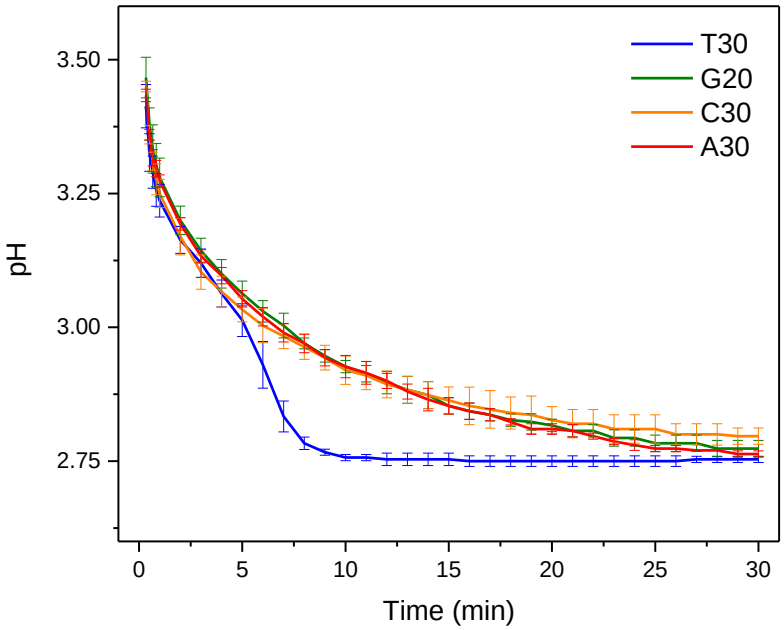

Figure 4.1. pH profile of the reaction in the presence of different DNA bases A30, G20, C30 and T30 upon addition of reductant hydroxylamine and $HAuCl_4$.

Table 4.1. Buffer components used in this study ranging from pH 1.5 to pH 5.

Labels	Buffer pH	Buffer component	pH at 4 mM
a	No buffer	-	-
b	1.5	Phosphate	2.70
c	2.0	Phosphate	2.97
d	2.5	Phosphate	3.35
e	3.0	Citrate	3.51
f	3.5	Citrate	3.97
g	4.0	Citrate	4.54
h	4.5	Citrate	5.09
i	5.0	Citrate	5.66

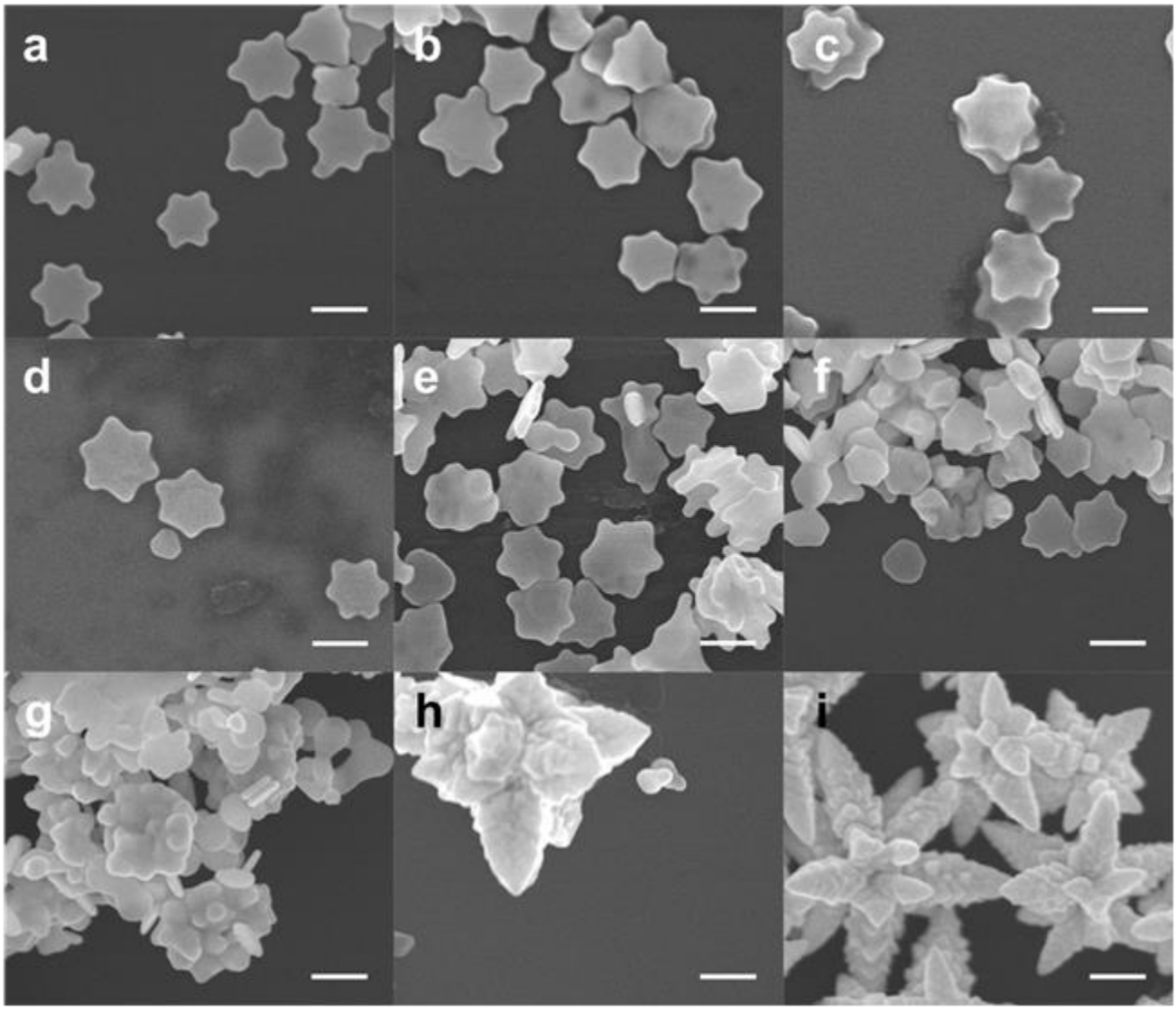

Figure 4.2. SEM images of the nanoprism grown with T30 in the presence of various buffer conditions with different pH mentioned in Table 4.1. The concentration of buffer when used is 4 mM. The scale bars are 200 μm.

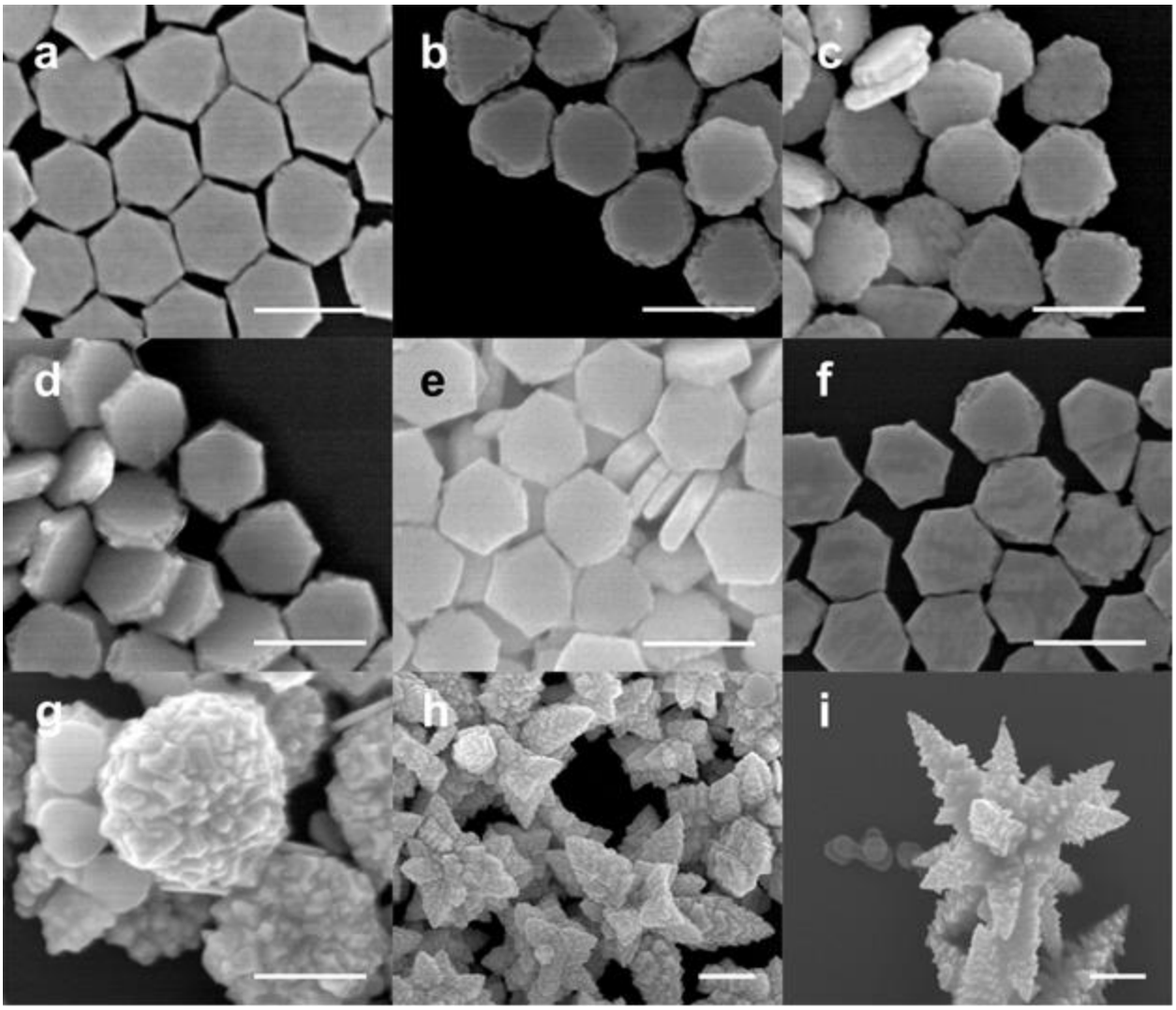

Figure 4.3. SEM images of the nanoprism grown with G20 in the presence of various buffer conditions with different pH mentioned in Table 4.1. The concentration of buffer when used is 4 mM. The scale bars are 200 μm.

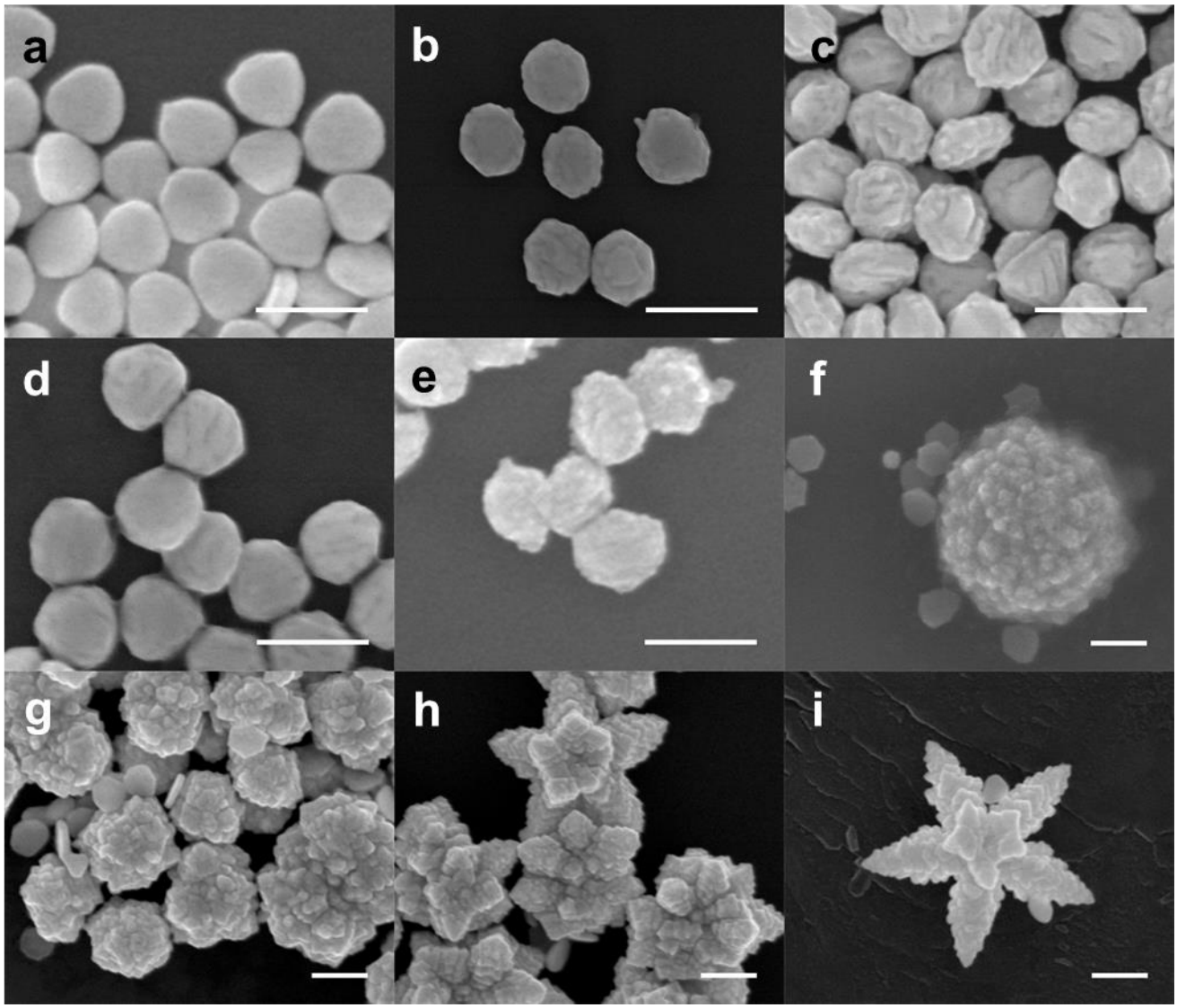

Figure 4.4. SEM images of the nanoprism grown with C30 in the presence of various buffer conditions with different pH mentioned in Table 4.1. The concentration of buffer when used is 4 mM. The scale bars are 200 μm.

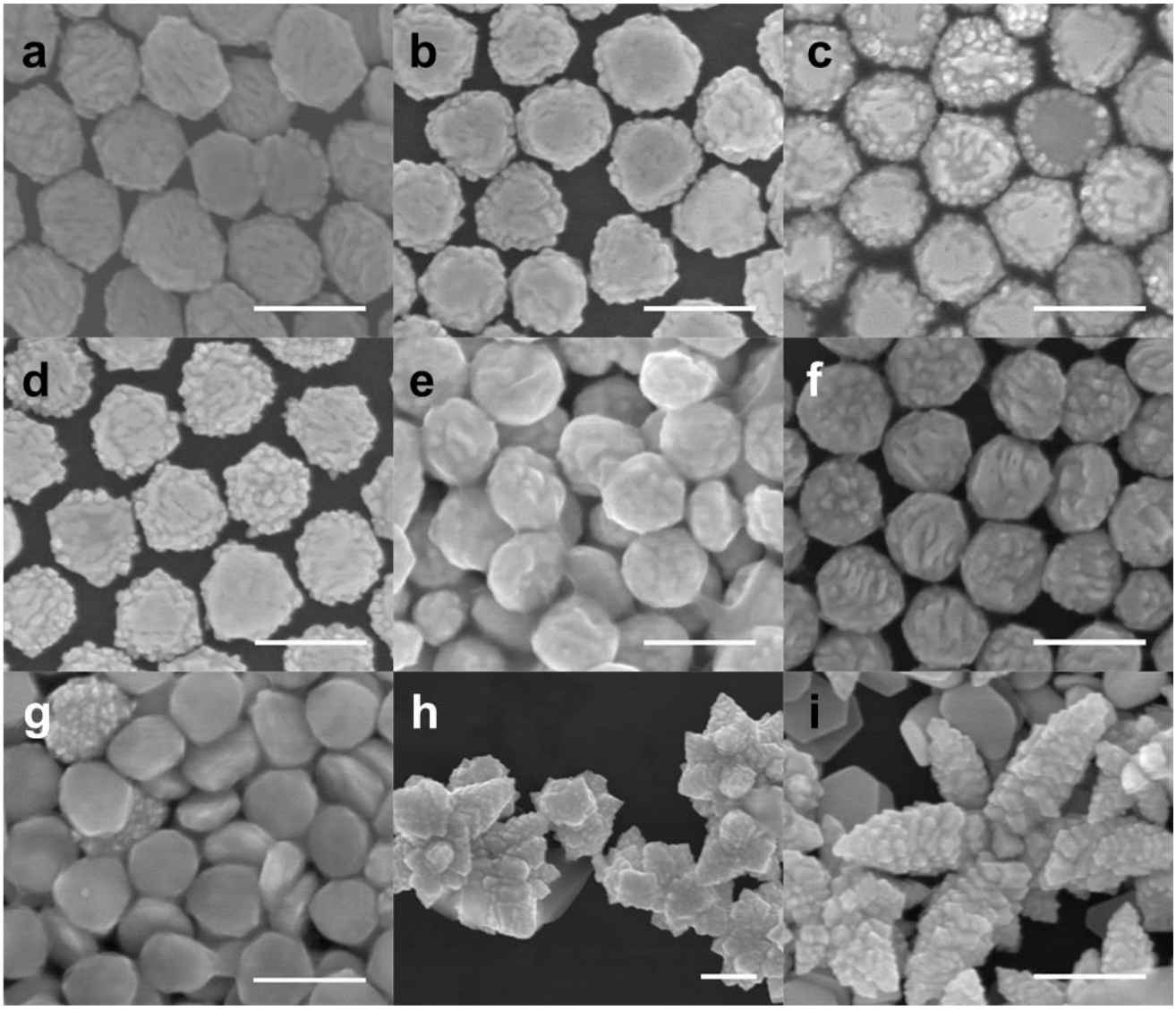

Figure 4.5. SEM images of the nanoprism grown with A30 in the presence of various buffer conditions with different pH mentioned in Table 4.1. The concentration of buffer when used is 4 mM. The scale bars are 200 μm.

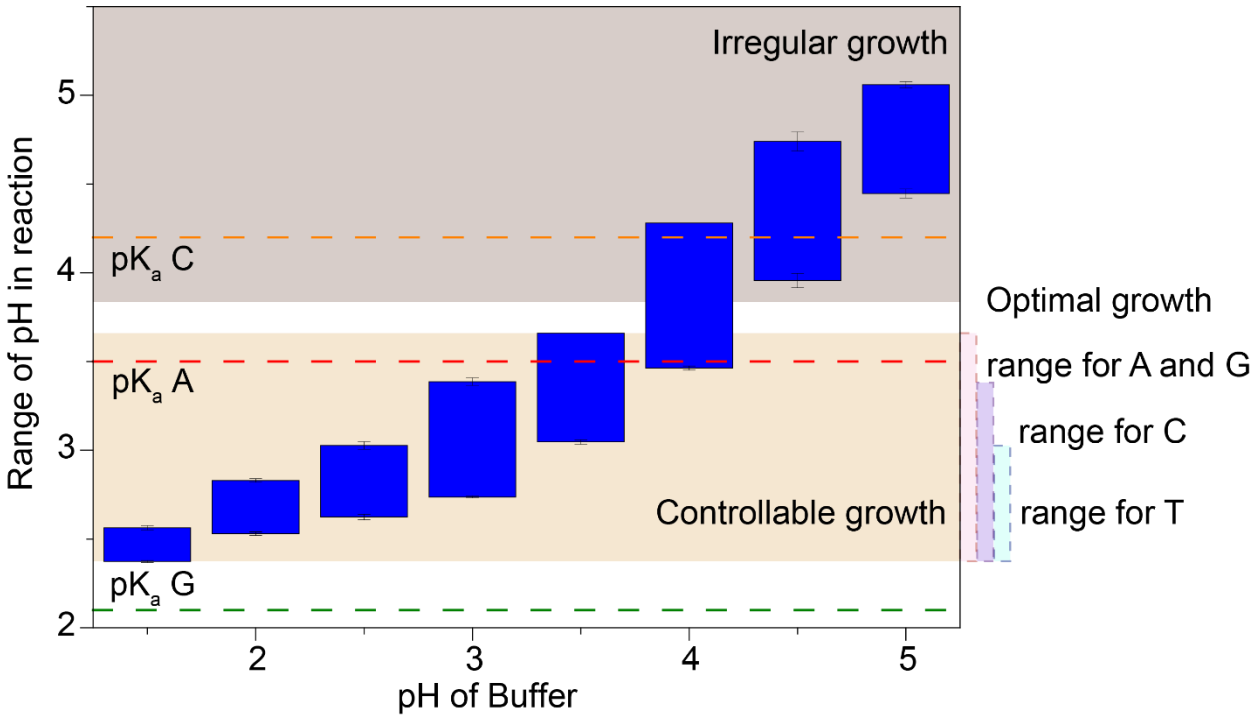

Figure 4.6. The range of pH observed at initial time points and final time points for the reactions when 4 mM buffer of various pHs were added. The relevant pK_a of bases are indicated in the graph as well as the range of pH were the growth was observed to be controllable for the different bases.

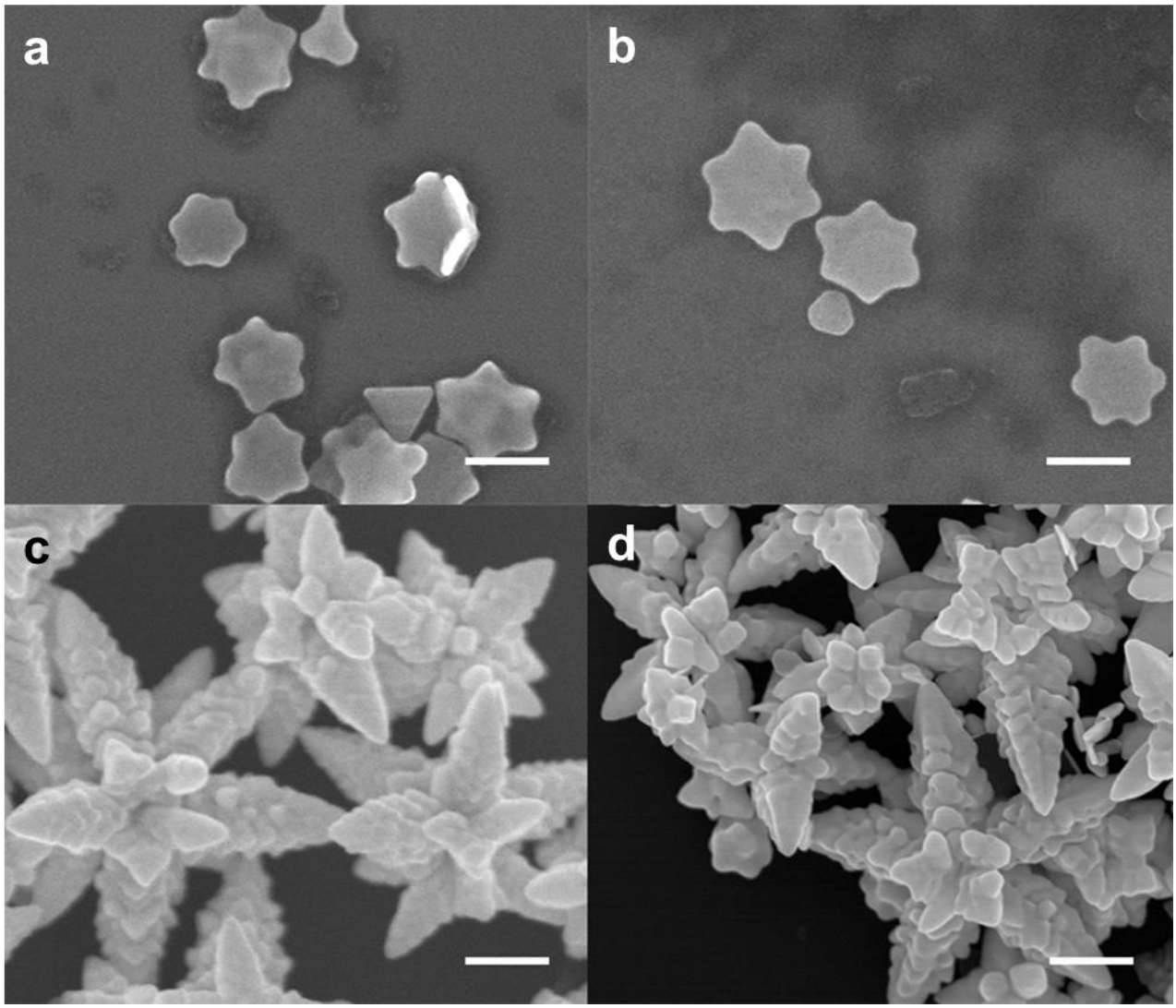

Figure 4.7. SEM images of the nanoprism grown with T30 in the presence of (a) phosphate buffer pH 2.5, (b) citrate buffer pH 2.5, (c) citrate buffer pH 5.0 and (d) acetate buffer pH 5.0. All buffer components were used at 4 mM concentration. The scale bars are 200 μm.

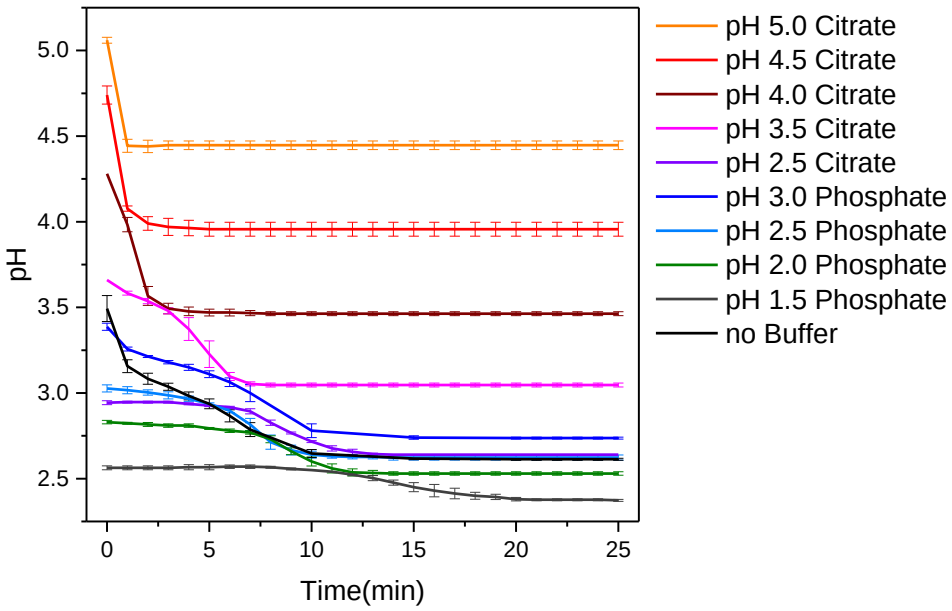

Figure 4.8. PH profile of the reaction mixture grown with 4 µM T30, 2 mM HA, 0.5 mM HAuCl4 and 4 mM of various buffers from pH 1.5 to 5.0.

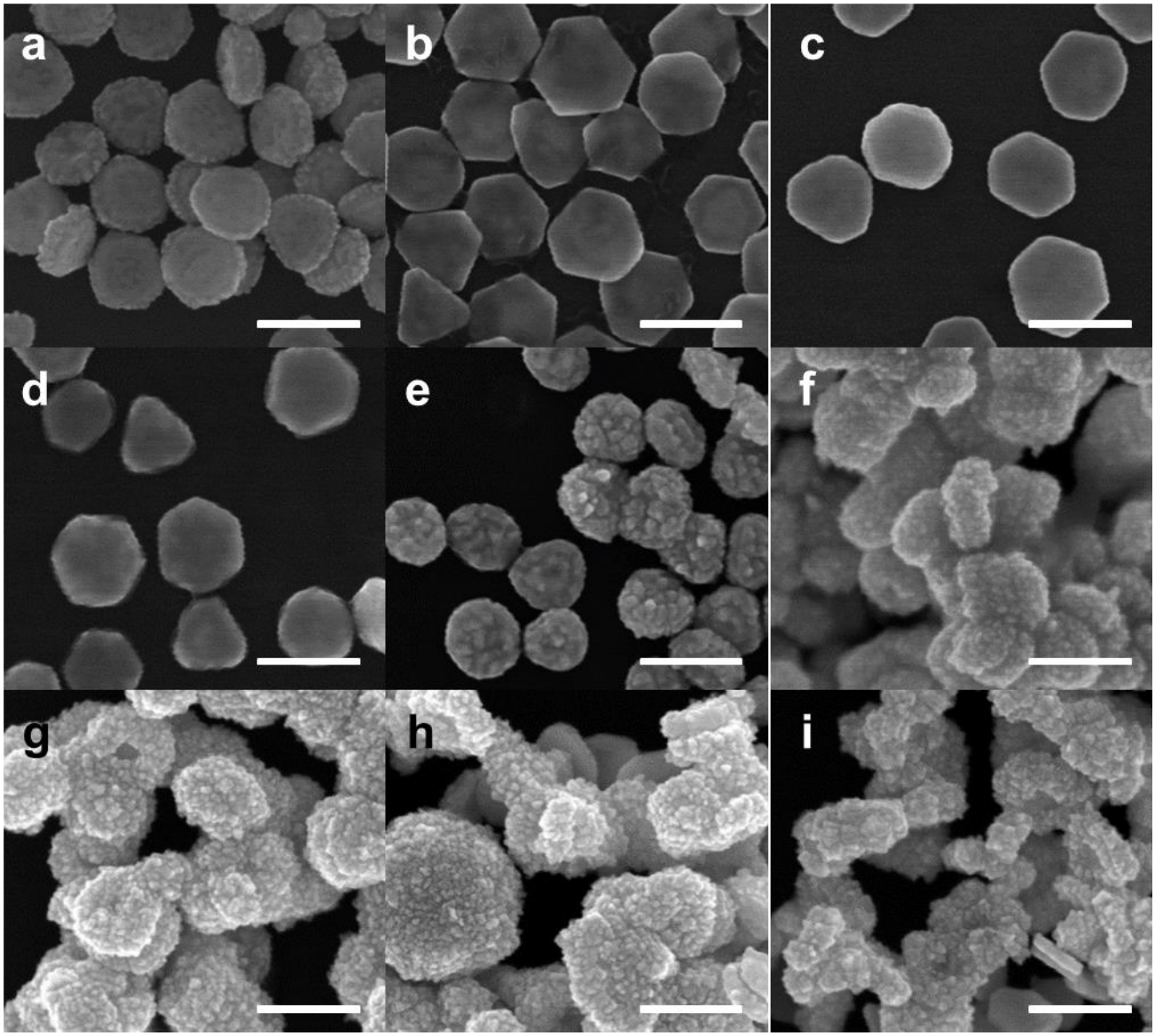

Figure 4.9. SEM images of the nanoprism grown with A30 in the presence of various buffer conditions with different pH mentioned in Table 4.1. The concentration of buffer when used is 50 mM. The scale bars are 200 μm.

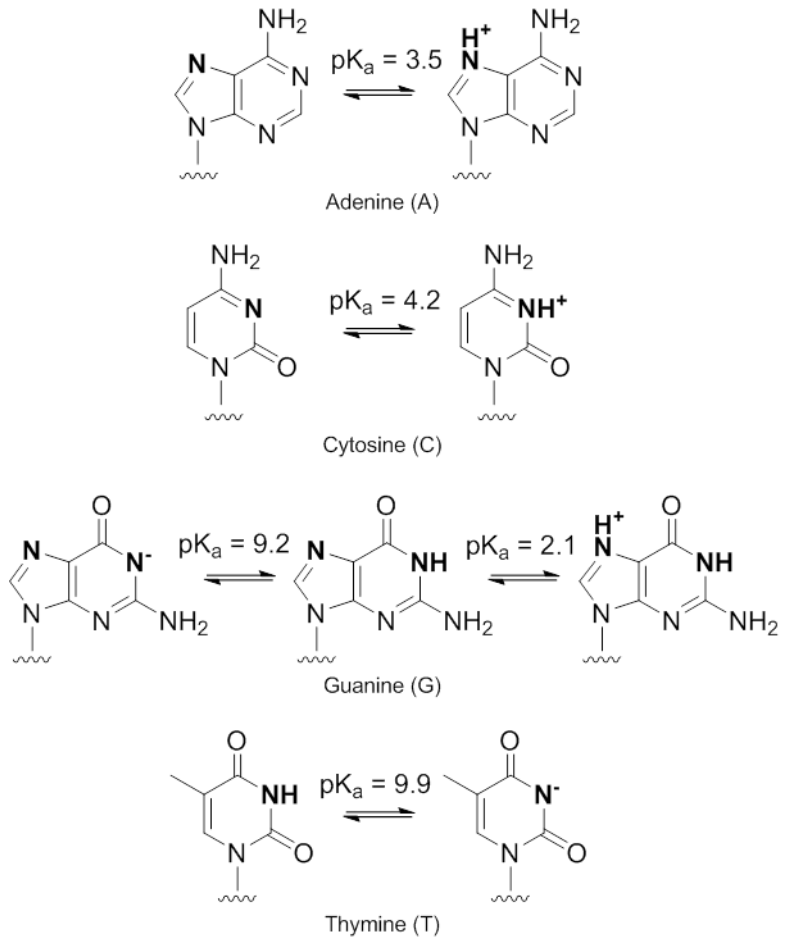

Figure 4.10. Different protonation and deprotonated states of the DNA bases and their corresponding pK_a values.

CHAPTER 5

FACILE AND EFFICIENT PREPARATION OF ANISOTROPIC DNA-FUNCTIONALIZED GOLD NANOPARTICLES AND THEIR REGIOSELECTIVE ASSEMBLY

Part of this chapter was published in "Facile and Efficient Preparation of Anisotropic DNA-Functionalized Gold Nanoparticles and Their Regioselective Assembly" Tan, L. H.; Xing, H.; Chen, H.; Lu, Y. *Journal of the American Chemical Society* **2013**, *135*, 17675.

5.1 Introduction

DNA-functionalized gold nanoparticles (DNA-AuNPs) are among the most useful building blocks for nanoscale assembly. They have been used to form wide variety of structures from discrete clusters[1-3] to one dimensional chains,[4-6] two dimensional assemblies consisting of regular and periodic sheets of AuNP,[7-10] and to three dimensional superlattices.[11-14] The programmable nature of the DNA strands allows tuning and engineering of a variety of superlattices not achievable by conventional methods and introduces functionality to the particles.[15-21] Most DNA-AuNPs used in assembly, however, are isotropic ones with DNA molecules distributed evenly around the AuNP surface. While a number of nanoscale assembly has been reported using these isotropic nanoparticles, it is desirable to explore the use of anisotropic nanoparticles in the assembly, as the unique directionality in interaction provided by anisotropically shaped or functionalized particles such as Janus particles or patchy particles, can result in complex structures with novel properties which are not achievable by using isotropic nanoparticles.[22-25] As a result, Janus or anisotropic particles are attracting huge amount of interest, as these particles, which

contain spatially separated functionalities, are capable of directing the orientation of particle interactions.[26-29] These particles have been demonstrated to form novel lattices, discrete and chiral assemblies with unique ensemble properties.[30-35] Despite being promising building blocks for self-assembly, DNA-conjugated anisotropic particles are challenging to synthesize,[36-39] with only few efficient methods.[40-44] Most synthesis methods require careful surface-based fabrication, long incubation time, or have low yields that require additional step of purification.[30,31,45-48] Furthermore, the prepared anisotropic nanoparticles are often difficult to functionalize selectively.[49] Here, we report a facile method to synthesize DNA-functionalized anisotropic nanoparticles with high yields, and subsequently functionalized with DNA for chemoselective and regioselective assembly of a variety of AuNPs. We further demonstrate that this particle could be used to regioselectively functionalize two different DNA strands on the same particle.

5. 2 Results and Discussions

The anisotropic AuNP (a-AuNP) was formed based on competition between hydrophobic and hydrophilic ligands on gold nanoparticle surface to produce anisotropic attachment of polymers, as reported by Chen *et al.*[49,50] This method allows facile synthesis of a-AuNP in high yield. However, the a-AuNP have not been applied for anisotropic functionalization due to the low efficiency for post-modification nor applied for selective assembly due to the limited functional groups that can be used for synthesis of these anisotropic AuNP. To overcome this limitation, we used a 10-mer oligo of adenine with thiol at the 5′ end (HS-A10) as the hydrophilic ligand and a thiolated phospholipid (PSH) as the hydrophobic ligand (shown in Figure 5.1a). Both ligands were incubated with either 15 nm or 20 nm AuNP and an amphiphilic polymer polystyrene-b-poly(acrylic acid) (PSPAA) in DMF/H_2O at 95 °C for two hours and the mixtures were then cooled

to room temperature. Transmission electron microscope (TEM) images of the samples synthesized with 15 nm (Figure 5.1b, large-area-view in Figure 5.2a) or 20 nm AuNPs (Figure 5.1c and Figure 5.2b) indicates that a-DNA-AuNPs were formed uniformly throughout, suggesting that this method can be applied for synthesis of a-DNA-AuNPs of different sizes. To quantify the synthesis yield, we counted a total of 633 particles from the TEM micrographs and found ~96% of 20 nm a-DNA-AuNPs, with the remaining 4% either having no polymer attachment, full polymer encapsulation or encapsulated dimer of particles.

Since DNA molecules are negatively charged, the ratio of DNA to PSH can be tuned to balance the competition between the two ligands. As shown in Figure 5.3a, a PSH to DNA ratio of 2 gave a larger polymer but still uniform coverage on the AuNP, while a PSH to DNA ratio of 1 resulted in a mixture of unencapsulated particles and partial encapsulated particles (Figure 5.3b). A ligand ratio of 1:2.8 and 1:1.5 was found to be optimal for 15 nm and 20 nm a-DNA-AuNPs, respectively. Control experiments performed using only DNA or only PSH as the ligand resulted in unencapsulated AuNP (Figure 5.1d) and the AuNP fully encapsulated with PSPAA (Figure 5.1e), respectively. These results support the roles of DNA as hydrophilic ligand and PSH as hydrophobic ligand. The areas on the AuNP not encapsulated by polymer are covered by DNA.

To investigate whether this method can be generally applied to DNA strands with different sequences, thiolated A10, A30 and R20 (full sequence available in SI) were used to repeat the above procedures and all of them produced anisotropic structures, as long as proper PSH to DNA ligand ratios of 1.5, 2.2 and 5.6 are maintained respectively (Figure 5.2b, 3c and 3d). These results suggest that DNA sequences only have minimal effects on the formation of anisotropic structure. Instead, the ligand ratio is critical, especially to produce uniform anisotropic encapsulation of AuNP.

Localized surface plasmon resonance (LSPR) spectra of AuNPs are strongly correlated to the structure of the AuNP and its monodispersity. From the UV-vis absorbance spectra of the a-DNA-AuNPs, we observed a clear peak at 535 nm, which is slightly red-shifted from the absorbance peak of citrate capped AuNPs (Figure 5.1f). The peak width was retained and there were no additional peak or shoulder peak suggesting that the AuNPs are well dispersed and individually modified with polymer after synthesis. This result is consistent with the TEM micrographs in Figure 5.1c. The slight red-shift of the plasmon resonance of the synthesized a-DNA-AuNP is expected due to the functionalization of the AuNP with a ligand shell.

Upon demonstrating the one-pot synthesis of these a-DNA-AuNPs, we next investigated selective ligand exchange on the a-DNA-AuNPs to introduce any desired functionality for further applications of these particles. The functionalization should be regioselective so that only specific locations of the anisotropic particle are functionalized. The ligand exchange on gold surfaces, which occurs via an associative mechanism, is known to be very inefficient at room temperatures, depending on several factors such as the steric bulk and length of the incoming and existing ligands.[51,52] To achieve this goal, we adopted a quick functionalization method reported by Zhang *et al.*[53] where thiolated DNA (D1) was incubated with a-DNA-AuNP in 50 mM of pH 3 Na-Citrate solution to give a-(D1)-AuNP (Figure 5.4a). The UV-vis absorption spectra of a-DNA-AuNP before and after functionalization with D1 were nearly identical indicating that the functionalization process did not disrupt the integrity of the a-DNA-AuNP particle or cause it to aggregate (Figure 5.5). The DNA attachment was confirmed by functionalizing the a-DNA-AuNP with fluorescein (FAM) labeled DNA at 5′ end. From the fluorescence measurement, we found that ~ 120 ± 20 strands of DNA were functionalized per particle. (Figure 5.6 and Table 5.1) Control experiments using non-thiolated DNA strands indicated a negligible amount of DNA (0.3 strands

attached per particle, data in Table 5.1) was detectable, suggesting that the attachment of DNA was via the thiol-gold interaction and there were little nonspecific binding of DNA to the polymer layer. In comparison to the maximum loading of 180 ± 20 DNA strands that were isotropically functionalized on a spherical 20 nm AuNP,[54] the DNA density on one a-DNA-AuNP is comparable considering that only half of the particle surface was available for functionalization. Therefore, the high-density DNA functionalization suggests that the surface of AuNP is suitable to be functionalized with any thiolated ligand, similar to the versatility of the citrate-capped AuNP. Functionalization of high-density DNA on the a-DNA-AuNP is also advantageous as such feature has been shown to increase AuNP stability and allow cooperative effects in DNA directed assembly.[55]

Progressing from the fluorescence results that indicates successful DNA (D1) attachment on the a-DNA-AuNP, we probed the regioselectivity of the functionalization of D1 on the a-(D1)-AuNP. AuNPs of 5 nm functionalized with complementary sequence to D1 (c-AuNP) were used to probe the hybridization ability and position of the DNA. Excess 5 nm c-AuNPs were removed via centrifugation. TEM micrographs of the mixture showed that the 5 nm c-AuNPs only attached on the exposed AuNP region and no particles where found on the polymer shell (Figure 5.4b and Figure 5.7a), indicating that the D1 DNA on a-(D1)-AuNP not only retained its hybridization ability but also regioselectivity as demonstrated. When 5 nm AuNPs with non-complementary strands were used, most of the 5 nm AuNPs were washed away leaving no significant attachment of 5 nm AuNPs on a-(D1)-AuNP (Figure 5.7b). These results clearly indicate that a-(D1)-AuNP interacts and assembles with other particles via specific hybridization of DNA and non-specific interaction was minimal.

Since the interaction is sequence-specific, we then expand the scope of asymmetric assembly with the use of AuNP of various sizes but functionalized with the same cDNA. As an example, the same a-DNA-AuNP was conjugated to either 5 nm or 10 nm AuNP and a cat-paw like structure was formed (see Figure 2b and 2c, respectively). For the assembly with 5 nm c-AuNPs, we found that there were on average 5 ± 2 particles regioselectively attached on each anisotropic particle from a count of total 81 particles tabulated from TEM micrographs (see histogram in Figure 2b). For 10 nm c-AuNPs, the average particle number on one a-DNA-AuNP was lower, at 3 ± 1 from a total of 107 particles (see histogram in Figure 2c and large area view in Figure 5.7c). The standard deviation was also slightly lower for the 10 nm c-AuNP as compared to the 5 nm c-AuNP, as the sizes of the particle is more comparable to the a-DNA-AuNP. With regioselectivity of a-(D1)-AuNP, the interaction between particles is well controlled to have specific and directional cluster assemblies.

Having demonstrated regioselectivity of the a-DNA-AuNP, we further explored its application in controlling formation of more complex structures. As shown in Figures 5.8a and 5.9, using 30 nm AuNP as an example, when the concentration of a-DNA-AuNP is the same as that of c-AuNP, an interaction of one a-(D1)-AuNP with one 30 nm c-AuNP was achieved. When an excess of a-(D1)-AuNP to 30 nm c-AuNP (10:1) was used, satellite assemblies were formed with multiple a-(D1)-AuNPs surrounding the 30 nm c-AuNP (Figure 5.8a, and Figure 5.10). Previous reports of AuNP assembly using isotropically-labeled DNA-AuNPs often resulted in AuNPs aggregates.[56,57] While herein the protection offered by the organic polymers on the a-DNA-AuNP made it possible to prepare monodispersed satellite assemblies (Figure 5.11)

To demonstrate even better control over assemblies between two particles, instead of using one anisotropic particle and one isotropically functionalized particle, we investigated the use of

only anisotropic particle for the assembly. We synthesized 20 nm a-(D1)-AuNP and 13 nm a-(D2)-AuNP functionalized respectively with D1 and D2. Mixture of the two particles at a ratio of 1 resulted in hetero-assembly of dimers consisting of a 20 nm and a 13 nm a-DNA-AuNP (Figure 5.8b and Figure 5.12), observed as snowman-like assemblies. From the TEM micrographs, we observed 85% of the assemblies formed dimers with the correct combination from a total of 47 assemblies. The remaining 15% of the assemblies were either dimers with the wrong orientation, combination or trimers and tetramers.

In addition to hetero-assembly, homo-assembly of a-(D1)-AuNP with the use of a linker strand, D3, was also investigated. The linker strand consists of the complementary sequence to D1, a single base spacer and CGCG bases at the 3′ end which can self-hybridize.[58] Since the direction and area of interaction is controlled in the a-(D1)-AuNP, we expect the formation of clusters of particles in the presence of D3. Figure 5.8c and Figure 5.13 shows Au nanoclusters consisting of 3, 4 or 5 AuNPs. However, without such directional control, aggregations of the particles will occur.[15]

In addition to regioselective functionalization of DNA onto the asymmetric hybrid particles and its use in selective and directional assemblies, a major advantage of the a-DNA-AuNPs is that they can provide two different functionalities with spatial separation preventing crosstalk or interference. Since this particle is an anisotropic gold-polymer hybrid particle, we can further introduce a second functionality through the polymer. The polymer is an amphiphilic polymer (polystyrene-b-polyacrylic acid). The carboxylic acid chain on the polyacrylic acid tail allows functionalization *via* 1-ethyl-3-(3-dimethylaminopropyl)carbodiimide (EDC) coupling chemistry with amine-based substrates. To test the localization of functionalities, we attached amine functionalized DNA with a fluorophore (FAM) label (D4) on the polymer side of a-(D1)-AuNP

giving a-(D1+D4)-AuNP (Figure 5.14a). The yield of DNA coupling was calculated to be ~ 30 DNA strands per particle. We then conjugated the a-(D1+D4)-AuNP to two different c-AuNPs, one functionalized with D2 and the other with D5. If the D1 and D4 functionalities are segregated, hybridization with D5 c-AuNP will selectively quench the fluorescence from D4, but D2 c-AuNP will not quench the fluorescence from D4. Our fluorescence results in Figure 5.14b and c strongly support that the D1 and D4 are functionalized respectively on the Au and polymer surface respectively.

In addition to functionalization through the polymer, functionalization of the nanoparticle through removal of the polymer shell and utilizing the lipid ligand was also investigated. As the PSPAA is assembled on the surface by van der Waals and hydrophobic interactions and kinetically trapped by the glassy state of the PS block polymer, addition of the a-(D1)-AuNP in to tetrahydrofuran (THF) could dissolve the glassy PS polymer and result in dissociation of the PSPAA on the surface of the nanoparticle. Upon incubation overnight and centrifugation to remove the dissolved polymer, we observed the absence of a polymer shell on the nanoparticle. 0.02% sodium dodecylsulfate (SDS) was added to the centrifuged particles to stabilize the lipid region of the nanoparticle. Despite appearing as a symmetrical gold nanoparticle in the absence of a polymer shell, the DNA on the nanoparticle retains its regiospecific hybridization ability. When 5 nm AuNP with complementary strand was added to a-(D1)-AuNP without the polymer shell, hybridization of the small particles were all located on one side of the nanoparticle (Figure 5.15). This result is promising as we have symmetrical nanoparticles which have asymmetrical ligand coating. Future directions would be to functionalize the lipid side of the nanoparticle through addition of functionalized lipids like biotin or maleimide for subsequent conjugation.

5. 3 Conclusions

In summary, we have demonstrated a facile method to prepare anisotropic DNA-functionalized AuNPs with very high yield. The method can be applied to prepare anisotropic DNA-functionalized gold nanoparticles with different sizes and a variety of DNA sequences in high density. In addition, the DNA on the a-DNA-AuNP can be readily exchanged with another DNA of difference sequences, allowing more sequence-specific control of nanoparticle assembly. The role of DNA in this ligand competition method serves as a unique bulky ligand which allows efficient post-functionalization on the gold surface. Taking advantage of this property, we have shown that the combination of a-DNA-AuNP and c-AuNP results in cat-paw and satellite flower assemblies. Furthermore, a-DNA-AuNP functionalized with different DNA strands were used to demonstrate hetero- and homo-assemblies, all with high regioselectivity and monodispersity. More importantly, the anisotropic nature of our a-DNA-AuNP allows us to regioselectively functionalize two different DNA strands and to demonstrate the localized quenching reactions. These asymmetric colloidal particles which are easily synthesized in high yields and versatile to be functionalized on both sides with desired DNA sequence or components which may interfere with each other can have great potential in biological applications for precise and specific targeting and response.[59-61] In addition, with dual functionality and directional hybridization, these anisotropic particles are promising candidate for creating optically active nano-assemblies not achievable by isotropic particles.[62]

5.4 Experimental Section

General chemical reagents were purchased from Sigma Aldrich and used without further purification. Amphiphilic diblock copolymers polystyrene-block-poly(acrylic acid) PS_{144}-*b*-PAA_{50}, M_n = 15000 for the PS block and M_n = 3600 for the PAA block, M_w / M_n = 1.20 was purchased from Polymer Source Inc.; 2-dipalmitoyl-*sn*-glycero-3-phosphothioethanol (sodium salt) (PSH) was purchased from Avanti Polar Lipids; 200 mesh copper specimen grids with formvar/carbon support film (TEM grids) was purchased from Ted Pella Inc. Twenty nanometer AuNP was purchased from British BioCell International (BBI). Thirteen nanometer AuNP were prepared following literature procedures by sodium citrate reduction of $HAuCl_4$.[63] DNA oligomers were purchased from Integrated DNA Technologies and purified by standard desalting.

Sequence of DNA used for the synthesis and functionalization.

SH-A10: 5′ SH-AAA AAA AAA A 3′

SH-A30: 5′ SH-AAA AAA AAA AAA AAA AAA AAA AAA AAA AAA 3′

SH-R20: 5′ SH-TTT TTT TTT TCA ATG CTC TGG ATC TGT GGG 3′

D1: 5′ AAC AAT TAT ACT CAG CAA TTT TTT TTT T –SH 3′

D2: 5′ TTG CTG AGT ATA ATT GTT TTT TTT TTT T –SH 3′

D3: 5′ TTG CTG AGT ATA ATT GTTA GCGC 3′

D4: 5′ NH-TTT TTT TTT T AAG AAT TTA TAA GCA GAA 3′

D5: 5′ SH-TTT TTT TTT T TTC TGC TTA TAA ATT CTT 3′

Ultrapure water with resistivity > 18 $M\Omega \cdot cm^{-1}$ was used for all experiments.

Anisotropic particle synthesis

The encapsulation was carried out according to the procedure from our previously reported paper with minor modifications.[64] 2.5 μL of 1mM thiolated DNA was treated with 0.5 μL of 100 mM sodium acetate pH 5.5 and 1.5 μL of 10 mM tris(2-carboxyethyl)phosphine (TCEP). The mixture was left at room temperature for 1 hour before purifying once with Centricon-3k to remove excess TCEP. Citrate stabilized AuNPs (~20nm, 1.5 mL) solution was centrifuged to a volume of ~15 μL using 13100 *g* for 15 min. The TCEP treated DNA was added to the concentrated AuNP and diluted with mili-Q water to a volume of 100 μL. A reaction vial (6 mL) was added 340 μL of DMF solution, PS_{144}-*b*-PAA_{50} (60 μL, 4 mg/mL in DMF), AuNP-DNA mixture and hydrophobic ligand PSH (5 μL, 0.5 mg/mL in EtOH) in order. The reaction mixture would have a total final volume of 505 μL, where V_{DMF} / V_{H2O} = 4, [AuNP]= 3.45 nM, [DNA] = 4.95 μM, [PSH]= 6.77 μM. The mixture was heated at 95 °C for 2 hr, and then allowed to cool down gradually till room temperature. Similar procedures were used for other DNA strands. The nanoparticles were purified by centrifugation where 100 μL of as-synthesized nanoparticles were diluted into 1400 μL mili-Q water to trap the nanoparticle in a kinetically stable state.

Functionalization/ligand exchange with selected DNA strands

To 5 μL of 1 mM thiol-DNA in Millipore water, 1 μL of 0.1 M sodium acetate buffer at pH 5.5 and 3.0 μL of 10 mM TCEP in Millipore water were added and mixed. This mixture was kept at room temperature for 1 hour and then purified by Centricon-3k to remove excess TCEP. 400 μL of as-synthesized nanoparticle were centrifuged one in water and another two times in 50% buffer A. The TCEP treated DNA was added to the purified particles and 100 μL of 50 mM Na-Citrate pH 3 was added to the mixture. The mixture was left overnight. Due to the low pH, the particles would sediment at the bottom of the tube but with sonication and addition of buffer A the particles would

resuspended in solution. The particles were purified with buffer A via centrifuge 6 times to ensure no free DNA remained in the supernatant.

Buffer A: 0.1 M sodium phosphate buffer, pH 7.3, 0.05% Tween-20

Buffer B: 0.1 M sodium chloride and 0.1 M sodium phosphate buffer, pH 7.3

Assembly

For demonstrating the functionality of the asymmetric nanoparticle, excess of 5 nm AuNP or 10 nm AuNP functionalized with D2 was added in large excess to the a-(D1)AuNP. The mixture was kept in buffer B and incubated at room temperature overnight. The excess 5 nm And 10 nm AuNP can be purified away via centrifugation with 1:1 buffer A and buffer B.

Ratiometric, Hetero and Homo Assembly.

The concentration of 13 nm a-(D2)AuNP, and 20 nm a-(D1)AuNP and 30 nm (D2)-AuNP were determined using the extinction coefficient 2.7×10^{8} $M^{-1}cm^{-1}$, 8.8×10^{8} $M^{-1}cm^{-1}$ and 4.7×10^{9} $M^{-1}cm^{-1}$ respectively. For the ratiometric system, snowman like assemblies were achieved when the ratio between the particles were controlled to be 1:1 while a ratio of 10:1 was used to give satellite structures. For hetero particle assembly, ratio of 1:1, 13nm a-(D2)AuNP and 20nm a-(D1)AuNP were used. For the homo particle assembly, D3 was added at 120 times of the particle concentration to give approximately 1:1 ratio of D1 to the linker. All the assemblies were performed in buffer B and imaged without further purification. Except for homo particle assembly, where the 0.5 M NaCl and 50 mM NaPi pH 7 were used.

DNA quantification

FAM-labeled DNA was functionalized on a-(DNA)AuNP. The AuNP concentration was first determined by UV-vis. Fluorescence of sample upon etching of the AuNP (50 μL) by KCN (10 μL, 100mM) was determined using a fluorometer. The fluorescence intensity was correlated to the DNA concentration present in the solution and divided by the number of particles to determine the number of DNA on each particle. To determine the amount of DNA that non-specifically attach to the particle, non-thiolated FAM DNA was used as a control.

Equipment and Characterizations

The particles synthesized as well as the nano-assemblies formed were analyzed using JEOL 2010LaB6/ 2100cryo transmission electron microscope (TEM) operated at 200 kV. Samples were prepared by mixing 4 μL of nanoparticle solution and 4 μL of $(NH_4)_6Mo_7O_{24}$ (40 mM) and then added onto a fomvar/carbon-coated copper TEM grid (Ted pella). $(NH_4)_6Mo_7O_{24}$ was used as a negative stain to increase the contrast of the polymer. Nanoparticle concentrations were characterized by the absorbance at 535 nm using UV-Vis spectrophotometry (Hewlett–Packard 8453). Fluorescence measurements were carried out on a Fluoromax-2 fluorimeter (HORIBA Jobin Yvon inc., Edison, NJ) to determine the concentration of fluorophore labeled DNA.

Calculation of anisotropic particle yields.

We cannot rule out the possibility that particles that appear to be fully encapsulated may be a result of the particles viewed when the particle is aligned parallel to the beam. Particles are deemed anisotropic when the AuNP appears to be off-center from the polymer shell while AuNP which are positioned at the center of the polymer shell will be deemed fully encapsulated.

For THF removal of polymer shell, a-(D1)-AuNP upon synthesis was concentrated and added with 200 μL THF and 20 μL H_20. The solution was incubated overnight and centrifuged to remove supernatant. Upon removal of supernatant 50μL of 0.02% SDS was added to the pallet and resuspended by sonication. The nanoparticles upon removal of polymer were tested for its regioselective hybridization by addition of 5 nm c-AuNP.

5.5 References

(1) Alivisatos, A. P.; Johnsson, K. P.; Peng, X.; Wilson, T. E.; Loweth, C. J.; Bruchez, M. P.; Schultz, P. G. *Nature* **1996**, *382*, 609.

(2) Sheikholeslami, S.; Jun, Y.-w.; Jain, P. K.; Alivisatos, A. P. *Nano Lett.* **2010**, *10*, 2655.

(3) Yan, W.; Xu, L.; Xu, C.; Ma, W.; Kuang, H.; Wang, L.; Kotov, N. A. *J. Am. Chem. Soc.* **2012**, *134*, 15114.

(4) Deng, Z.; Tian, Y.; Lee, S.-H.; Ribbe, A. E.; Mao, C. *Angew. Chem. Int. Ed.* **2005**, *44*, 3582.

(5) Ding, B.; Deng, Z.; Yan, H.; Cabrini, S.; Zuckermann, R. N.; Bokor, J. *J. Am. Chem. Soc.* **2010**, *132*, 3248.

(6) Zhao, Y.; Xu, L.; Liz-Marzán, L. M.; Kuang, H.; Ma, W.; Asenjo-García, A.; García de Abajo, F. J.; Kotov, N. A.; Wang, L.; Xu, C. *J. Phys. Chem. Lett.* **2013**, *4*, 641.

(7) Aldaye, F. A.; Sleiman, H. F. *Angew. Chem. Int. Ed.* **2006**, *45*, 2204.

(8) Zheng, J.; Constantinou, P. E.; Micheel, C.; Alivisatos, A. P.; Kiehl, R. A.; Seeman, N. C. *Nano Lett.* **2006**, *6*, 1502.

(9) Sharma, J.; Chhabra, R.; Cheng, A.; Brownell, J.; Liu, Y.; Yan, H. *Science* **2009**, *323*, 112.

(10) Tan, S. J.; Campolongo, M. J.; Luo, D.; Cheng, W. *Nature Nanotech.* **2011**, *6*, 268.

(11) Nykypanchuk, D.; Maye, M. M.; van der Lelie, D.; Gang, O. *Nature* **2008**, *451*, 549.

(12) Maye, M. M.; Kumara, M. T.; Nykypanchuk, D.; Sherman, W. B.; Gang, O. *Nature Nanotech.* **2010**, *5*, 116.

(13) Macfarlane, R. J.; Lee, B.; Jones, M. R.; Harris, N.; Schatz, G. C.; Mirkin, C. A. *Science* **2011**, *334*, 204.

(14) Xu, L.; Ma, W.; Wang, L.; Xu, C.; Kuang, H.; Kotov, N. A. *Chem. Soc. Rev.* **2013**, *42*, 3114.

(15) Mirkin, C. A.; Letsinger, R. L.; Mucic, R. C.; Storhoff, J. J. *Nature* **1996**, *382*, 607.

(16) Katz, E.; Willner, I. *Angew. Chem. Int. Ed.* **2004**, *43*, 6042.

(17) Lau, P. S.; Li, Y. F. *Curr. Org. Chem.* **2011**, *15*, 557.

(18) Tikhomirov, G.; Hoogland, S.; Lee, P. E.; Fischer, A.; Sargent, E. H.; Kelley, S. O. *Nat Nano* **2011**, *6*, 485.

(19) Du, J.; Jiang, L.; Shao, Q.; Liu, X.; Marks, R. S.; Ma, J.; Chen, X. *Small* **2013**, *9*, 1467.

(20) Kumar, A.; Hwang, J.-H.; Kumar, S.; Nam, J.-M. *Chem. Commun.* **2013**, *49*, 2597.

(21) Barrow, S. J.; Funston, A. M.; Wei, X.; Mulvaney, P. *Nano Today* **2013**, *8*, 138.

(22) Aldaye, F. A.; Sleiman, H. F. *J. Am. Chem. Soc.* **2007**, *129*, 4130.

(23) Hu, S.-H.; Gao, X. *J. Am. Chem. Soc.* **2010**, *132*, 7234.

(24) Xu, L.; Kuang, H.; Xu, C.; Ma, W.; Wang, L.; Kotov, N. A. *J. Am. Chem. Soc.* **2011**, *134*, 1699.

(25) Yan, J.; Bloom, M.; Bae, S. C.; Luijten, E.; Granick, S. *Nature* **2012**, *491*, 578.

(26) Suzuki, K.; Hosokawa, K.; Maeda, M. *J. Am. Chem. Soc.* **2009**, *131*, 7518.

(27) Du, J.; O'Reilly, R. K. *Chem. Soc. Rev.* **2011**, *40*, 2402.

(28) Zhang, S.; Li, Z.; Samarajeewa, S.; Sun, G.; Yang, C.; Wooley, K. L. *J. Am. Chem. Soc.* **2011**, *133*, 11046.

(29) Wang, Y.; Wang, Y.; Breed, D. R.; Manoharan, V. N.; Feng, L.; Hollingsworth, A. D.; Weck, M.; Pine, D. J. *Nature* **2012**, *491*, 51.

(30) Xu, X.; Rosi, N. L.; Wang, Y.; Huo, F.; Mirkin, C. A. *J. Am. Chem. Soc.* **2006**, *128*, 9286.

(31) Sardar, R.; Heap, T. B.; Shumaker-Parry, J. S. *J. Am. Chem. Soc.* **2007**, *129*, 5356.

(32) Claridge, S. A.; Liang, H. W.; Basu, S. R.; Fréchet, J. M. J.; Alivisatos, A. P. *Nano Lett.* **2008**, *8*, 1202.

(33) Mastroianni, A. J.; Claridge, S. A.; Alivisatos, A. P. *J. Am. Chem. Soc.* **2009**, *131*, 8455.

(34) Maye, M. M.; Nykypanchuk, D.; Cuisinier, M.; van der Lelie, D.; Gang, O. *Nat. Mater.* **2009**, *8*, 388.

(35) Yoon, J. H.; Lim, J.; Yoon, S. *ACS Nano* **2012**, *6*, 7199.

(36) Perro, A.; Reculusa, S.; Ravaine, S.; Bourgeat-Lami, E.; Duguet, E. *J. Mater. Chem.* **2005**, *15*, 3745.

(37) Walther, A.; Muller, A. H. E. *Soft Matter* **2008**, *4*, 663.

(38) Jiang, S.; Chen, Q.; Tripathy, M.; Luijten, E.; Schweizer, K. S.; Granick, S. *Adv. Mater.* **2010**, *22*, 1060.

(39) Lee, J.-H.; Kim, G.-H.; Nam, J.-M. *J. Am. Chem. Soc.* **2012**, *134*, 5456.

(40) Ohnuma, A.; Cho, E. C.; Camargo, P. H. C.; Au, L.; Ohtani, B.; Xia, Y. *J. Am. Chem. Soc.* **2009**, *131*, 1352.

(41) Chen, T.; Chen, G.; Xing, S.; Wu, T.; Chen, H. *Chem. Mater.* **2010**, *22*, 3826.

(42) Li, Z.; Cheng, E.; Huang, W.; Zhang, T.; Yang, Z.; Liu, D.; Tang, Z. *J. Am. Chem. Soc.* **2011**, *133*, 15284.

(43) Gröschel, A. H.; Walther, A.; Löbling, T. I.; Schmelz, J.; Hanisch, A.; Schmalz, H.; Müller, A. H. E. *J. Am. Chem. Soc.* **2012**, *134*, 13850.

(44) He, J.; Perez, M. T.; Zhang, P.; Liu, Y.; Babu, T.; Gong, J.; Nie, Z. *J. Am. Chem. Soc.* **2012**, *134*, 3639.

(45) Loweth, C. J.; Caldwell, W. B.; Peng, X.; Alivisatos, A. P.; Schultz, P. G. *Angew. Chem. Int. Ed.* **1999**, *38*, 1808.

(46) Worden, J. G.; Shaffer, A. W.; Huo, Q. *Chem. Commun. (Cambridge, U. K.)* **2004**, 518.

(47) Sung, K.-M.; Mosley, D. W.; Peelle, B. R.; Zhang, S.; Jacobson, J. M. *J. Am. Chem. Soc.* **2004**, *126*, 5064.

(48) Xing, H.; Wang, Z.; Xu, Z.; Wong, N. Y.; Xiang, Y.; Liu, G. L.; Lu, Y. *ACS Nano* **2011**, *6*, 802.

(49) Chen, T.; Yang, M.; Wang, X.; Tan, L. H.; Chen, H. *J. Am. Chem. Soc.* **2008**, *130*, 11858.

(50) Wang, H.; Chen, L.; Feng, Y.; Chen, H. *Acc. Chem. Res.* **2013**, *46*, 1636.

(51) Hostetler, M. J.; Templeton, A. C.; Murray, R. W. *Langmuir* **1999**, *15*, 3782.

(52) Guo, R.; Song, Y.; Wang, G.; Murray, R. W. *J. Am. Chem. Soc.* **2005**, *127*, 2752.

(53) Zhang, X.; Servos, M. R.; Liu, J. *J. Am. Chem. Soc.* **2012**, *134*, 7266.

(54) Hill, H. D.; Millstone, J. E.; Banholzer, M. J.; Mirkin, C. A. *ACS Nano* **2009**, *3*, 418.

(55) Elghanian, R.; Storhoff, J. J.; Mucic, R. C.; Letsinger, R. L.; Mirkin, C. A. *Science* **1997**, *277*, 1078.

(56) Liu, J.; Lu, Y. *J. Am. Chem. Soc.* **2003**, *125*, 6642.

(57) Wang, Z.; Lu, Y. *J. Mater. Chem.* **2009**, *19*, 1788.

(58) Park, S. Y.; Lytton-Jean, A. K. R.; Lee, B.; Weigand, S.; Schatz, G. C.; Mirkin, C. A. *Nature* **2008**, *451*, 553.

(59) Verma, A.; Uzun, O.; Hu, Y.; Hu, Y.; Han, H.-S.; Watson, N.; Chen, S.; Irvine, D. J.; Stellacci, F. *Nat. Mater.* **2008**, *7*, 588.

(60) Wu, L. Y.; Ross, B. M.; Hong, S.; Lee, L. P. *Small* **2010**, *6*, 503.

(61) Walther, A.; Müller, A. H. E. *Chem. Rev.* **2013**, *113*, 5194.

(62) Chen, Q.; Whitmer, J. K.; Jiang, S.; Bae, S. C.; Luijten, E.; Granick, S. *Science* **2011**, *331*, 199.

(63) Ji, X.; Song, X.; Li, J.; Bai, Y.; Yang, W.; Peng, X. *J. Am. Chem. Soc.* **2007**, *129*, 13939.

(64) Richards, C. I.; Choi, S.; Hsiang, J.-C.; Antoku, Y.; Vosch, T.; Bongiorno, A.; Tzeng, Y.-L.; Dickson, R. M. *J. Am. Chem. Soc.* **2008**, *130*, 5038.

5.6 Figures

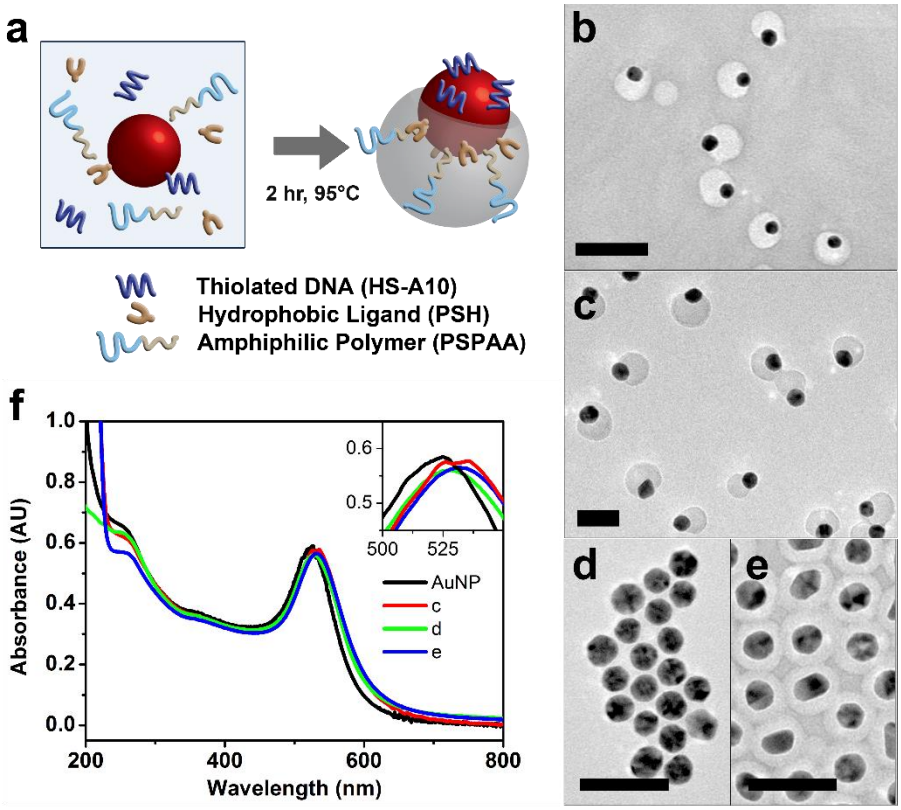

Figure 5.1. (a) Schematic for the synthesis of a-DNA-AuNP where HS-A10, PSH, PSPAA and AuNP are incubated at 95°C for two hours in DMF/H_2O. TEM micrographs of (b) 15 nm a-DNA-AuNP, (c) 20 nm a-AuNP, (d) completely unencapsulated AuNP when no PSH was added, (e) fully encapsulated AuNP when no SH-A10 was added. (f) UV-vis absorption spectra of citrate-capped AuNP, the a-DNA-AuNP sample in (b), and fully encapsulated AuNP (d), inset shows the shift of plasmon peak from 525 nm to 535 nm. Scale bar = 50 nm.

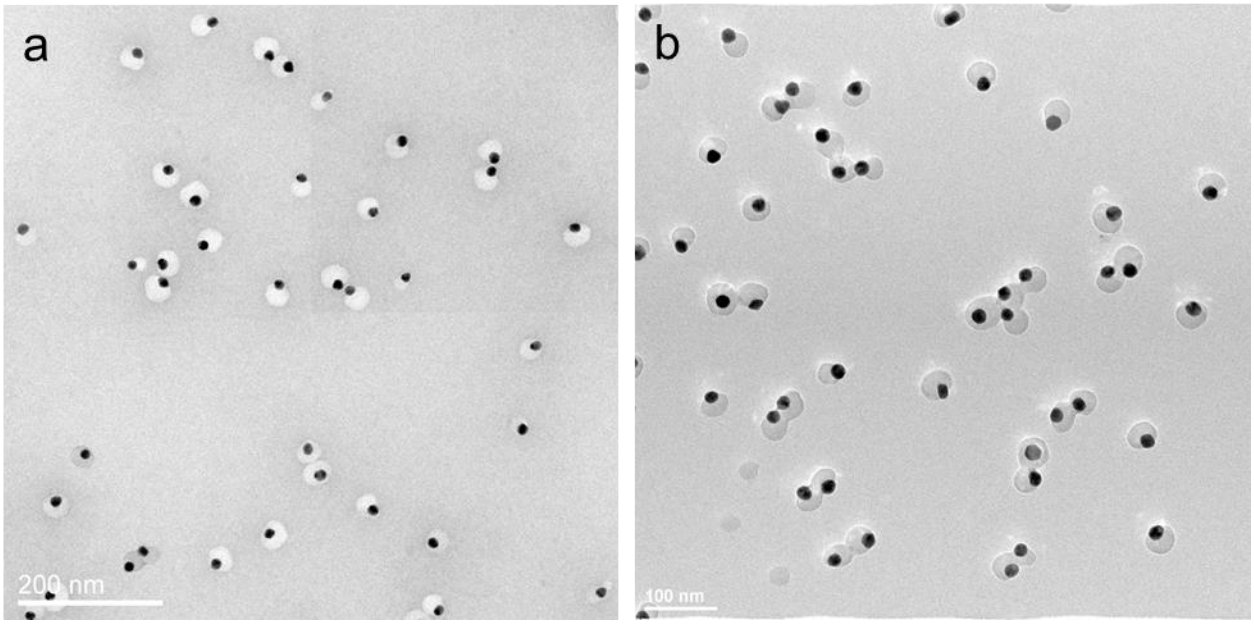

Figure 5.2. (a) Large area view of a-AuNP synthesized with 15 nm AuNP and SH-A10 as the hydrophilic ligand. (b) Large area view of a-AuNP synthesized with 20 nm AuNP and SH-A10 as the hydrophilic ligand.

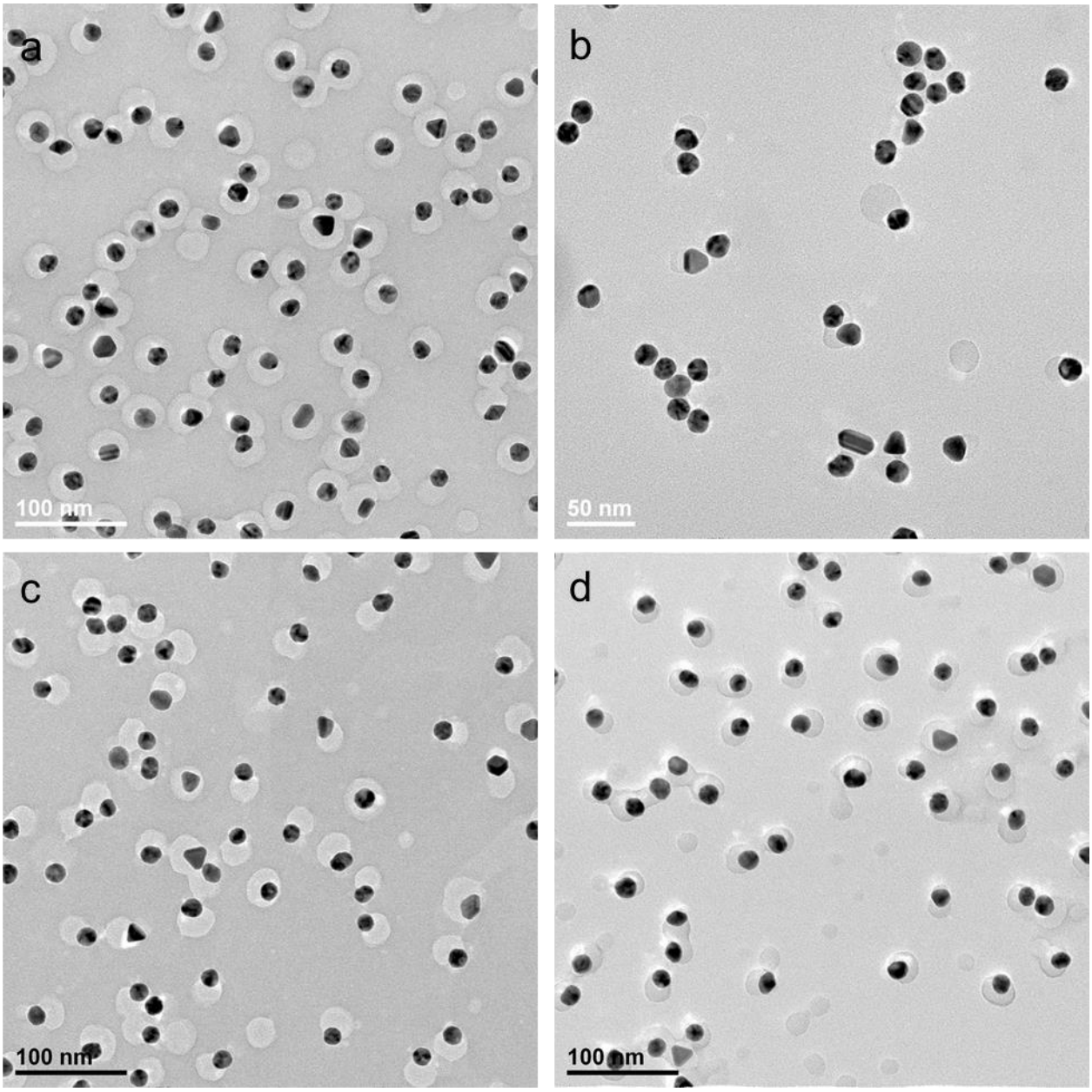

Figure 5.3. (a) Large area view of a-AuNP synthesized with 20 nm AuNP and SH-A10 as the hydrophilic ligand. The ratio of PSH:DNA used is 2.2. (b) Large area view of a-AuNP synthesized with 20 nm AuNP and SH-A10 as the hydrophilic ligand. The ratio of PSH:DNA used is 1. (c) Large area view of a-AuNP synthesized with 20 nm AuNP and SH-A30 as the hydrophilic ligand. The ratio of PSH:DNA used is 2.2. (d) Large area view of a-AuNP synthesized with 20 nm AuNP and SH-R20 as the hydrophilic ligand. The ratio of PSH:DNA used is 5.6.

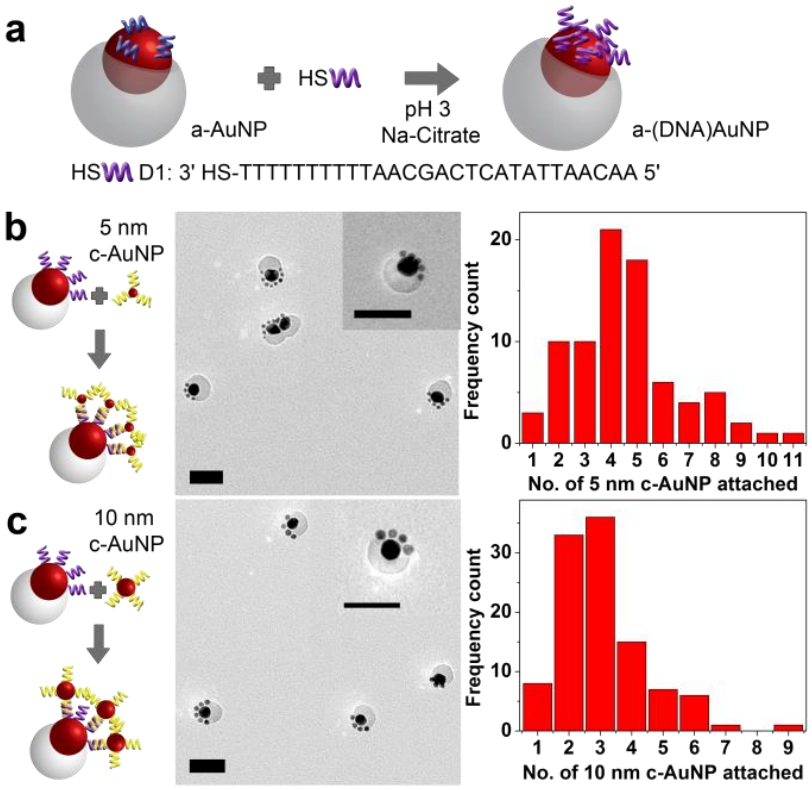

Figure 5.4. (a) Schematic for the functionalization of a-AuNP with D1 resulting in a-(D1)-AuNP. Schematic of selective assembly of a-(D1)-AuNP (b) with 5 nm c-AuNPs and (c) 10 nm c-AuNPs with its corresponding TEM micrographs and histogram showing particle analysis. Scale bars are 50 nm.

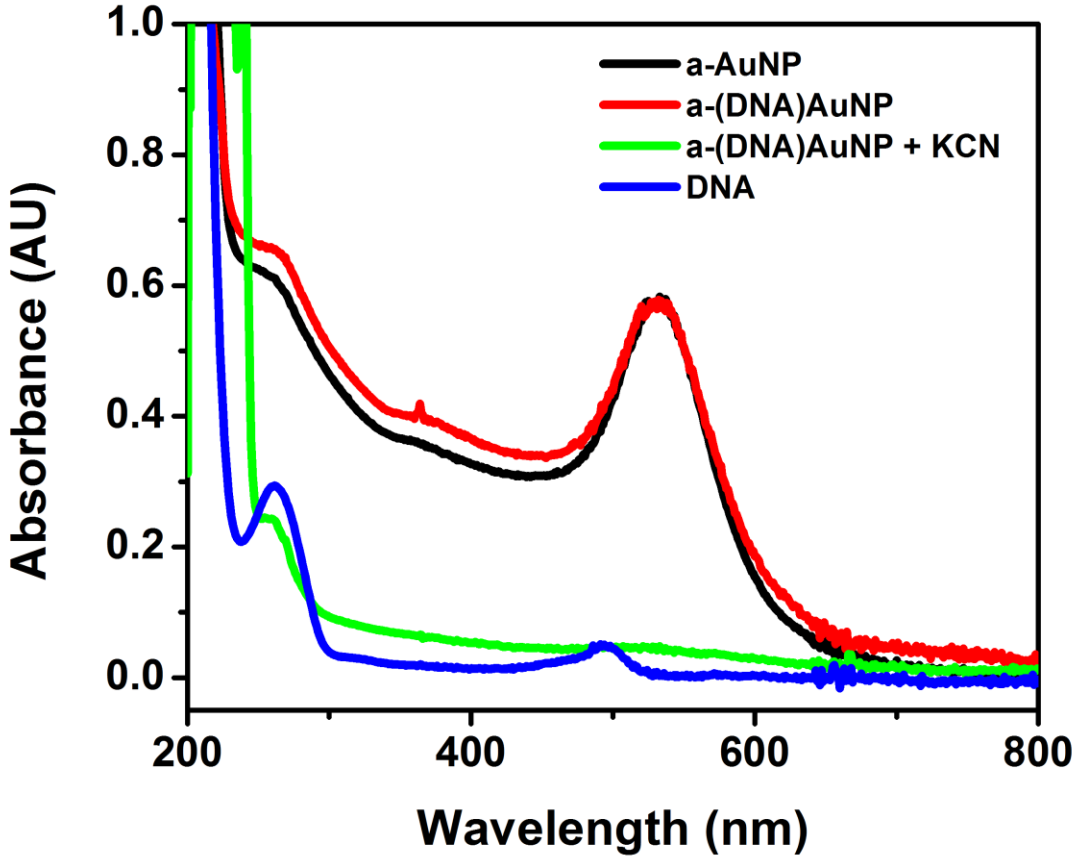

Figure 5.5. UV-vis absorbance for a-AuNP before and after ligand exchange with desired DNA. Also shown is the absorbance of a-DNA-AuNP after incubation with KCN to ensure all AuNP has been etched away and quantification of DNA can be carried out.

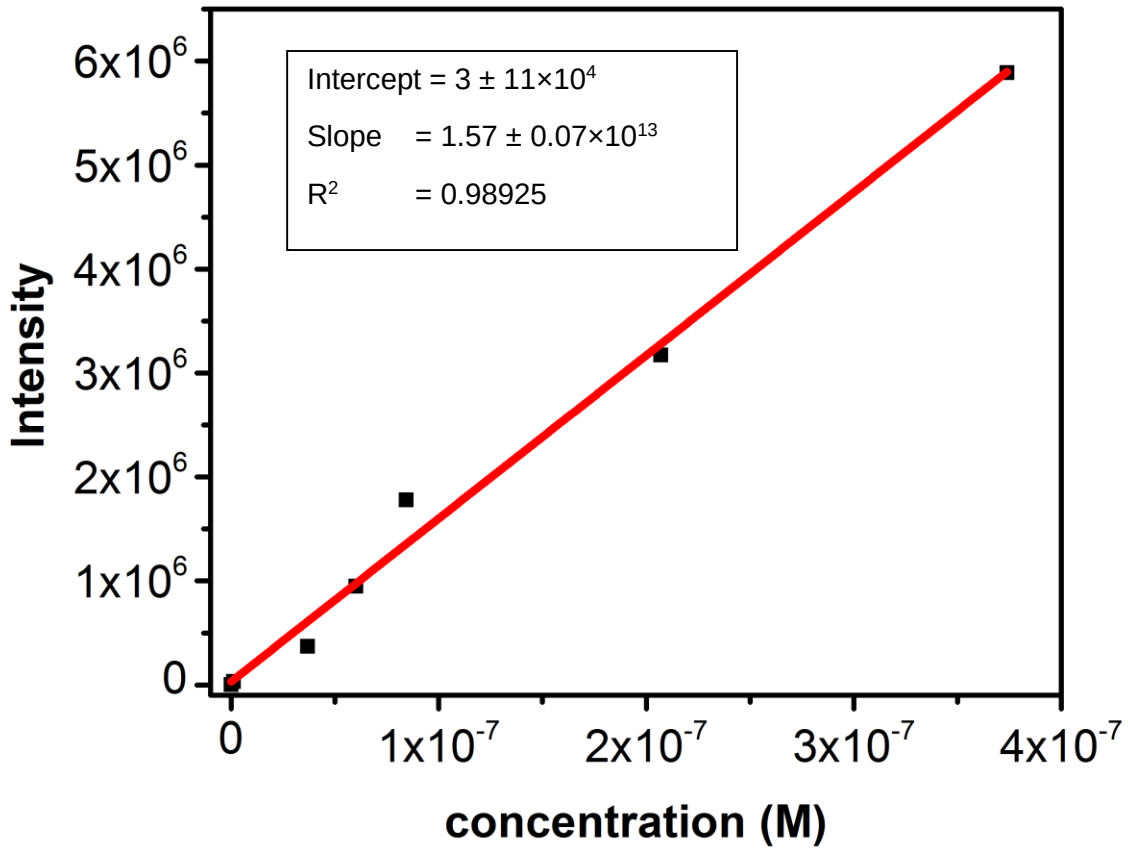

Figure 5.6. Fluorescence calibration curve for measuring DNA concentration on AuNP after synthesis.

Table 5.1. Table shows measurements and calculation to obtain amount of DNA per AuNP. Three measurements was taken for the sample and the concentration was calculated from the slope and intercept values obtained from this graph. The number of DNA on each particle was obtained by dividing the concentration of DNA with the concentration of particles.

	Thiolated DNA on AuNP	Non-thiolated DNA on AuNP
Concentration calculated from fluorescence (M)	2.41E-07	6.10E-10
	2.09E-07	6.68E-10
	2.08E-07	4.97E-10
Average concentration (M)	2.20E-04	2.20E-04
Standard deviation (M)	4.59E-11	1.47E-13
Volume of fluorophore (L)	2.20E-04	2.20E-04
No. of moles of DNA	4.82E-11	1.30E-13
No. of moles of AuNP	3.70E-13	3.86E-13
DNA/AuNP	**1.30E+02**	**3.37E-01**
Calculated error for DNA/AuNP	2.40E+01	

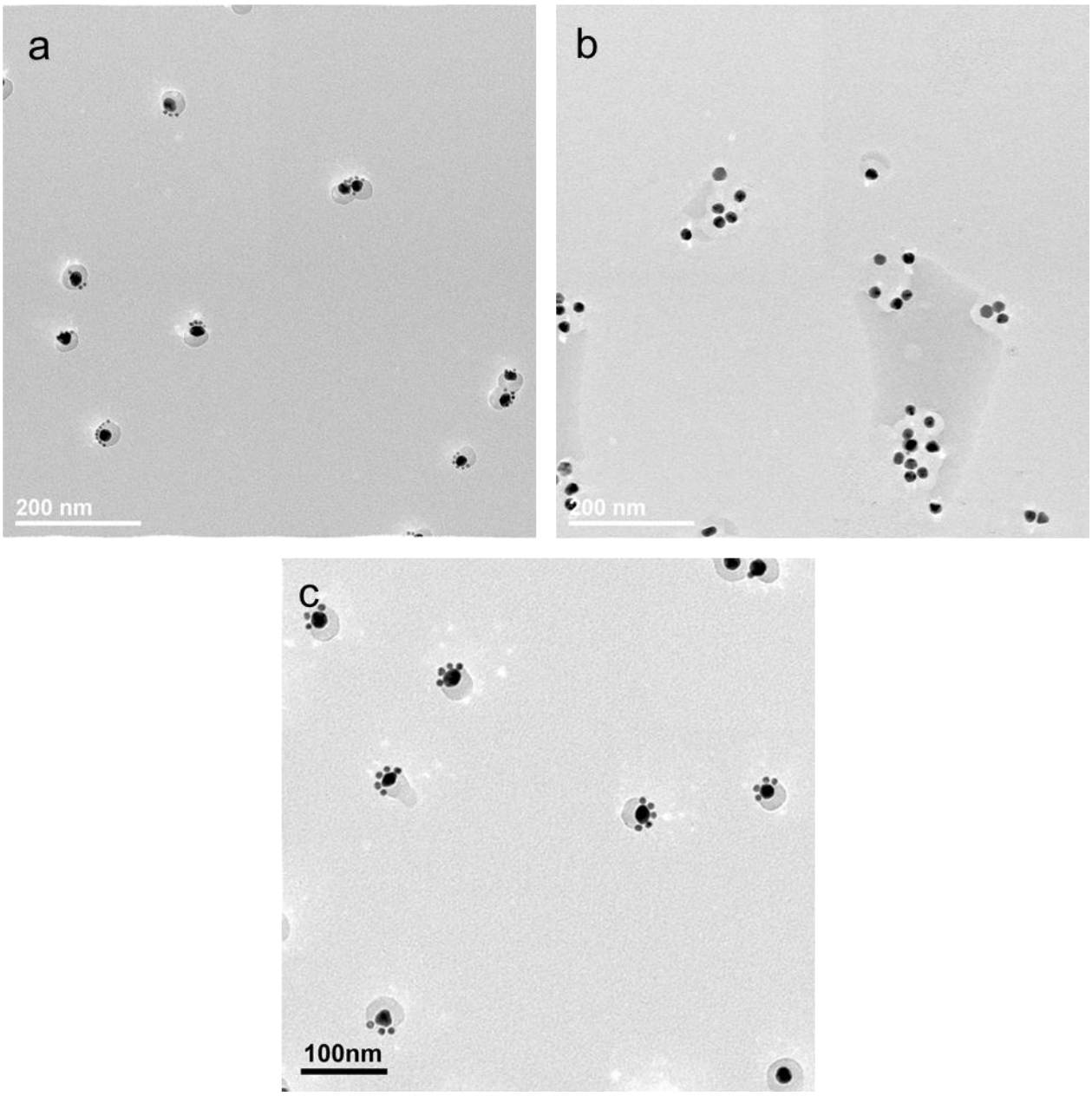

Figure 5.7. (a) Large area view of selective hybridization of a-(D1)AuNP (20 nm) and c-(D2)AuNP (5 nm). (b) Large area view of selective hybridization of a-(D1)AuNP (20 nm) and 5 nm AuNP functionalized with non-complementary strand. No 5 nm AuNP was attached indicating the selectivity offered by the DNA strand. (c) Large area view of selective hybridization of a-(D1)AuNP (20 nm) and c-(D2)AuNP (10 nm).

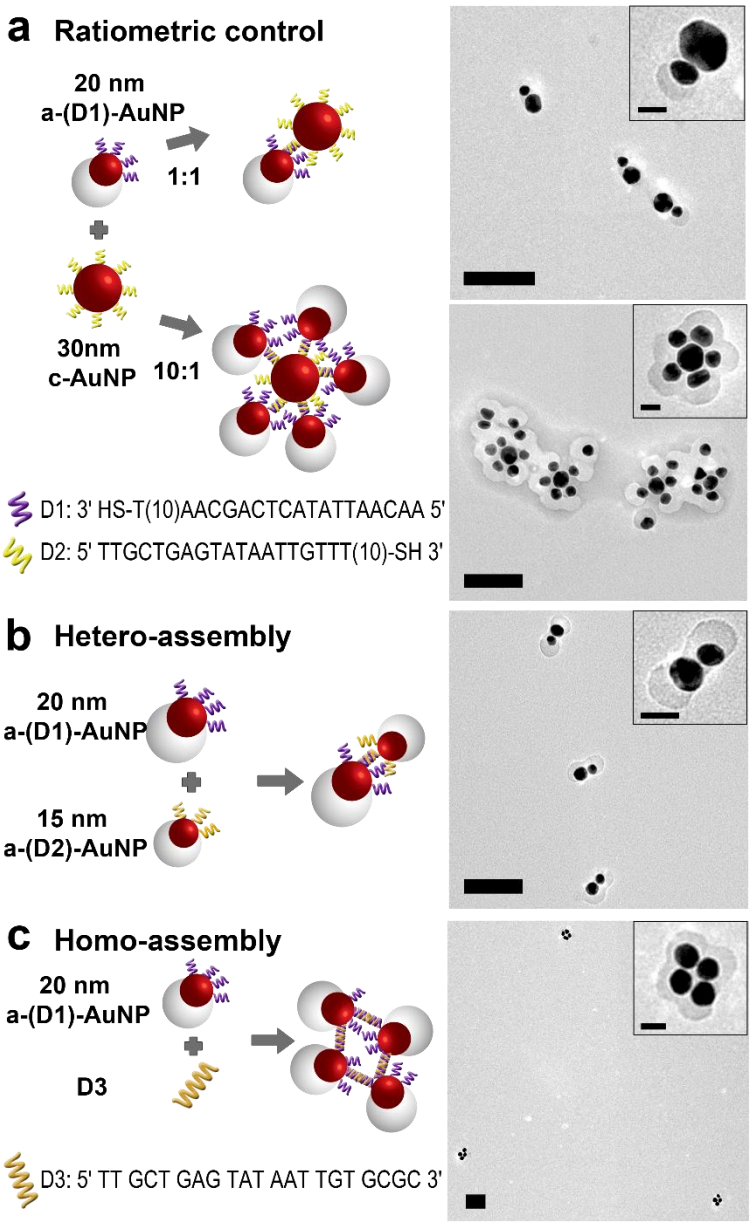

Figure 5.8. (a) a-(D1)-AuNP – 30 nm c-AuNP assemblies at a ratio of 1:1 (upper) and 10:1 (lower). (b) Hetero-assembly of 20 nm and 13 nm a-(D1)-AuNP. (c) Homo –assembly of a-(D1)-AuNP using a linker strand D3. Scale bar = 100 nm; (insets) 25 nm.

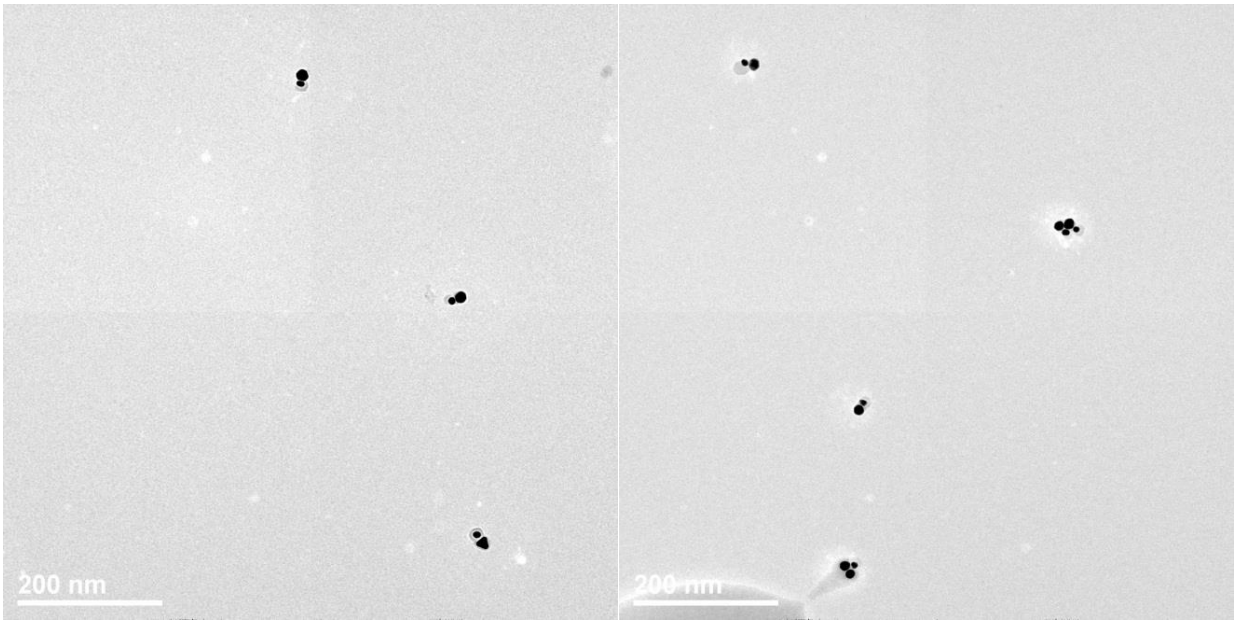

Figure 5.9. Additional TEM micrographs selective hybridization of a-(D1)AuNP (20 nm) and c-(D2)AuNP (30 nm) at ratio of 1:1.

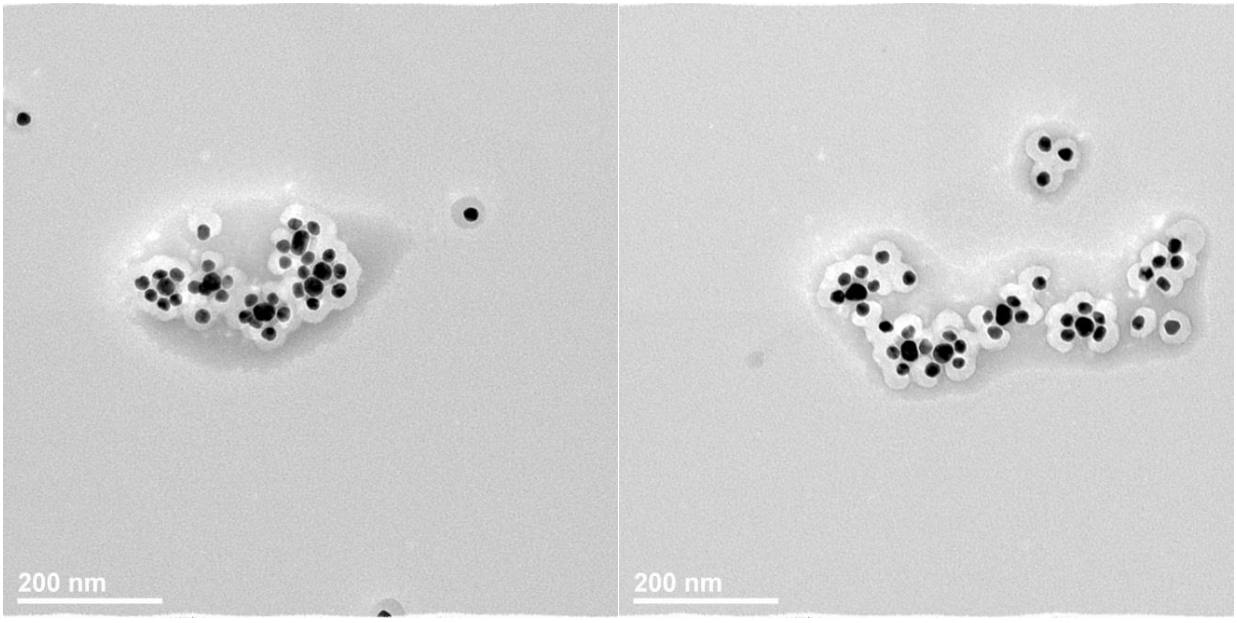

Figure 5.10. Additional TEM micrographs selective hybridization of hybridization of a-(D1)-AuNP (20 nm) and c-(D2)AuNP (30 nm) at ratio of 10:1.

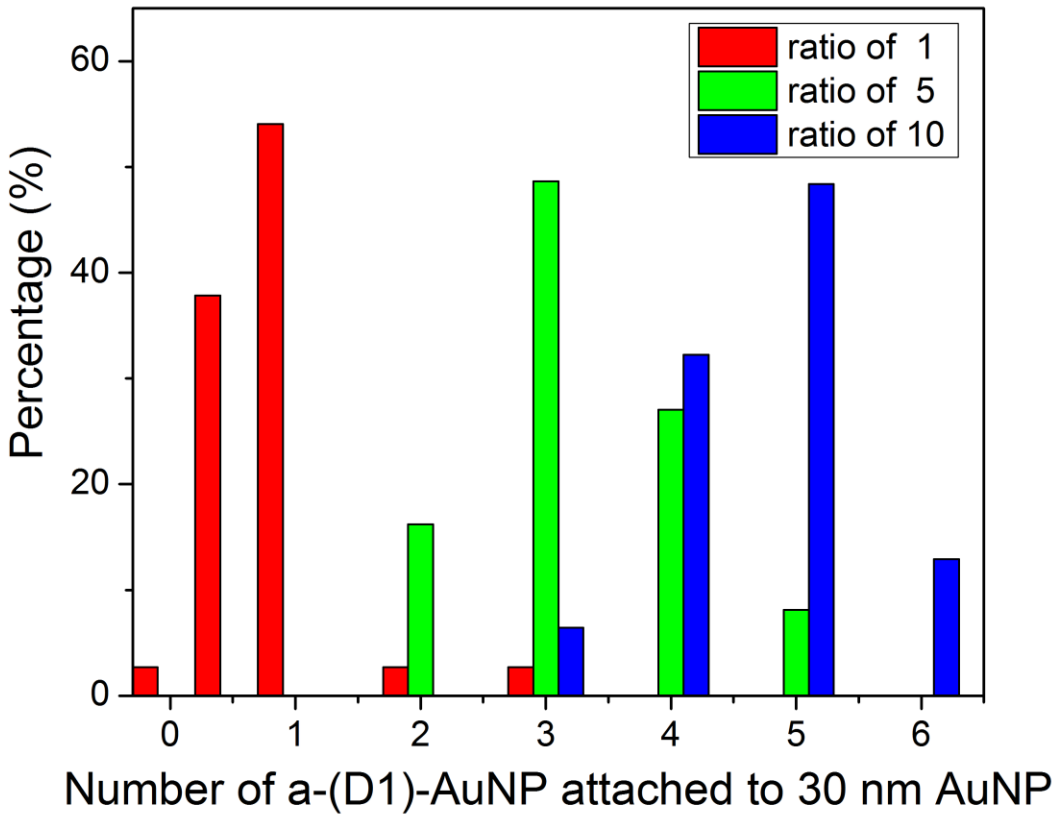

Figure 5.11. Bar graph showing distribution of hybridization of a-(D1)-AuNP (20 nm) and c-(D2)AuNP (30 nm) at ratios of 1:1, 5:1 and 10:1.

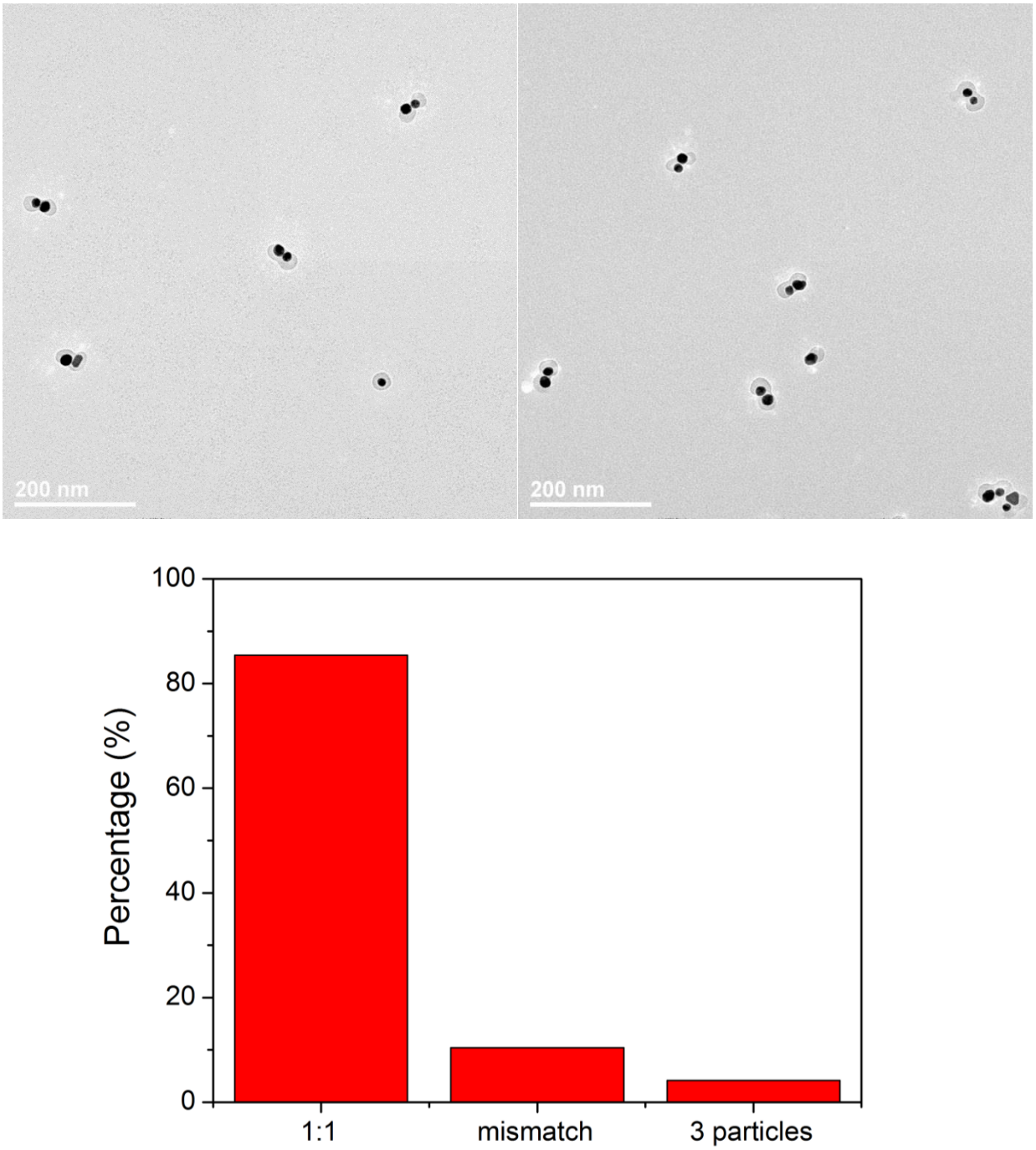

Figure 5.12. Additional TEM micrographs selective hybridization of a-(D1)AuNP (20 nm) and c-(D2)AuNP (13 nm).Graph at the bottom shows percentage of particles with correct dimer formation, mismatch and with 3 or more aggregates.

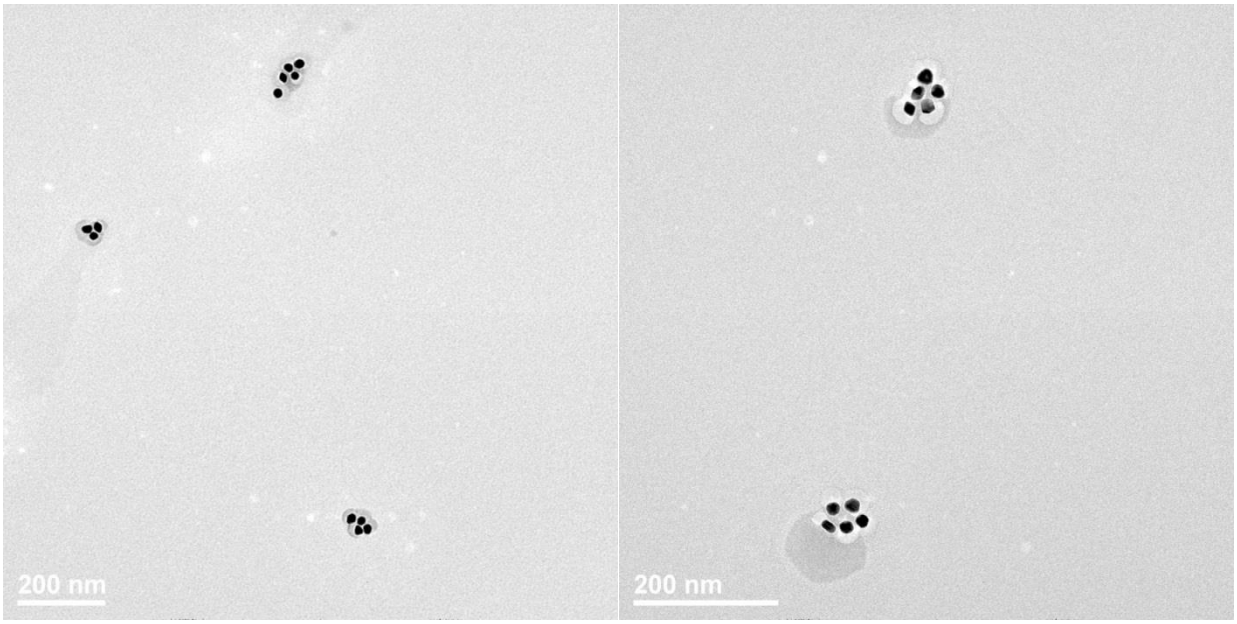

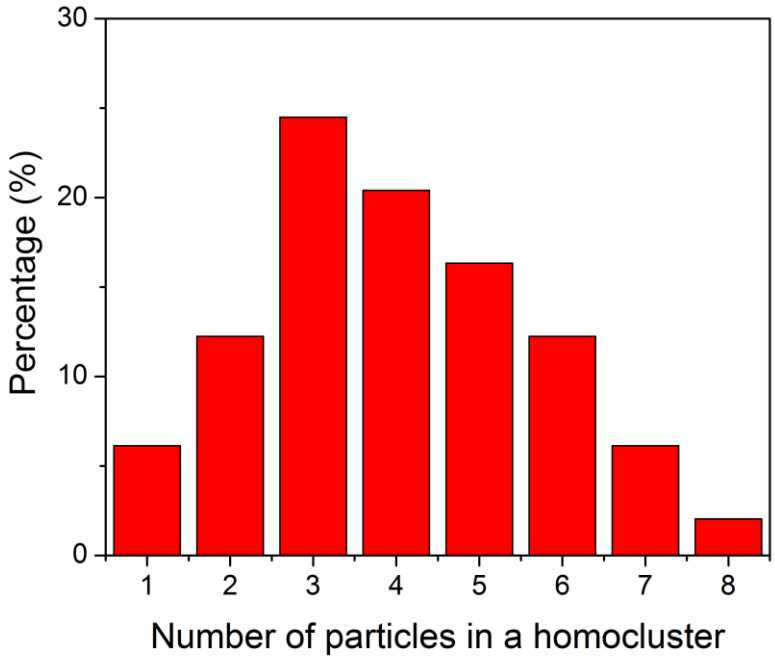

Figure 5.13. Additional TEM micrographs of homo-assembly of a-(D1)AuNP (20 nm) with D3 DNA and graph showing the distribution of particles in a homo-assembled cluster.

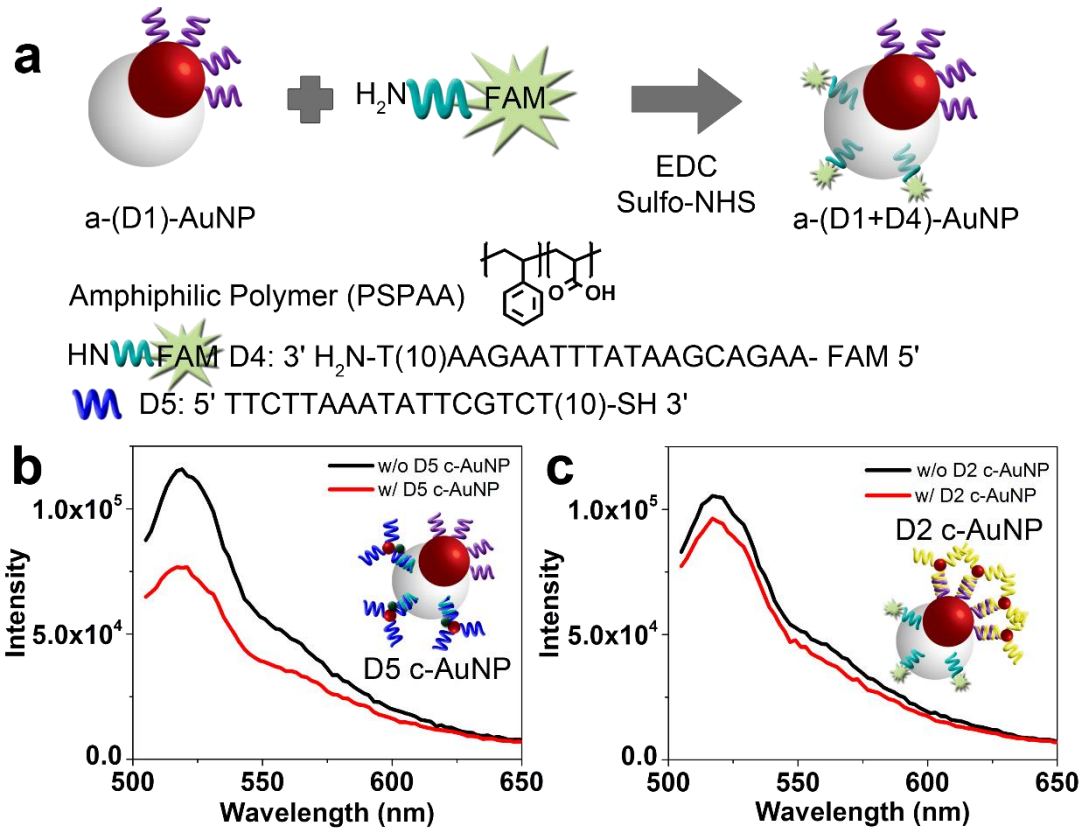

Figure 5.14. (a) Scheme showing functionalization of D4 on the polymer side of the particle *via* EDC coupling. Fluorescence spectra of a-(D1+D4)-AuNP before and after incubation with (b) D5 c-AuNP and (c) D2 c-AuNP.

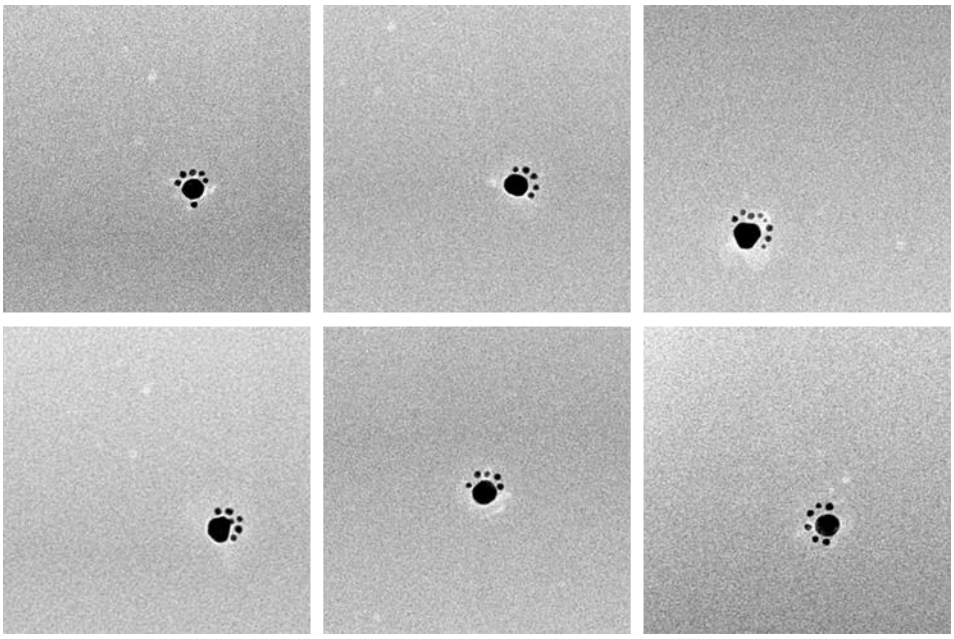

Figure 5.15. TEM micrographs of selective hybridization of a-(D1)AuNP (20 nm) with its polymer shell removed by THF and c-(D2)AuNP (5 nm).

CHAPTER 6

DNA STABILITY AND DEGRADATION ON GOLD NANOPARTICLES

6.1 Introduction

Nanomaterials have attracted great attention in the field of biology and medicine. Gold nanoparticles (AuNPs) for instance have been used for targeting, sensing, imaging and delivery.[1-5] The increase in applications of nanomaterials in biology has driven a great concern about the health risks and long term effects of these particles. AuNPs are generally considered inert and non-toxic, however, recent reports suggest that AuNPs could induce oxidative damage in cells.[6] The effect of AuNP on the viability of cells vary depending on various factors including the concentration of AuNP,[7] surface charge,[8] and size[9]. A concentration of AuNP above 50 μg/mL was found to result in detectable DNA damage, while the extent of toxicity was also highly correlated with the uptake efficiency of the particles. While many studies have incubated the AuNP with cells to investigate DNA damage or cell viability, there are few reported studies that systematically investigated the degradation of DNA by AuNP. AuNP–DNA conjugates have been used to direct self-assemblies of plasmonic structures[10-15] and used in sensing applications.[16,17] While AuNP-DNA conjugates are useful, it is important to understand the stability of these conjugates. This study would be important not only for the bioapplicability of AuNP, but also for applications of AuNP-DNA assemblies. Previously Taton and coworkers have observed non-specific cleavage of DNA on AuNP when heated.[18] In another study, Liu and coworkers studied the stability of DNA-AuNP hybrids at solvent and salt concentrations.[19]

Here we study the stability of short DNA strands conjugated to AuNPs at various temperatures. The stability of DNA in the presence of Au was tested at various conditions: varying

time, temperature, pH, and salt concentration. The extent of DNA damage was affirmed using PAGE and analyzed using semi-automated footprinting analysis (SAFA).[20] In addition, the mechanism of degradation was investigated in the presence of radical scavengers.

6.2 Results and Discussions

This investigation initiated when we observed that DNA-AuNP conjugates became unstable as the particles were annealed at high temperatures for long periods of time. To investigate the origin of the AuNP instability at high temperatures, we used fluorophore labelled DNA-AuNP conjugates and determined the integrity of the DNA sequence by polyacrylamide gel electrophoresis (PAGE). The fluorescently tagged DNA sequence used for this experiment was 5′ SH- TTT TTT TTT T TCT TA TGT ATA CTT CTT AAT-FAM 3′. Fluorescein labelled DNA was first functionalized on 20 nm AuNPs via a thiol Au linkage using the established salt aging method and excess DNA was removed by centrifugation. The DNA-AuNP conjugates were diluted to 1.16 nM based on their absorbance at 520 nm with an extinction coefficient of 1.2×10^9 $M^{-1}cm^{-1}$, and were then heated at 95 °C for 8 hours. The DNA obtained after heating was run under PAGE to separate the cleaved products from the intact strands due to mass difference. We observed that the DNA on the nanoparticle was degraded as multiple bands were observed below the position of the intact strand (Figure 6.1a). The data from the gel indicated that few completely intact DNA strands remained in on the AuNP after heating for 8 hours. The various cleaved product bands varied in intensity, suggesting that some bases were preferentially cleaved by the AuNP.

In order to determine if the cleavage occurs only for DNA directly attached to the AuNP surface, we subsequently tested the cleavage of free DNA in the presence of AuNP. Upon running a PAGE gel on the heated samples with DNA and AuNPs (conditions 95 °C, 8 hours), we still

observed cleavage of the DNA strands. The extent of DNA cleavage when mixed with AuNP was less compared to DNA conjugated on AuNP as indicated by a higher band intensity at the uncleaved DNA position. The cleavage pattern showed clear bands which allowed us to match each distinct band with the sequence of the DNA. We observe that there were preferences for specific cleavage at purine bases adenine (A) and guanine (G). (Figure 6.1a). Cleavage did occur for the pyrimidine bases as well, however the extent of cleavage was lower. When the sample was not heated, the cleavage was insignificant. The smaller amount of cleavage observed for the non-conjugated DNA suggests that the cleavage is related to the proximity or contact between DNA and the AuNP. Therefore, the factor that induced the cleavage was not diffusible or was unable to induce extensive cleavage through the solution.

To ensure that the cleavage did not occur only at certain lengths of DNA, we tested the stability of a longer DNA strand of 43 bases on AuNP. Since there are many more bases in this strand, not all bases can be observed distinctly (Figure 6.1b). We ran the sample against a ladder in which the positions of guanines and adenines were cleaved using an established method reported by Hamsphire *et al.*, noted as GA ladder.[21] We observed that the cleavage pattern from the AuNP was found to be similar to the GA ladder (Figure 6.1b). These results show that the selectivity for cleavage at A and G bases by AuNP was consistently observed for different DNA strands.

The amount of cleavage of DNA by AuNP at 95 °C was quantified at different heating times of 1, 2, 4, 8 and 24 h (Figure 6.2a and b). Each band intensity was determined using SAFA,[20] allowing us to quantitatively determine the percentage of cleavage. From the data in the PAGE gel, the amount of cleavage increased with time. The uncleaved product was found to be about 90 % in the non-heated sample. The sample that was heated for an hour retained only 60 % of uncleaved product. After 24 h, nearly all of the DNA was cleaved. Our results were consistent with

a previous report by the Taton group in which the stability of DNA-AuNP conjugates were compromised upon exposure to heat. In their system, they report that there is no specificity in the site of cleavage used as the DNA strand consisted of 30 bases of A. As the DNA that we used consists of a combination of bases, we plotted the intensities at each band position (Figure 6.2c). We observed that the cleavage corresponds well to the positions of G and A on the DNA sequence while the positions of thymine (T) and cytosine (C) bases did not show much cleavage. The presence of a strong intensity at the position of the 25^{th} base corresponds to a C base but a close inspection of the gel distinctly indicates that another broader band was present on the gel (Figure 6.2a). This band was observed to be present in all of the samples at the same position regardless of the DNA sequence (Figure 6.1a and 6.2a). It is possible that this band corresponds to the cleavage product of the fluorescein from the DNA strands.

We next investigated the stability of DNA in the presence of AuNP at various temperatures, from 4 °C to 90 °C. Our initial results indicated that significant cleavage occurred at temperatures beyond 60 °C (Figure 6.3). At low temperatures, the influence of AuNP on DNA stability is less prominent. While these results are promising for the use of AuNP-DNA conjugates at physiological temperature without significant risk of degradation, applications for the AuNP-DNA conjugate at higher temperatures may result in DNA degradation.

Investigations of the reaction with Au(I)

To attribute the reactivity of DNA cleavage by AuNP, we hope to investigate the stability of DNA also in the presence of Au salt. The oxidation state of Au on the surface of the AuNP is not accurately known. However, from the crystal structures of Au clusters like thiolated Au_{38}, it was found that Au atoms form linear S-Au-S binding motifs at the cluster interface.[22,23] The

oxidation state of Au at the interface is Au(I) when binding motifs are formed.[24] Considering the oxidation state of Au at the interface in which Au reacts with DNA, it would be important to study the influence of Au(I) on the degradation of DNA.

DNA cleavage was indeed observed when Au(I) was incubated with DNA. The higher the concentration of Au(I), the more cleavage was observed (Figure 6.4a). Similar to AuNP, we observed that the extent of cleavage increased with heating time (Figure 6.4b). We also tested for DNA cleavage in the presence of other metal ions (Figure 6.4c). For the same metal ion concentration of 1.6 mM, Au(I) induced the highest amount of degradation at high temperature. Copper and iron ions also induced cleavage, though not to the same degree as Au(I), and have been previously reported as metallonucleases.[25] In addition, we observed that mercury ions interacted with the DNA resulting in a smear of DNA observed on the PAGE. This might be due to the formation of T-T mismatches bonded by mercury ions.[26,27] These results suggest that Au(I) is the species responsible for the cleavage of DNA in the presence of AuNP, rather than other trace metal ions that may also be present.

To further investigate the mechanism of cleavage, we first studied the extent of DNA cleavage induced by Au(I) in the presence of various concentrations of buffer and pH. Comparing the amount of DNA cleaved in the absence and presence of Au(I), we observed that the amount of DNA cleaved would decrease when the buffer concentration was higher and that more cleavage was observed for pH 6 than for pH 7 (Figure 6.5a). However, cleavage in the presence of Au(I) salts was still significant even after increasing the concentration of sodium phosphate to 100mM. When the degradation was tested in the presence of NaCl, the extent of DNA cleaved was also similarly reduced with increasing NaCl concentration (Figure 6.5b). This observation is consistent with the effect of salt concentration on the depurination of DNA with heat.[28] In the presence of

radical scavengers, it was found that presence of hydroxyl scavenger, ethanol (EtOH), did not show any difference to the cleavage (Figure 6.5c).[29] Sodium azide (NaN_3), a singlet oxygen scavenger, was found to reduce cleavage while reaction in deuterated water (D_2O) gave no change in the amount of cleavage (Figure 6.5d and e).[29] The lifetime of singlet oxygen was previously reported to be higher by an order of magnitude in the presence of D_2O than in H_2O.[30] This suggests that the reaction may not be via a singlet oxygen mechanism. From our studies, the amount of DNA cleavage was influenced by the presence of buffer or sodium salt. Since the Au(I) is a positively charged ion, the increase in ionic strength of the reaction solution would better screen the interaction between the DNA and Au(I). Hence, the amount of cleavage decreases with higher ionic strength. From these tests, we can conclude that the cleavage event occurs at close proximity between the DNA base and the Au(I) ion. In addition, reactive oxygen species are unlikely to be reactive intermediates for the observed DNA cleavage.

6.3 Conclusions

DNA strands were specifically cleaved at A and G bases in the presence of AuNP at high temperatures. The cleavage occurs when DNA is in close proximity to the AuNP. Similar to the AuNP, Au(I) salts were shown to result in DNA cleavage at high temperatures. The cleavage can be minimized in the presence of high ionic strength but was not affected by radical scavengers.

6.4 Experimental Section

Oligonucleotides used in the work were purchased from Integrated DNA Technologies Inc. (Coralville, IA). General chemical reagents were purchased from Sigma Aldrich and used without further purification. Thiolated DNA was first treated with tris(2-carboxyethyl)phosphine (TCEP) to cleave the dithiol bond. 2.5 µL of 1mM thiolated DNA was treated with 0.5 µL of 100 mM sodium acetate pH 5.5 and 1.5 µL of 10 mM TCEP. The mixture was left at room temperature for 1 hour before purifying once with Centricon-3k to remove excess TCEP.

Preparation of AuNP-DNA conjugates

5 mL of AuNP (20 nm, 0.86 nM) were concentrated by centrifugation once at 13,400 g and to remove supernatant. The TCEP-treated DNA was then added to the concentrated AuNP solution and left overnight. 300 mM of NaCl was added to the DNA stabilized AuNP to increase the concentration of DNA on the AuNP and left for a varying amount of hours. Excess DNA was removed by centrifugation three times. The concentrated AuNP was then diluted into 500 µL with H_2O to 2 mM sodium phosphate (NaPi) buffer pH 7. This solution was heated in a heat block at 95 ^oC.

Gel electrophoresis of Au-DNA conjugates

Heated samples were centrifuged at 13,400 *g* for 30 min three times, with 250 µL for each subsequent centrifugation. The supernatants were combined and placed in a speed vacuum to concentrate the released DNA. To obtain the DNA on the AuNP, 40ul of potassium cyanide (KCN) (100 mM) was added and left overnight. The excess KCN and $Au(CN)^{2-}$ was removed from the

solution with Amicon 3K, centrifuging three times. Cleaved products and uncleaved substrate were separated by 20 % polyacrylamide gel electrophoresis and imaged with a Molecular Dynamics Storm 430 phosphorimager. The amount of cleavage was quantified using SATA.

6.5 References

(1) Zhao, B.; Shen, J.; Chen, S.; Wang, D.; Li, F.; Mathur, S.; Song, S.; Fan, C. *Chem. Sci.* **2014**, *5*, 4460.

(2) Chen, X.-J.; Sanchez-Gaytan, B. L.; Qian, Z.; Park, S.-J. *Wiley Interdiscip. Rev. Nanomed. Nanobiotechnol.* **2012**, *4*, 273.

(3) Xing, H.; Hwang, K.; Li, J.; Torabi, S.-F.; Lu, Y. *Curr. Opin. Chem. Eng.* **2014**, *4*, 79.

(4) Sun, T.; Zhang, Y. S.; Pang, B.; Hyun, D. C.; Yang, M.; Xia, Y. *Angew. Chem. Int. Ed.* **2014**, *53*, 12320.

(5) Murphy, C. J.; Gole, A. M.; Stone, J. W.; Sisco, P. N.; Alkilany, A. M.; Goldsmith, E. C.; Baxter, S. C. *Acc. Chem. Res.* **2008**, *41*, 1721.

(6) Petersen, E.; Nelson, B. *Anal. Bioanal. Chem.* **2010**, *398*, 613.

(7) Li, J. J.; Zou, L.; Hartono, D.; Ong, C.-N.; Bay, B.-H.; Lanry Yung, L.-Y. *Adv. Mater.* **2008**, *20*, 138.

(8) Schaeublin, N. M.; Braydich-Stolle, L. K.; Schrand, A. M.; Miller, J. M.; Hutchison, J.; Schlager, J. J.; Hussain, S. M. *Nanoscale* **2011**, *3*, 410.

(9) Kang, J. S.; Yum, Y. N.; Kim, J. H.; Song, H.; Jeong, J.; Lim, Y. T.; Chung, B. H.; Park, S. N. *Biomol. Ther.* **2009**, *17*, 92.

(10) Tan, S. J.; Campolongo, M. J.; Luo, D.; Cheng, W. *Nature Nanotech.* **2011**, *6*, 268.

(11) Macfarlane, R. J.; Lee, B.; Jones, M. R.; Harris, N.; Schatz, G. C.; Mirkin, C. A. *Science* **2011**, *334*, 204.

(12) Alivisatos, A. P.; Johnsson, K. P.; Peng, X.; Wilson, T. E.; Loweth, C. J.; Bruchez, M. P.; Schultz, P. G. *Nature* **1996**, *382*, 609.

(13) Mirkin, C. A.; Letsinger, R. L.; Mucic, R. C.; Storhoff, J. J. *Nature* **1996**, *382*, 607.

(14) Storhoff, J. J.; Mirkin, C. A. *Chem. Rev.* **1999**, *99*, 1849.

(15) Stadler, A.; Chi, C.; van der Lelie, D.; Gang, O. *Nanomedicine* **2010**, *5*, 319.

(16) Liu, J.; Cao, Z.; Lu, Y. *Chem. Rev.* **2009**, *109*, 1948.

(17) Wang, Z. D.; Lu, Y. *J. Mater. Chem.* **2009**, *19*, 1788.

(18) Herdt, A. R.; Drawz, S. M.; Kang, Y.; Taton, T. A. *Colloids Surf. B Biointerfaces* **2006**, *51*, 130.

(19) Bhatt, N.; Huang, P.-J. J.; Dave, N.; Liu, J. *Langmuir* **2011**, *27*, 6132.

(20) Das, R.; Laederach, A.; Pearlman, S. M.; Herschlag, D.; Altman, R. B. *RNA* **2005**, *11*, 344.

(21) Hampshire, A. J.; Rusling, D. A.; Broughton-Head, V. J.; Fox, K. R. *Methods* **2007**, *42*, 128.

(22) Jadzinsky, P. D.; Calero, G.; Ackerson, C. J.; Bushnell, D. A.; Kornberg, R. D. *Science* **2007**, *318*, 430.

(23) Whetten, R. L.; Price, R. C. *Science* **2007**, *318*, 407.

(24) Hakkinen, H. *Nature Chem.* **2012**, *4*, 443.

(25) Jiang, Q.; Xiao, N.; Shi, P.; Zhu, Y.; Guo, Z. *Coord. Chem. Rev.* **2007**, *251*, 1951.

(26) Ono, A.; Togashi, H. *Angew. Chem. Int. Ed.* **2004**, *43*, 4300.

(27) Miyake, Y.; Togashi, H.; Tashiro, M.; Yamaguchi, H.; Oda, S.; Kudo, M.; Tanaka, Y.; Kondo, Y.; Sawa, R.; Fujimoto, T.; Machinami, T.; Ono, A. *J. Am. Chem. Soc.* **2006**, *128*, 2172.

(28) Greer, S.; Zamenhof, S. *J. Mol. Biol.* **1962**, *4*, 123.

(29) Bruskov, V. I.; Malakhova, L. V.; Masalimov, Z. K.; Chernikov, A. V. *Nucleic Acids Res.* **2002**, *30*, 1354.

(30) Bruskov, V. I.; Petrov, A. I. *Mol. Biol.* **1992**, *26*, 1362.

6.6 Figures

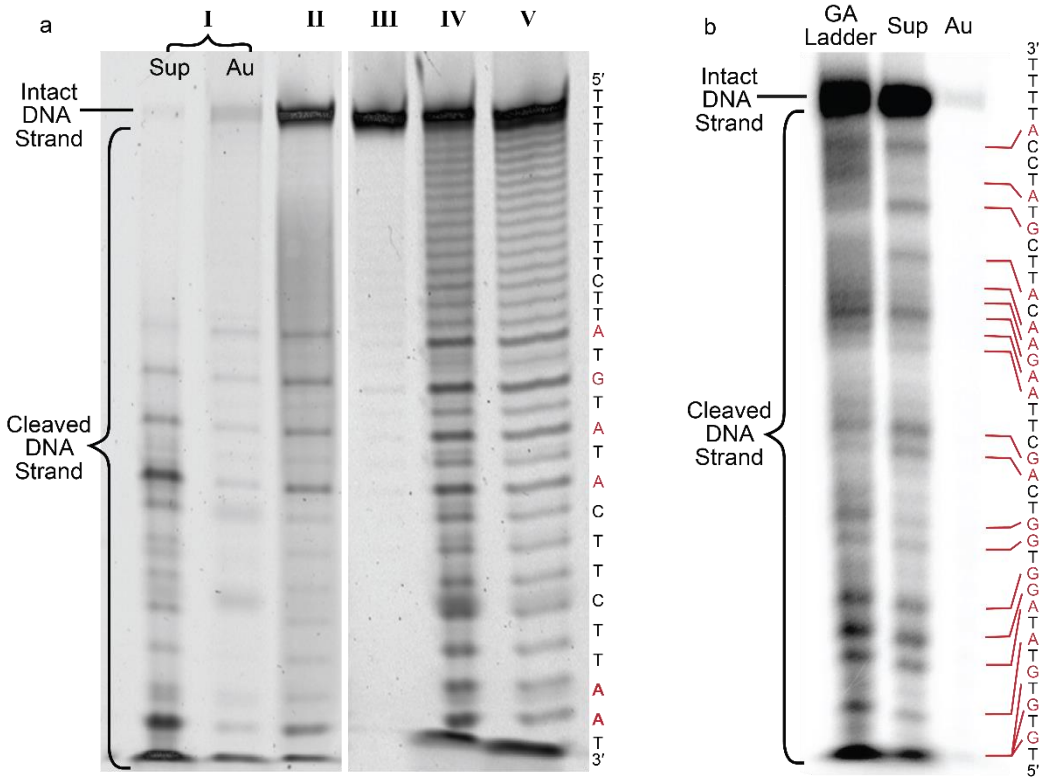

Figure 6.1. (a) PAGE gel of DNA conjugated AuNPs (I) Sup: supernatant after heating for 8 hrs and Au: DNA remaining on AuNPs after heating (obtained from etching of the AuNPs by adding 10 µL of 100 mM KCN) and (II) in the absence of heating. Mixture of 1µL of 1 mM DNA with 1 mL of 1.16 nM AuNPs, (III) in the absence of heating, (IV) heated for 8 h in a 1.5ml centrifuge tube, and (V) heated for 8 h in a scintillation vial. Sequence of DNA used 5′ SH- TTT TTT TTT T TCT TA TGT ATA CTT CTT AAT-FAM 3′ is indicated on the gel corresponding to each cleavage at each band. (b) PAGE gel of the 43 base DNA P^{32} labeled at the 5′ conjugated on AuNPs and heated for 8 h the supernatant of heated sample and the DNA retained on the AuNPs. The position of G and A bases for the 43 base DNA are shown in the GA ladder.

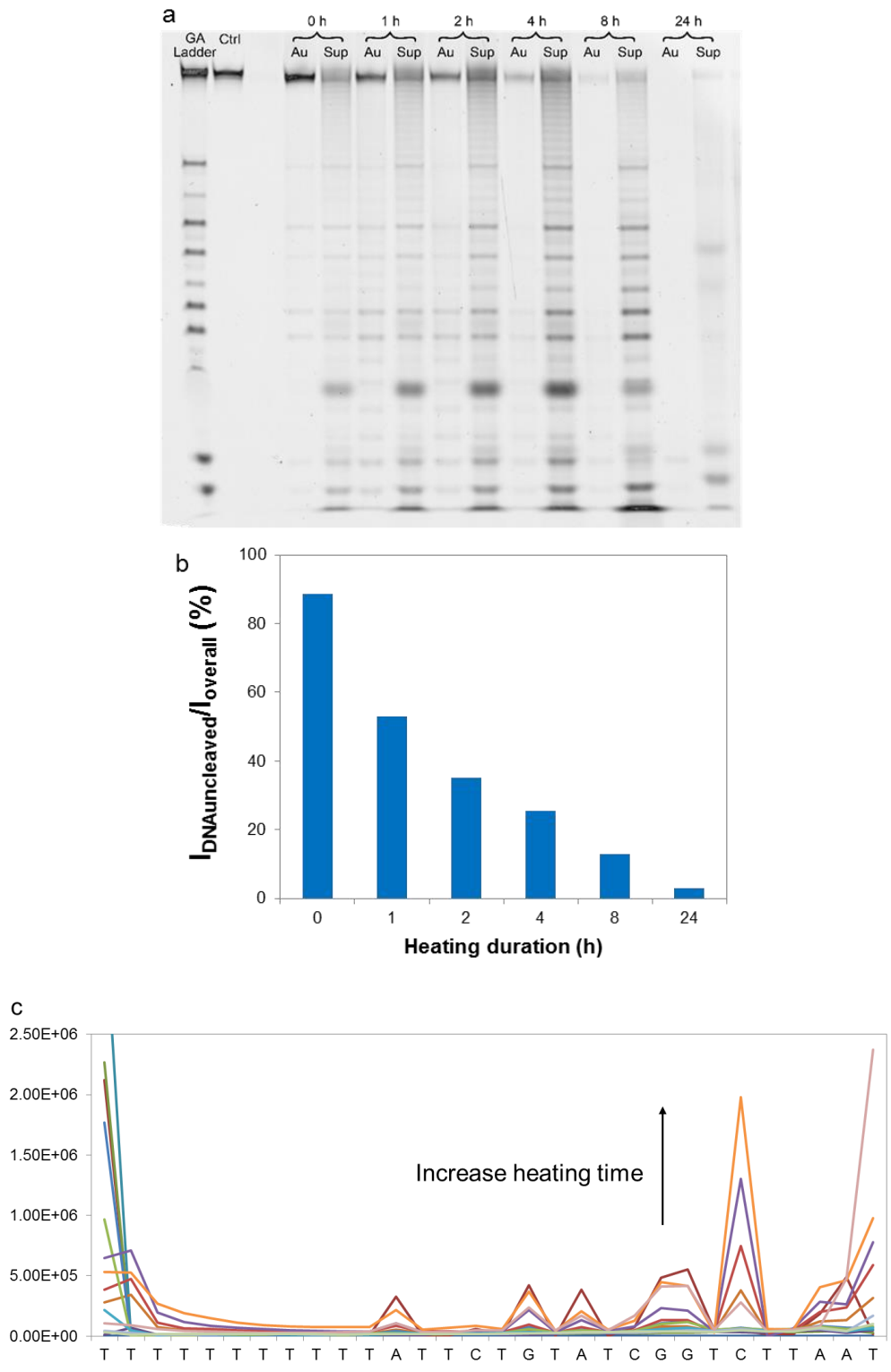

Figure 6.2. (a) PAGE gel of AuNP-DNA conjugates heated at various times. (b) Graph of percentage of uncleaved DNA calculated from the band intensities in the PAGE gel against heating time. (c) Intensity of each band obtained from PAGE gel corresponding to the DNA sequence.

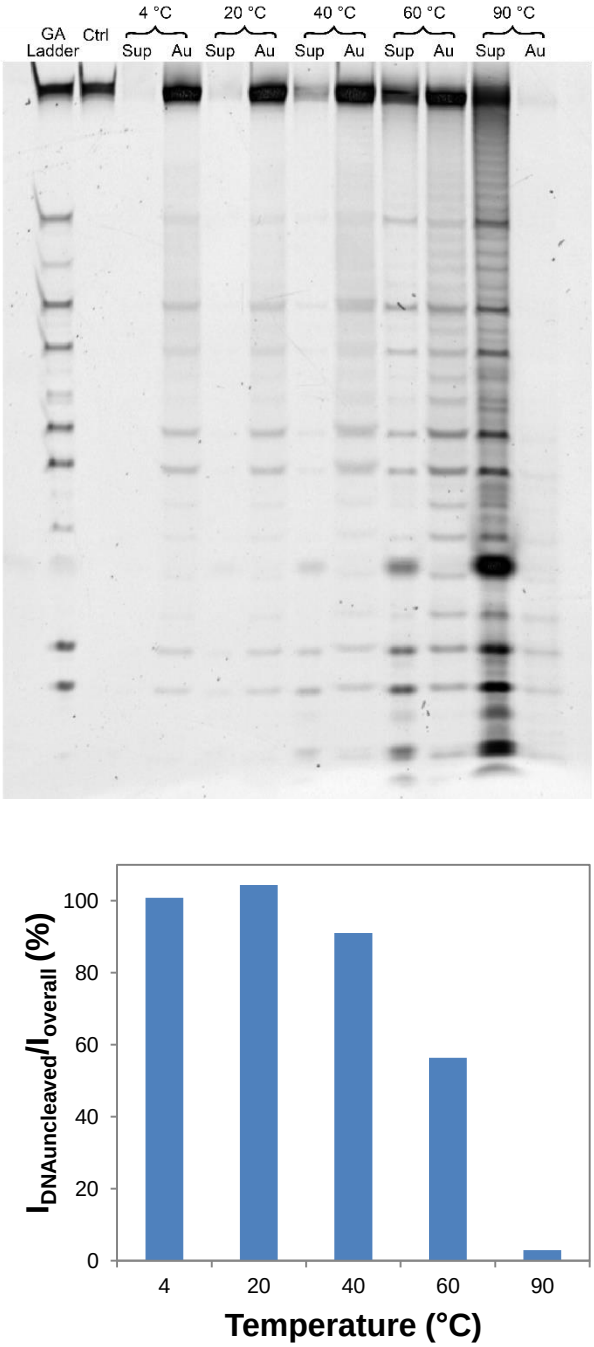

Figure 6.3. PAGE gel of AuNP-DNA conjugates heated at various temperatures and graph of percent uncleaved DNA calculated from the band intensities with change in temperatures.

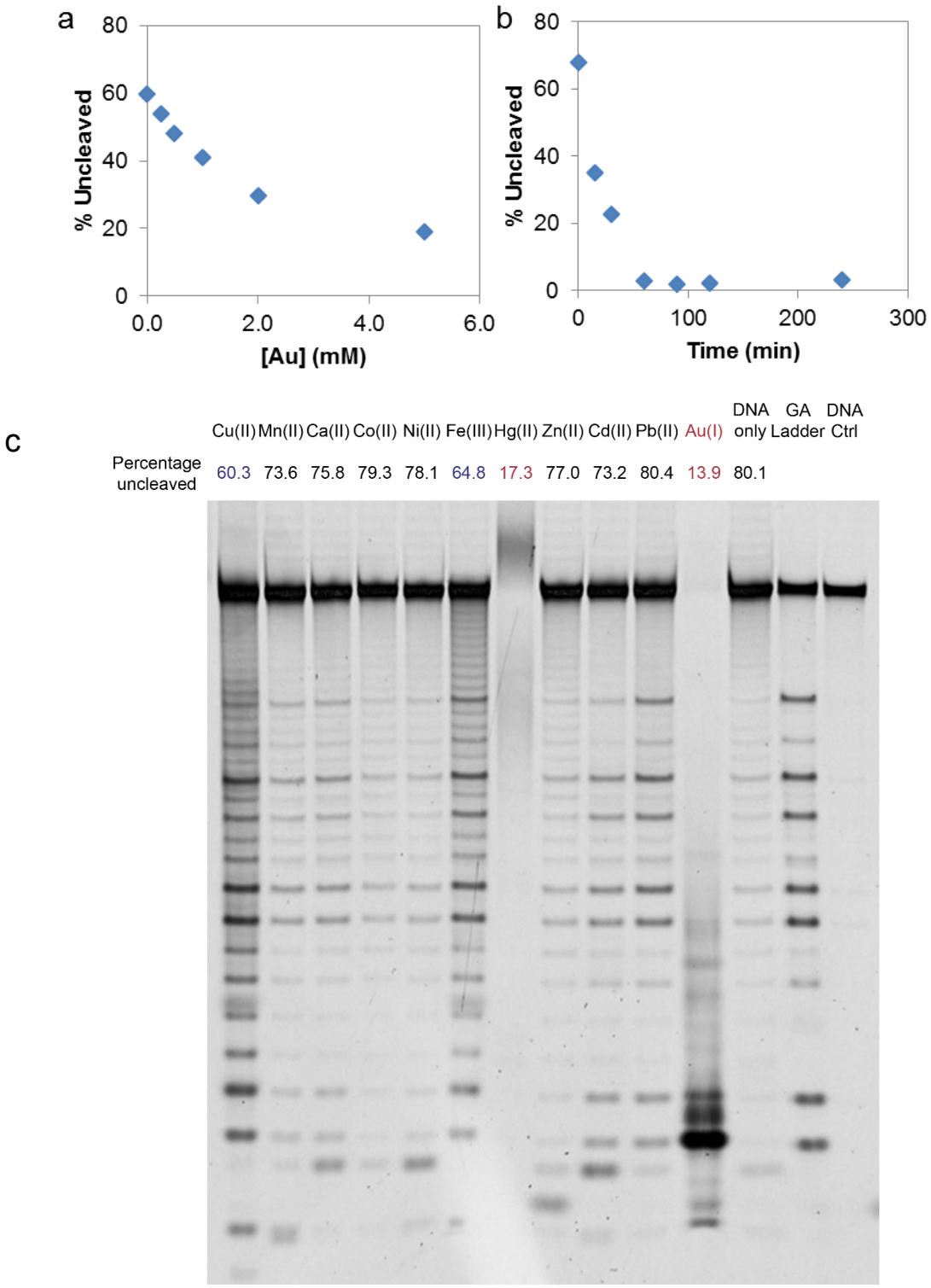

Figure 6.4. Graph of percent DNA uncleaved over (a) Au(I) concentration and (b) time (min). (c) PAGE image of the samples when DNA were incubated with various metal ions and the percentage of cleavage indicated at the top of the gel image.

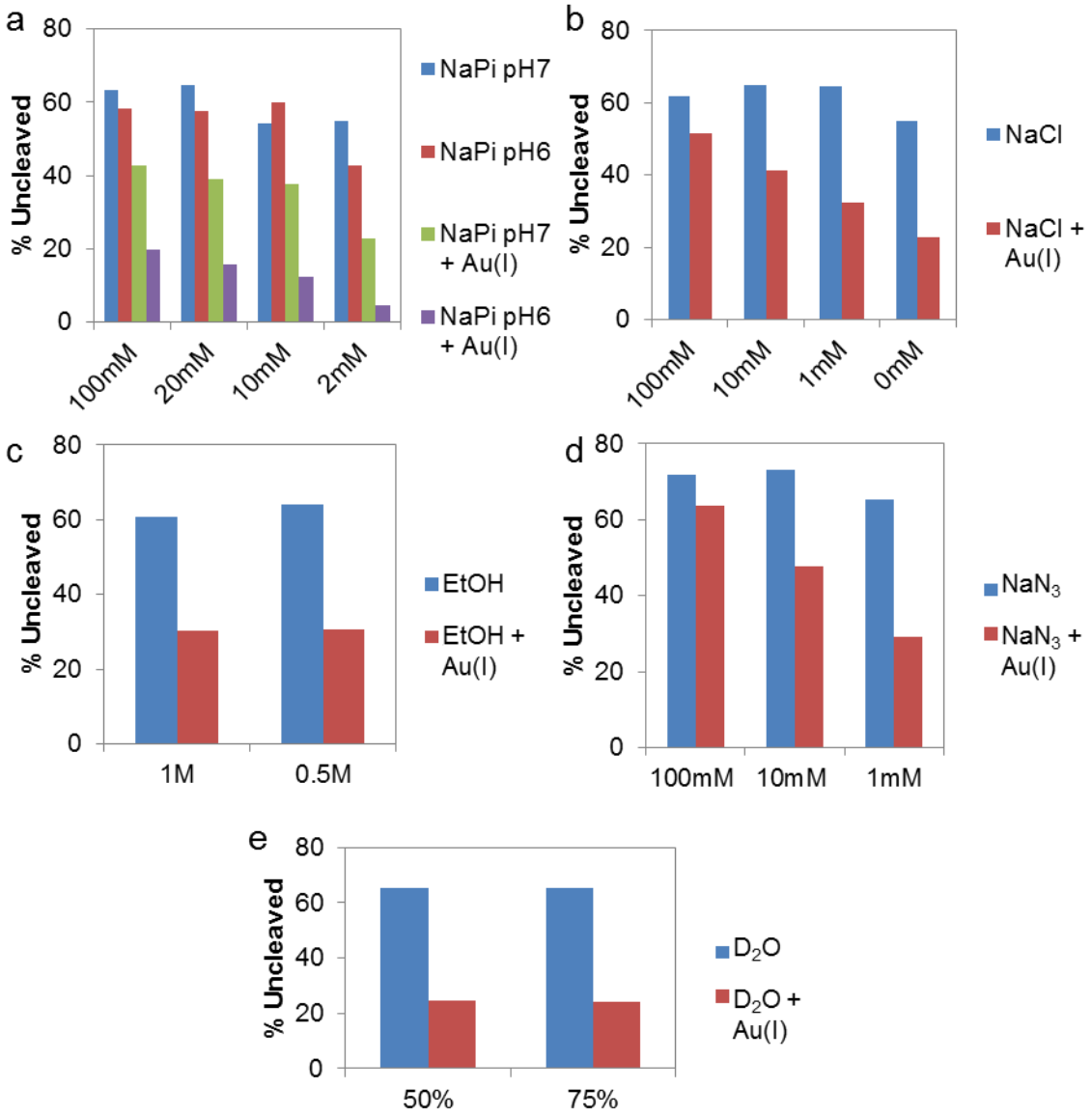

Figure 6.5. Graph of percent of DNA cleavage against (a) buffer concentration, (b) sodium chloride concentration, (c) ethanol concentration (d) NaN_3, singlet oxygen scavenger concentration and (e) in different percentages of D_2O in the presence and absence of Au(I) to indicate the effect of the additives on Au(I) induced cleavage of DNA.